Structural and electronic properties of Nb_3Sn in the high pressure and low temperature region

by

Rita Loria

Submitted to the Department of Science
for the degree of

Doctor of Philosophy of Material Science, Nanotechnology and
Complex Systems

at the

UNIVERSITY OF ROMA TRE

October 2018

Abstract

Currently, the A15 type compound Nb_3Sn represents the most appropriate superconductor for applications requiring magnetic fields well above 10 T, such as the future particle accelerators and fusion reactors. The stress-strain dependence of Nb_3Sn properties is a research topic long since. It is known in particular that an applied uniaxial and/or transverse load remarkably affects Nb_3Sn superconducting properties by degrading both its critical current density and critical temperature: consequently such strain sensitivity is a key factor to be considered when dealing with the above mentioned high-field applications. The response of Nb_3Sn to mechanical stresses is then a topic of strong interest. In order to shed light onto the degradation of the superconducting properties as function of stress and strain, a first approach concerns the investigation of the structural and superconducting properties when a high hydrostatic pressure is applied.

Recently, X-ray diffraction (XRD) experiments on the two A15 compounds - Nb_3Al and Nb_3Ga - as a function of an applied hydrostatic pressure, revealed a pressure-induced isostructural phase transition which has been subsequently suggested to be an Electronic Topological Transition (ETT) by means of first-principle calculations. In this thesis work the structural and superconducting properties of Nb_3Sn as a function of the hydrostatic pressure have been studied by means of XRD, XAFS (X-ray absorption spectroscopy), Density Functional Theory (DFT) and Density Functional Perturbation Theory (DFPT) calculations, revealing that also Nb_3Sn could exhibit an anomaly as a function of the hydrostatic pressure below 10 GPa. XRD at high pressure suggested that Nb_3Sn has an anomaly in the compressibility at around 5-6 GPa. XAFS measurements confirm the presence of a structural anomaly, that can be related to dimerization effect of the Nb chains that characterizes the Nb_3Sn structure. Based on first-principle calculations, the phonon and electronic contributions to this anomaly have been investigated: in particular, from the simulations it can be inferred that the observed anomaly presumably originates from phonons and thus from lattice contributions.

This work, with the goal to shed light on the nature of the recently observed pressure-induced structural anomaly on A15 compounds, represents an effort toward the general understanding of the behaviour of A15 Nb-based superconductors as a function of pressure.

To my Family

Acknowledgments

I would like to express my special thanks to Prof. Carlo Meneghini and Prof. Enrico Silva for their guidance, enthusiasm and ideas and the support they gave me throughout this work, I will never forget their teachings.
I remember with gratitude the support of Dr. Simone Anzellini of Diamond Light Source for having taught me the tricks of diamond-anvil anvil cells and of Dr. Gianluca De Marzi of ENEA for introducing me into the world of first principle calculations.

Finally, I would like to say a special thanks to the support of my loving family, nothing of this work would have been possible without their support.

Contents

1 Superconductivity 25

1.1 The Bardeen-Cooper-Schrieffer theory 30

1.2 The Eliashberg Theory 35

1.3 Notes on the Ginzburg-Landau theory 37

2 A15 materials 43

2.1 Physical properties of Nb_3Sn 45

2.1.1 Phase Diagram 45

2.1.2 The Batterman-Barrett Transformation 46

2.2 High pressure effects on superconductivity 55

2.2.1 The High pressure effect on A15 superconductors 57

3 The Nb_3Sn samples 65

3.1 Nb_3Sn wire 65

3.2 Nb_3Sn polycrystalline samples 67

3.3 Microwave measurements 69

4 X-ray diffraction characterization 77

4.1 Notes on X-Ray Powder Diffraction and Rietveld Refinement 78

4.2 XRD experiments on Nb_3Sn 81

4.2.1 Data reduction 81

4.2.2 HP-XRD diffraction at room temperature 83

4.2.3 XRD diffraction at low temperature 95

5 High pressure EXAFS characterization 105

5.1 The X-ray absorption spectra 106

5.2 Origin of the EXAFS structure signal 108

5.3 EXAFS measurements on Nb_3Sn 114

5.4 Results from EA-RMC analysis 124

6 DFT based first-principles calculations 129

6.1 Notes on Density Functional Theory 131

6.2 Details of Calculations on Nb_3Sn 138

6.2.1 Convergence tests 139

6.2.2 Computation scheme 142

6.3 Results of the calculations 143

6.3.1 Ambient pressure 143

6.3.2 High pressure 146

7 Conclusions 155

A The Peierls distortion in 1D chain 161

B Elastic constants 165

C Diamond anvil cell 171

C.1 Membrane Diamond Anvil Cell 174

C.2 Pressure calibration 176

List of Figures

1-1 Flux penetration behaviour of type I and type II superconductors. . . 26

1-2 $\rho\,(T)$ curves of a sample of Nb_3Al under different magnetic field values in T (shown in blue) [23]. It is possible to see how T_c decreases as the the applied field increases. 27

1-3 Schematic diagram of vortex in the Shubnikov phase. 28

2-1 (Top) The unit cell of A_3B compounds. A atoms are dark red coloured, B atoms are pink. (Bottom left) The coordination environment of B atoms and (Bottom right) A atoms. 44

2-2 Niobium-Tin phase diagram after Charlesworth *et al.* [54]. 45

2-3 Lattice parameter versus temperature for Nb_3Sn single crystal determined by Mailfert *et al.* [58]. 47

2-4 Model of the Nb atom sublattice shift due to the Batterman-Barrett transformation in Nb_3Sn (full circles Nb; empty circles Sn) [59]. . . . 48

2-5 Schematic phase diagram for the superconducting and martensitic phase transitions as function of λ_L. NT, SC, ST and NC means normal tetragonal, superconducting cubic, superconducting tetragonal and normal cubic phases respectively [66]. 50

2-6 Elastic moduli versus temperature of Nb_3Sn obtained from measured sound velocities in the (100) and (110) directions [12]. The straight red line and an arrow in the c_{44} shear modulus has been sketched in order to better evidence the change of slope below 200 K. 51

2-7 The stiffness parameter $\dfrac{C_{11} - C_{12}}{2C_{44}}$ versus temperature [68]. 53

2-8 Temperature dependence of the frequency of the E_g Raman peak of Nb_3Sn [70]. 54
2-9 Periodic table indicating the superconducting and magnetic properties of the bulk elemental solids at ambient and high pressure, from [81]. . 56
2-10 The pressure dependence of T_L and T_c in (left) V_3Si and (right) Nb_3Sn. 59
2-11 Electronic density of states of Nb_3Sn from ab-initio calculations. . . . 60
2-12 The P-V plot of (left) Nb_3Ga [8] and (right) Nb_3Al [7]. 61
2-13 T_c plotted as a function of A for Nb_3Sn (S=single cristal) and (P=policrystalline sample) under pressure. The solid lines are guide to the eyes. [11] 62

3-1 SEM cross section of the OCSI internal-tin strand (outer diameter 0.81 mm), after heat treatment (left). One of the strand sub-elements(right). [90]. 67
3-2 EDX analysis of the OCSI strand, after the heat treatment. The white area represents the spatial distribution of each element. Upper left: Cu; upper right: Nb; lower left: Sn; lower right:Ta [90]. 67
3-3 SEM of Nb_3Sn policrystalline samples. 69
3-4 Literature results of the lattice parameter a and the critical temperature T_c as a function of the atomic Sn content (adapted from [31]). The red points are the value of a and T_c of the laboratory polycrystalline Nb_3Sn samples studied in this thesis. 70
3-5 Sketch of a typical dielectric resonator. The circular geometry of the current on the sample is shown. 72
3-6 Experimental setup. 73
3-7 The surface resistance R_s of a Nb_3Sn platelet at 0 T. 74
3-8 The surface resistance, $R_s(T, B)$, as function of temperature at different values of an applied magnetic field on the polycrystalline Nb_3Sn sample. 74
3-9 The surface resistance R_s at 15 K as function of the applied magnetic field B on the polycrystalline Nb_3Sn sample. 75

3-10 Temperature dependence of the critical field of the polycrystalline Nb_3Sn sample. 76

3-11 Literature results of the upper critical magnetic field as a function of the atomic Sn content (adapted from [31]). The dashed line separates the region in which the phase is cubic (C) from that in which it is tetragonal (T). The red point is the value of B_{c_2} of the polycrystalline Nb_3Sn samples studied in this thesis. 76

4-1 (left) Debye rings and (right) powder diffraction pattern from a fine grained sample of Nb_3Sn. 82

4-2 Example of LaB_6 calibration for the diffraction patterns. 83

4-3 (Left) Diffraction pattern of the data at 2.56 GPa (run2) after 2D image integration and (right) after a 13 degree polynomial background subtraction. 84

4-4 Picture of a sample completely embedded in the pressurized He transmitting medium, with the ruby pressure gauge near the sample. . . . 84

4-5 Integrated powder X-ray diffraction patterns of the samples (powdered filaments of Nb_3Sn) at lowest (upper panel) and highest (lower panel) pressure reached. Diffraction peaks of Nb_3Sn (black), Cu (red) and Ta (green) are labeled by colors. The insets show a part of the recorded raw diffraction images. 85

4-6 The 200 diffraction peak of Nb_3Sn at all the pressures of run2. 87

4-7 (top): measured volume of Nb_3Sn as a function of the pressure. (bottom): difference between measured and fitted volume, with the anomaly below 10 GPa. 89

4-8 Peak position differences, $\Delta_{400,321}$ and $\Delta_{400,222}$, as function of pressure: an anisotropy of the elastic properties around 6 GPa can be seen. . . 90

4-9 The specimen-broadening parameters LX and LY relative to run1. . 90

4-10 FWHM at $\theta = \pi/6$ relative to run1. 91

4-11 Ratio of the normalized volumes of the different phases. 93

4-12 The three spectra collected 88 K. In the inset a zoom in the 34-37 degrees interval is shown. 95

4-13 The Nb_3Sn 321 diffraction peak as function of temperature on cooling (DOWN run). The peak intensity has been normalized to the peak maximum. The very good statistical quality achieved by 2D setup can be appreciated. 96

4-14 The diffraction pattern at 88.08 K (DOWN run): all the peaks are indicated. Superimposed the Rietveld refinement of the full spectrum obtained with the software GSAS/EXPGUI (red curve). The difference between the observed (cross symbols) and the fitted pattern is shown with a line at the bottom of the graph. 97

4-15 Top graphs: The volume and lattice parameter obtained with the Rietveld refinement of the data. Bottom graphs: the difference between the linear fit in the two regions, LT and HT, showing better the change of the lattice parameter slope. 98

4-16 The lattice parameter has been extrapolated at 43 K to be compared with that reported in [58] (see fig. 2-4). 100

4-17 The specimen-broadening parameters LX and LY: again the anomaly at 175 K can be appreciated, here as an inversion of slope of the two parameters. 101

4-18 The FWHM at different values of the angle θ as function of temperature (from the DOWN set). 101

4-19 The ratio $\frac{c}{a} - 1$ as function of the temperature: an abrupt change of slope at around 120 K is present. 103

5-1 EXFAS phenomenon scheme: (a) the photon impinges the atom A (the black circle indicates the orbital of the core electron); (b) a core electron of the atom A absorbs the energy of the photon and is photoemitted. It is represented by its outgoing wave function (the white circle indicates the hole in the core state); (c) the outgoing and the backward diffused wave functions from the atom B interfere. 106

5-2 Absorption coefficient as function of the incoming radiation. 106

5-3 Scheme of the two atoms system: A is the absorber atom and B the backscatterer. The grey regions represent the muffin-tin potential spheres [115]. 112

5-4 BM23 beamline: optical layout [125]. 114

5-5 $x\mu(E)$ at 7 GPa. 116

5-6 Pre-edge and post-edge subtraction and normalization at 7 GPa. . . . 117

5-7 Background subtraction at 7 GPa. 118

5-8 The extracted $k^2\chi(k)$ EXAFS signals as a function of pressure. 118

5-9 The magnitude of the complex $\chi(R)$ as function of pressure. 119

5-10 The list of the first ten scattering paths produced after running FEFF on the ATHENA software. The following information about each path are given in the columns: (I col.) order of the path, (II col.) multiplicity, (III col.) half-length of the scattering path, (IV col.) relative amplitude and (V col.) path, where the backscatterer atoms are listed and the absorbing atom is indicated with [+]. 120

5-11 Scattering paths of the first three shells. 120

5-12 Result of the fit to the $|\chi(R)|$ function obtained with ARTEMIS at 2 GPa. The gray region is the fitting region. 121

5-13 Result of the fit to the $|\chi(R)|$ function obtained with ARTEMIS at 26 GPa. The gray region is the fitting region. 122

5-14 *delr* as function of pressure. 122

5-15 The MSRD factor σ^2 as function of pressure. 123

5-16 Distance distributions of the first (a), second (b) and third shell (c) at different pressures. 125
5-17 Correlation between first shell Nb atoms. 126

6-1 Total energies for Nb_3Sn calculated as a function of the k-point grid (left) and of the cut-off energy (right). 140
6-2 The first Brillouin zone for A15 structures. 143
6-3 Total energy of Nb_3Sn in the simple cubic crystal structure as a function of the volume, V. The curve shows the fit of the DFT data. . . . 144
6-4 The electronic band structure and density of states of Nb_3Sn calculated at atmospheric pressure. The Fermi level is set to 0 eV (dashed orizontal line). 145
6-5 Phonon dispersion and density of states for Nb_3Sn at ambient pressure. 146
6-6 Calculated volume of Nb_3Sn as a function of pressure, compared with XRD data. 147
6-7 Electronic density of states of Nb_3Sn near the Fermi level at different values of pressure. 148
6-8 ω_{ln} as a function of hydrostatic pressure. In the inset a zoom at low pressure is shown. 149
6-9 The critical temperature T_c calculated as a function of hydrostatic pressure (black line). The electronic and vibrational contributions have been separated by fixing ω_{ln} and $< I^2 >$ (red line) or N_{E_F} (green line) at their atmospheric pressure values. 150
6-10 The behaviour of the elastic constants in cubic Nb_3Sn as a function of hydrostatic pressure. 151
6-11 The difference between a linear fit at pressure below 6 GPa and the calculated elastic constants. 152
6-12 The elastic constants calculated by Reddy *et al.* [10] 153

A-1 Up: a linear chain of identical atoms equally spaced; Down: the chain of atoms after the Peierls distortion. 162

A-2 Electron energy in linear chain. Left: uniform spacing a. Center: uniform spacing $2a$ with two atoms per cell. Right: Dimerized chain. 163

B-1 Stress components acting on the 1,2,3-planes. 166
B-2 The scheme of the types of deformation of a cube seen from a face: (left) compression, (center) dilatation on compression, (right)shear deformation. Below each scheme: the constitutive relation written with the four indices notation and with the Voigt notation. 169

C-1 Opposed diamond anvil configuration, with a metallic gasket for sample confinement in a pressure medium; the basic part of the DAC. 172
C-2 Schematic representation of the components of a membrane diamond anvil cell. The membrane is filled with helium through a capillary and transmits the force to the piston. 175
C-3 Plot of the pressure measured in the cell as a function of the pressure in the membrane, in the case of the HP-XRD experiment described in sec. 4.2.2, run2. 175
C-4 Plot of the fluorescence signal obtained at pressure 4.77 GPa. 177

List of Tables

1.1 Critical temperature T_c, energy gap to T_c ratio $\frac{2\Delta(0)}{k_B T_c}$, upper critical magnetic field at 0 K $H_{c_2}(0)$, Debye temperature Θ_D and experimental and theoretical electron-phonon coupling parameter λ for selected strong coupling superconductors [41–48]. 38

4.1 The V_0, K_0 and K_0' values from the fits of $P-V$ data. 88

4.2 Rydberg-Vinet fit parameter for Cu and Ta relative to run1. 92

4.3 The volume and lattice parameter values from Rietveld analysis at room temperature. 98

4.4 Table of the thermal expansion coefficient. 99

6.1 The lattice parameter, bulk modulus and its derivative and the critical temperature T_c calculated at ambient pressure. Also literature values are reported, from ref. [110, 149, 150] 145

6.2 The values of the volume, bulk modulus and its first derivative at ambient pressure obtained from the Rydberg-Vinet fit of volumes computed by BFGS variable-cell relaxation at different pressure. 147

Introduction

The A15 Nb_3Sn superconductor is currently the protagonist material for high magnetic field applications like dipole and quadrupole magnets for particles accelerators such as the High-Luminosity Large Hadron Collider (HL-LHC) [1], central solenoid and toroidal field coils in tokamak fusion devices such as in the International Thermonuclear Experimental Reactor (ITER) [2, 3], nuclear magnetic resonance (NMR) [4], and laboratory hybrid magnets [5]. Although this material has been known for more than sixty years, its use and development have been heavily hampered due to its intrinsic brittleness and strain sensitive superconducting properties, while technologies based on the use of the most ductile and less expensive NbTi represented the first workhorse among the superconducting materials in the field of high magnetic fields applications. However NbTi, with its upper critical magnetic field of 9 T, is no longer sufficient for the above listed modern and future high magnetic fields applications for which Nb_3Sn has become the mandatory choice, being the Nb_3Sn today the only commercially available superconductor that can generate magnetic fields well over 10 T. Indeed, alternative conductors based, for example, on the more tolerant to the strain Nb_3Al (of the same structural family of Nb_3Sn and with similar superconducting properties) are in development stage while technologies based on the High Temperature Superconductors (HTS), which in principle have superconducting properties that better meet the requirements of high field applications allowing to reach higher magnetic field at higher operational temperature, are hampered by their poor mechanical properties (HTS are in general very brittle materials) and high cost.

In the high fields applications above listed Nb_3Sn is subject to strong mechanical stresses due to the thermal contraction differences during cooldown and the high Lorentz forces that develop during charging of the magnet [6]. The combining of these large forces and brittle material, like Nb_3Sn, make the design and assembly of the magnets a real challenge. In this context, having a good knowledge of the effects of stress acting on the material is of paramount importance in order to understand the performance of the material in these very powerful applications. However, investigations of the fundamental properties of Nb_3Sn stopped at the eighties, when the focus shifted and still remains on technological applications.

The request for ever more performing superconductors, the foreseen new application areas such as the superconducting radio frequency (SRF) cavities and the current availability of more accurate theoretical and experimental investigation techniques (compared to those of fifty years ago) have revamped the interest on Nb_3Sn and the other A15 superconducting compounds. Several works recently appeared in literature, mostly concerning the study of the effect of a high hydrostatic pressure on the structural and superconducting properties of A15 compounds. High pressure X-ray diffraction experiments on Nb_3Al and Nb_3Ga have recently pointed out that these two A15 materials show a pressure induced isostructural transition [7,8], that the first principles calculations of Rajagopalan [9] and Reddy *et al.* [10] show is related to an electronic topological transition. Finally, dates back only to the last year the work of Ren *et al.* [11] in which the critical temperature behaviour as function of pressure (up to $\sim$ 10 GPa) of Nb_3Sn has been studied, pointing out a degradation of the critical temperature as pressure increases, originating in the decrease with pressure of the electronic density of states at the Fermi level.

In this context, this thesis work combines cutting-edge investigation techniques (X-ray diffraction and X-ray absorption spectroscopy experiments at high pressure, using membrane diamond anvil cells) and advanced ab-initio techniques (based on density functional theory and density functional perturbation theory, DFT and DFPT) to explore the material structure down to the atomic scale and its response to mechanical (hydrostatic pressure) and thermal (cooling) stresses. In particular X-ray absorption spectroscopy (XAFS) and X-ray diffraction (XRD) are complementary structure determination techniques: XRD allowed us to determine the crystal structure of Nb_3Sn up to ~50 GPa showing a compressibility anomaly in the first few GPa, while XAFS, a local probe technique, showed how the anomaly is related to the dimerization of Nb atoms along the characteristic perpendicular Nb chain in the structure of Nb_3Sn. DFT and DFPT based calculations have been carried out to explore the structure, the electronic and phonon dispersion curves and the critical temperature of the material up to 50 GPa. Instabilities in the critical temperature originating from a phonon anomalous behaviour and a discontinuity in the shear moduli of the material are predicted to occur in the first few GPa. The results of the calculations and of the experiments have often been compared to evaluate the quality of the constructed theoretical model. Moreover, XRD investigations at temperature down to liquid nitrogen and ambient pressure have pointed out the possible presence of precursors of the tetragonal transition, that in Nb_3Sn takes place at ~40 K, already at 120 K and a discontinuity of the thermal compression that likely has to be related to the previously observed and not investigated discontinuity of the shear modulus C_{44} [12].

This thesis is organized in seven chapters.

In the first chapter the properties of the superconductors and the current applications based on low critical temperature superconductors are described in general, and especially as regards Nb_3Sn. Then follows a review of the Bardeen-Cooper-Schrieffer theory and its extension proposed by Eliashberg, and the more phenomenological Ginzburg-Landau theory, within which the superconducting properties of Nb_3Sn can be understood.

The second chapter is dedicated to the description of Nb_3Sn properties, with some reference to the other A15 superconductors. Particular emphasis is placed on reviewing the results of literature concerning structural properties, in particular the tetragonal transition, and how these are related to the superconducting properties of the material. Moreover, the effect of a hydrostatic pressure on superconducting materials is discussed in general and in more detail for Nb_3Sn.

In the third chapter the studied samples are described, together with further microwave characterizations carried out during this thesis work by means of which the critical temperature as function of an applied magnetic field has been investigated and the upper critical magnetic field has been determined.

In the fourth chapter the experiments of diffraction under pressure (0-50 GPa) and low temperature (80-300 K) and their results are described, highlighting the new information they reveal. The long range structural characterizations of this chapter are then followed with the fifth chapter where the short range XAFS characterizations at high pressures (0-26 GPa) are described. Here the local structure around a Nb atom in the Nb_3Sn cell is delineated.

The sixth chapter is devoted to the description of the first-principles calculations on Nb_3Sn. Here the results are discussed by comparing them to those of the previous chapter and those of literature.

In the last chapter, the summary of this work was drawn. In particular the new experimental results of this thesis work on the structural properties of Nb_3Sn as function of an applied hydrostatic pressure and of temperature are discussed highlighting the importance of exploiting the now available advanced experimental techniques in order to unveil and understand them. A discussion of the results of the first-principles calculations follows, with an inspection of the strengths and limits of the proposed model. Finally, future prospects opened by these studies are discussed.

Chapter 1

Superconductivity

Superconductivity is a phenomenon such that certain materials show zero electrical resistance (observed for the first time in 1911 by H. Kamerlingh Omnes[1] on mercury [13]) and expulsion of magnetic field (the “Meissner effect” [14]) when cooled below a characteristic critical or transition temperature T_c.

This was a very remarkable discovery at the time, being the first evidence of real materials with zero resistance and thus able to carry electric current without dissipations. Moreover, right from the discovery, it has been envisioned that superconductors might be used to generate strong magnetic fields. However, an issue arose: their transition temperature approached absolute zero and cooling to such low temperatures is expensive and often not cost efficient.

During the first 60 years after the discovery of superconductivity the search for new superconducting materials led only to a slow increase in the highest known transition temperature T_c, reaching a plateau at 23 K with the discovery in 1973 of the superconductivity in Nb_3Ge [15], leading scientists to think that superconductivity only occurs in elemental metals and intermetallic compounds at low temperature.

Thirteen years later, the revolutionary discovery by J. G. Bednorz and K. A. Müller[2] [16] of superconductivity at ∼35 K in the ceramic material $La_{5-x}Ba_xCu_5O_{5(3-y)}$ opened the way to radically higher transition temperatures. This was followed a few

---

[1] Nobel Prize in physics 1913

[2] Nobel Prize in physics 1987

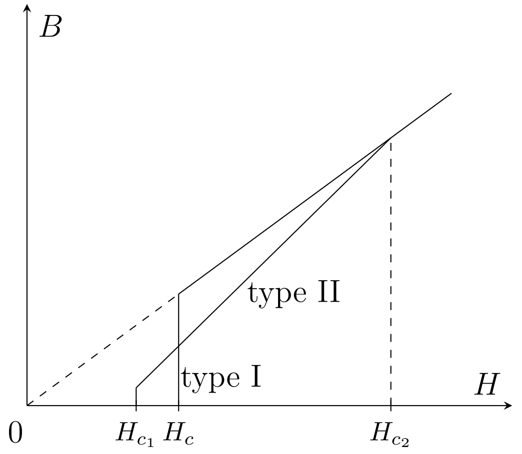

Figure 1-1: Flux penetration behaviour of type I and type II superconductors.

months later by the discovery of superconductivity at 90 K in a structurally related material, $YBa_2Cu_3O_{7-\delta}$ [17]. Cuprate superconductors showed T_c up to 135 K at non and ambient pressure. Then, the phenomenon of superconductivity is not restricted any more to very low temperature. During the last 30 years many other superconducting compunds have been found, and this development is by no means closed. Among all the last superconducting materials discovered, it is worth to mention the two band superconductor magnesium diboride (MgB_2) [18] in which two electronic bands cross the Fermi level giving rise to two distinct superconducting gaps; fullerenes which have nanosuperconducting characteristics [19]; the heavy fermion compounds [20], where magnetic interactions are essential for superconductivity; the iron pnictides [21] and the hydrogen sulfide H_2S that with a T_c of 203 K (but at the very high pressure of 150 GPa) holds the record for the highest transition temperature since 2015 [22].

Based on the differences in their behaviour in presence of a magnetic field, all superconductors are classified as type I or type II superconductors (see fig. 1-1). Indeed, the critical temperature T_c in addition to taking material-dependent values, also depends on the intensity of an applied magnetic field (see fig: 1-2). This means that above a characteristic magnetic field H_c, superconductivity disappears, whatever the temperature is. Type-I superconductors are materials in which an externally applied magnetic field is completely excluded up to a critical field H_c and superconductivity is

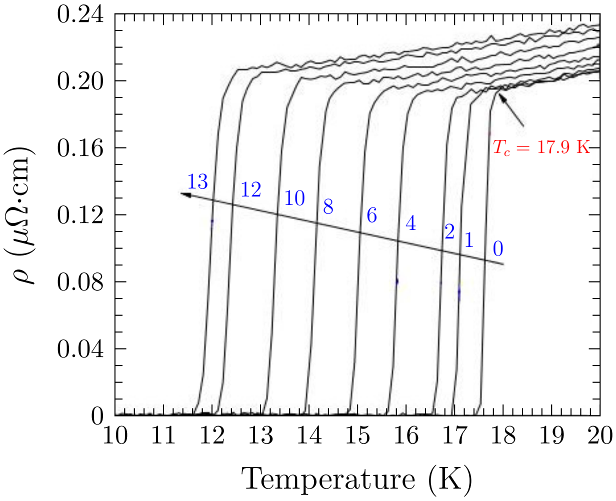

Figure 1-2: $\rho\,(T)$ curves of a sample of Nb_3Al under different magnetic field values in T (shown in blue) [23]. It is possible to see how T_c decreases as the the applied field increases.

completely suppressed above this field value. In contrast, in type-II superconductors the application of a magnetic field above a lower critical magnetic field H_{c_1} results in the presence of cylindric normal cores in the superconducting bulk [24], until at the upper critical magnetic field H_{c_2} superconductivity is completely suppressed. In particular, between H_{c_1} and H_{c_2} there is a continuous increase in the flux penetration and this condition is called “mixed state” or “Schubnikov phase”. In the mixed state, the field penetrates in a regular array of flux tubes (called “fluxons”), each carring a quantum of flux $\Phi_0 = \dfrac{h}{2e}$, where h is the Planck constant and e the electronic charge. The magnetic flux within each core is generated by a vortex of supercurrents that circulates around the core (fig. 1-3).

In all the different classes of superconductors the electrons form pairs in order to superconduct. However, the fundamental physical mechanisms that provide this coupling may differ and not all the mechanisms have been fully understood yet. Only for the so called “conventional” superconductors a detailed quantitative theory is available since a long time. According to the BCS (Bardeen-Cooper-Schrieffer) theory, that will be summarized in sec. 1.1, electrons interact with each other via the vibrations of the crystal lattice. All superconducting elements and many other Low

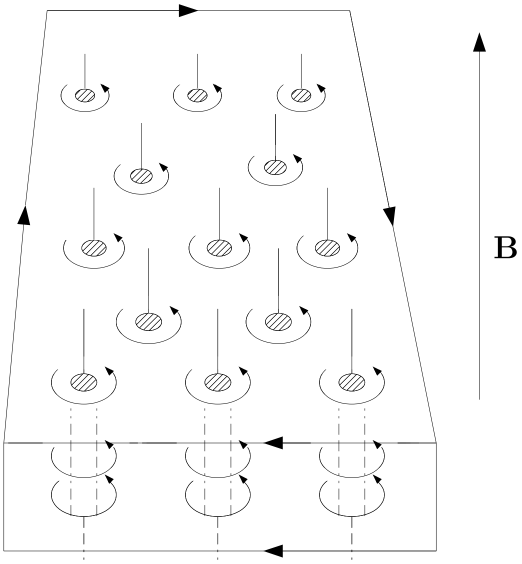

Figure 1-3: Schematic diagram of vortex in the Shubnikov phase.

Temperature Superconductors (LTS) are conventional superconductors. Instead, understanding the origin of superconductivity of the High Temperature Superconductors (HTS) is a premier challenge of the recent research.

Despite the advent of the HTSs, a lot of attention still remains also on the LTSs. This thesis work is devoted to the study of an LTS superconductor, the binary compound Nb_3Sn, a relative of the aforementioned Nb_3Ge, discovered in 1954 and with a critical temperature of about 18 K [25]. This material is supposed to be well known and is still the most widely used superconductor for high field magnets. However, there are many reasons for the revived interest in this material.
Nb_3Sn is a particularly promising material for replacing Nb in superconducting radiofrequency (SRF) cavities [26] for future particle accelerators that require higher magnetic fields to achieve higher luminosities than those reachable with Nb, material of choice by far, that is operating almost to its limits. Indeed, SRF Nb cavities suffer a decreasing quality factor, Q, with the increasing RF accelerating voltage. The need to eliminate this Q degradation led to the consideration of other superconducting materials for coating of the Nb cavities, characterized by lower surface resistance in RF fields. Nb_3Sn, with its higher critical temperature T_c and lower surface resistance

at 4.2 K, allows to increase the Q values (inversely proportional to the surface resistance) by a factor $\sim 10^2$ with respect to Nb cavities.

Moreover, in the field of modern particle accelerators, Nb_3Sn is also considered for the superconducting magnets necessary to steer the high energy particle beams. An important example of this application is the High-Luminosity Large Hadron Collider (HL-LHC) accelerator project at CERN, where high-field magnets based on Nb_3Sn with a usable magnetic field of around 12 T are the choice for the beam focusing and bending [1, 27, 28].

Another example is the Future Circular Collider (FCC), also at CERN. The goal of the FCC is to greatly push the energy and intensity frontiers of particle colliders to extend the research currently being conducted at LHC, with the aim of reaching collision energies of 100 TeV. In this case, a field of 16 T, necessary to steer a 50 TeV beam over a 100 km long tunnel, is the final goal to be reached [29].

Nb_3Sn is also the superconductor of choice for high field magnets to be used for plasma confinement in fusion reactors. The International Thermonuclear Experimental Reactor (ITER) project envisages the central solenoid (which reaches magnetic field values up to 13.5 T) and toroidal field superconducting magnets based on Nb_3Sn [2] [3].

Another important application of Nb_3Sn is in the Nuclear Magnetic Resonance (NMR) spectrometers, very important analysis tools in medicine, chemistry and material science, which use fields up to 23.5 T [4].

Using Nb_3Sn to make high field magnets is not trivial because it is very brittle and then susceptible to mechanical damage. In high field applications the magnets need to withstand large mechanical forces, with overwhelming difficulties in the magnet engineering. However, for very-high fields applications other superconductors, such as NbTi, are not sufficient, while Nb_3Sn remains superconducting up to magnetic fields above 20 T and then it represents a unique technology (no alternatives exist yet) for the listed high magnetic field applications. Indeed, also if HTSs could reach magnetic fields even larger than 20 T, the technology based on these materials is significantly more expensive than that based on Nb_3Sn and moreover, a lot of work to optimize the stress management, quench protection and fabrication methods has to be done yet. This fact revamped the interest in Nb_3Sn leading to new researches particularly addressed to the relationship between superconducting properties and mechanical stress.

In addition to the large scale applications that are already current or planned for the future, a more fundamental reason for studying of Nb_3Sn is that, in spite of previous scientific research spanning several decades, there are still features that are not yet fully understood. For example, recent investigations on Nb_3Sn revealed that it could be a new example of two-gap superconductivity [30]. Also the effect of strain and compositional disorder on its superconducting properties are vaguely understood till now [31].

Superconductivity is framed in different theories, of different complexity, and providing an exhaustive discussion overcomes the purpose of this thesis. In this first chapter a general discussion on superconductivity will be given, focusing only on some aspects of the theories of superconductivity relevant to this thesis.

1.1 The Bardeen-Cooper-Schrieffer theory

The first microscopic theory of superconductivity, still valid for describing the physics of low T_c superconductors, was developed in 1957 by the American physicists John Bardeen, Leon N. Cooper and J. Robert Schrieffer [3]. In this theory, since then referred to as the BCS theory, the energy of the normal state can be lowered by having the electrons at the top of the Fermi sea condense into a superconducting state where the electrons form pairs in momentum space.

The idea of paired electrons dates back to 1950/51, when an interaction between the electrons mediated by the vibrations of the lattice was for the first time proposed simultaneously and independently by Fröhlich [32] and Bardeen [33]. At the same time, the experimental discovery of the dependence of the critical temperature on the isotopic mass of the lattice M in mercury [34, 35], the "isotope effect", for which

---

[3] Nobel Prizes in physics 1972

$T_c \sim M^{1/2}$, came to support the Fröhlich's suggestion that superconductivity involves lattice vibrations. Following the idea that the interaction between the electrons can be mediated by phonons, in 1956 Leon Cooper demonstrated that an arbitrarily small attraction between electrons in a metal could cause a paired state of electrons ("Cooper pairs") to have a lower energy than the Fermi energy, which implies that the pair is bound [36]. In BCS theory this attraction is due to the electron-phonon interaction proposed by Fröhlich and Bardeen.

The attractive interaction between electrons, mediated through the lattice vibrations, can be described by the following picture. Conduction electrons propagate through the lattice of the atomic ions of a material. For simplicity, let's look at only two electrons within this lattice of atomic ions and ignore all other electrons. The negative charge of both electrons will slightly distort the lattice by attracting the surrounding positive charges. This polarization of the lattice leads to an accumulation of positive charge near the polarizing negative charge. This leads to an effective attractive interaction between the two electrons causing them to "pair up" into a Cooper pair. A Cooper pair consists of two electrons with opposite momentum of equal magnitude and with opposite spins. The spacing between the two electrons in the pair is typically several hundred or a thousand times the interatomic spacing and in the BCS theory it is represented by the coherence length ξ_0. The interaction is retarded since the attractive interaction occurs via phonons which travel with finite speed while, on this time scale, the Coulomb repulsion between the electrons can be considered nearly instantaneous. The strength of the polarization, and hence of the interaction, depends on the characteristic frequency of the lattice and, therefore, also on the mass of the atomic ions. This results because the polarization takes place along the way of the electrons and sensitively depends on how quickly the lattice can follow the polarizing action of them. By thinking at the time during which the lattice of atomic ions can respond to any displacements, one qualitatively explains also the 'isotope effect': heavier isotopes oscillate more slowly and then follow the polarizing action more slowly compared to lighter isotopes. This results in a smaller T_c.

In the BCS theory, the attractive potential introduced to describe the pairing of electrons takes the form:

$$\langle k, \sigma \left| V\left(q\right) \right| k', \sigma' \rangle = -V \delta_{k,-k'} \delta_{\sigma,-\sigma'}, \tag{1.1}$$

where k and k' are the momenta and σ and σ' are the spin indices of the elctrons. The potential V is assumed to be constant and it applies for electrons in an energy range $\pm\hbar\omega_D$ centered about the Fermi surface, where ω_D is the Debye frequency. Everywhere else the interaction is assumed to be zero. The electrons involved in the pairing mechanism are described by a free electron type wave function. The Hamiltonian that describes the system in the BCS theory is the so-called "reduced" or "pairing" Hamiltonian, which may be expressed in the form:

$$H_{red} = \sum_{\mathbf{k}\sigma} \varepsilon_{\mathbf{k}} n_{\mathbf{k}\sigma} + \sum_{\mathbf{kl}} V_{\mathbf{kl}} c^*_{\mathbf{k}\uparrow} c^*_{-\mathbf{k}\downarrow} c_{-\mathbf{l}\downarrow} c_{\mathbf{l}\uparrow} \tag{1.2}$$

where $\varepsilon_{\mathbf{k}}$ is the energy of one free electron, and the c^* and c are the electron creation and annihilation operators. The term $V_{\mathbf{kl}}$ scatters from a state with $(-\mathbf{l}\downarrow, \mathbf{l}\uparrow)$ to one with $(-\mathbf{k}\downarrow, \mathbf{k}\uparrow)$.

The BCS ground state wave function has the form:

$$|\psi_G\rangle = \prod_{\mathbf{k}} \left(u_{\mathbf{k}} + v_{\mathbf{k}} c^*_{\mathbf{k}\uparrow} c^*_{-\mathbf{k}\downarrow} \right) |\phi_0\rangle. \tag{1.3}$$

Here, $|\phi_0\rangle$ refers to the vacuum state and the factors $u_{\mathbf{k}}$ and $v_{\mathbf{k}}$ are related to probabilities of occupation. In particular, if the probability of the pair $(\mathbf{k}\uparrow, -\mathbf{k}\downarrow)$ being occupied is $|v_{\mathbf{k}\uparrow}|^2$, from the normalization of $|\psi_G\rangle$, the probability that it is unoccupied is $|u_{\mathbf{k}\uparrow}|^2 = 1 - |v_{\mathbf{k}\uparrow}|^2$. BCS obtained the two factors $u_{\mathbf{k}}$ and $v_{\mathbf{k}}$ starting from the Hamiltonian (1.2) and applying the variational method, as described in [37]. The result is that these factors depend on the energy gap Δ, that is predicted by the theory to exist between the superconducting ground state and the excited states, according to the following formulas:

$$|v_{\mathbf{k}}|^2 = \frac{1}{2}\left[1 - \frac{\varepsilon_{\mathbf{k}} - E_F}{\left(\varepsilon_{\mathbf{k}} - E_F\right)^2 + |\Delta|^2}\right], \tag{1.4}$$

$$|u_{\mathbf{k}}|^2 = 1 - |v_{\mathbf{k}}|^2 = \frac{1}{2}\left[1 + \frac{\varepsilon_{\mathbf{k}} - E_F}{(\varepsilon_{\mathbf{k}} - E_F)^2 + |\Delta|^2}\right]. \tag{1.5}$$

By assuming that the system is isotropic and that the electronic density of states is constant in the narrow region where the potential acts, the energy gap and the energy of the superconducting state at zero temperature are determined by the following formulas:

$$\Delta_0 = \frac{\hbar\omega_D}{\sinh\left[1/N_{E_F}V\right]} \approx 2\hbar\omega_D \exp\left(-\frac{1}{VN_{E_F}}\right) \tag{1.6}$$

and

$$U_{sc}(0) = U_n(0) - \frac{1}{2}N_{E_F}\Delta^2(0), \tag{1.7}$$

where $U_{sc}(0)$ and $U_n(0)$ are the internal energy of the system in the superconducting and normal state, respectively. The last step in (1.6) holds in the so-called weak-coupling limit $N_{E_F}V \ll 1$. The quantity $U_{sc}(0) - U_n(0)$ is the condensation energy and it represents the energy gain when Cooper pairs form.

The excited states of the system are formed by broken Cooper pairs, where each electron is a *quasiparticle*. Indeed, by means of a Bogoliubov-Valatin canonical transformation (see [37] for the details of calculations) on the terms of H_{red}, it has been demonstrated also that the energy of the excited states $E_{\mathbf{k}}$ with respect to the Fermi level is given by:

$$E_{\mathbf{k}} = \sqrt{(\varepsilon_{\mathbf{k}} - E_F)^2 + |\Delta|^2}. \tag{1.8}$$

Since the energy of a quasiparticle is $E_{\mathbf{k}}$, the minimum energy required to create a new excitation is Δ, and since quasiparticles are created in pairs, the minimum energy required to break a Cooper pair and then to create an excitation from the ground state is 2Δ.

For conventional superconductivity the pair wave function has an isotropic s-wave symmetry. This is because the two electrons of the Cooper pair form a state in which the value S and L (that are the total spin and the total angular momentum) of the pair vanishes. The energy gap then results to be approximately independent on the wave vector $\mathbf{k}$ of the electrons, that is that the generation of a quasiparticle with wave vector $\mathbf{k}$ costs an energy Δ approximately equal for all directions of $\mathbf{k}$.

The dependence of the energy gap on the temperature is determined by the following equation [37]:

$$\frac{1}{V} = \frac{1}{2}\sum_{\mathbf{k}} \frac{\tanh\left(k_B T E_{\mathbf{k}}/2\right)}{E_{\mathbf{k}}}, \tag{1.9}$$

where k_B is the Boltzmann constant.

The critical temperature T_c is determined by the condition that, at T_c, $\Delta\left(T\right) \rightarrow 0$. It results that:

$$k_B T_c = 1.13\hbar\omega_D \exp\left(-\frac{1}{N\left(E_F\right)V}\right). \tag{1.10}$$

Then, the transition temperature is proportional to $\hbar\omega_D$, which is consistent with the isotope effect, and is also a strong function of the electron concentration since the density of states at the Fermi level enters exponentially.

The equations (1.6) and (1.10) combined give the ratio:

$$\frac{2\Delta_0}{k_B T_c} = 3.53, \tag{1.11}$$

which is independent from material dependent quantities other then Δ_0 and T_c. This ratio holds in the weak-coupling limit, that is, as said above, when $N_{E_F}V \ll 1$. Most materials deviate from this BCS relation and, in most cases, the failure derives from the choice of a constant interaction potential between the paired electrons, in which the details, such as the retarded nature of the phonon-induced interaction are ignored.

For this thesis work, partly devoted to the study of the effect of an applied pressure on the properties of Nb_3Sn, it is interesting to understand the effect of pressure on the superconducting properties of a BCS material. From Eq. (1.10) also the pressure dependence of the critical temperature can be understood. The parameters ω_D and N_{E_F} depend on the lattice parameter and hence will change with pressure. Since pressure reduces the interatomic distances, ω_D increases with pressure (phonon hardening) and then T_c is expected to increase too. On the other hand, reducing the average distance between the atoms leads to a band broadening that, in a metal means a lowering of N_{E_F}, and then of T_c. However, the pressure dependence of N_{E_F} can be different, depending on the details of the Fermi surface of a particular compound. Nonlinearities in the pressure dependence of T_c have been observed in correspondence to changes in the topology of the Fermi surface (and this is also related to changes in N_{E_F}). What results is therefore a competition between different mechanisms that are difficult to identify uniquely and that, to be understood, require the combination of investigation techniques and complementary models. This discussion will be resumed later, in sec. 2.2.1.

1.2 The Eliashberg Theory

Nb_3Sn is a strong coupling superconductor so that it deviates from the ratio given by (1.11). This means that the approximation that led to T_c (Eq. (1.10)) is not appropriate for obtaining the critical temperature of Nb_3Sn and it is necessary to extend the theory including adequate corrections. This can be done using the Eliashbergh model whose salient features will be described in this section.

The original BCS theory, valid in the weak-coupling regime, had little to do with the details of the attractive mechanism, but rather succeeded in establishing the pairing formalism which lead to a superconducting state once some attractive interaction is established. In particular the BCS equation (1.10) turned out to be inadequate for superconductors in which the electron-phonon interaction is strong. A primary reason for this is the instantaneous nature of the BCS interaction which does not incorporate enough of the physics of the electron-phonon interaction. For example, the electron-phonon interaction causes a mass enhancement of electron states near the Fermi level and a finite lifetime of electron quasiparticle states. In many materials these effects are strong and well-defined quasiparticles no longer exist.

The Eliashberg theory [38] extended the original BCS theory emphasizing the electron-ion interaction (the mechanism by which Cooper pairs form) in which the details of the lattice and of the phonon dispersion curves play a crucial role. In this theory, proposed in 1960, Eliashberg used a Green's function approach to incorporate the details of the electron-phonon interaction into the theory of superconductivity. The result was a theory that could explain the deviations from the universal BCS relation (1.11) for most materials.

The important parameters introduced by the Eliashberg theory are the spectral function $\alpha^2 F(\omega)$ and the Coulomb pseudopotential μ^*. The spectral function contains the electron-phonon coupling, $\alpha^2(\omega)$, and the phonon density of states $F(\omega)$. The parameter μ^* represents a "renormalized" Coulomb repulsion between the coupled electrons. This is reduced in value from the Coulomb repulsion μ to:

$$\mu^* = \frac{\mu}{\left[1 + \ln\left(\frac{\omega_P}{\omega_D}\right)\right]}. \tag{1.12}$$

This suppression of the Coulomb repulsion results from the fact that the electron-phonon attraction is retarded in time by an amount $\Delta t \approx \dfrac{1}{\omega_D}$, whereas the repulsive screened Coulomb interaction between electrons is retarded by a much smaller time, $\Delta t \approx \dfrac{1}{\omega_P}$, where ω_P is the electronic plasma frequency.

The equilibrium superconducting properties, namely the critical temperature T_c and the energy gap Δ, can be derived from the knowledge of the spectral function $\alpha^2 F(\omega)$, that is expressed as:

$$\alpha^2 F(\omega) = \frac{1}{N_{E_F}} \sum_j \delta(\omega - \omega_{\mathbf{q}j}) \sum_{k,k'} \left|g(\mathbf{k}, \mathbf{k}'; \mathbf{q}j)\right|^2 \times \delta(E_k - E_F)\,\delta(E'_k - E_F), \tag{1.13}$$

where $g(\mathbf{k}, \mathbf{k}'; \mathbf{q}j)$ are the electron-phonon coupling matrix elements. The spectral function measures the contribution of phonons with frequency ω to the scattering processes of electrons at the Fermi level and is related to the dimensionless electron-phonon coupling parameter λ through the formula:

$$\lambda = 2\int_0^\infty \frac{\alpha^2 F(\omega)}{\omega} d\omega \tag{1.14}$$

which corresponds roughly to the product $N_{E_F}V$ of the original BCS formula.

Within the Eliashberg theory, McMillan obtained the following analytical formula for

T_c [39]:

$$T_c = \frac{\Theta_D}{1.45} \exp\left[-\frac{1.04\left(1+\lambda\right)}{\lambda - \mu^*\left(1+0.62\lambda\right)}\right] \tag{1.15}$$

where Θ_D is the Debye temperature and μ^* is the reduced Coulomb repulsion experienced by a Cooper pair described above. This formula is highly accurate for materials with $\lambda < 1.5$, but by predicting an upper limit for T_c, it underestimates T_c for large values of the coupling parameter λ, which occur in lattices with relatively soft phonons (e.g. Nb_3Sn). It can be shown that the reason of such failure resides in the fact that (1.15) was not derived analitically but obtained by numerical solutions in a fixed range of the coupling parameter.

The formula (1.15) was improved by Allen and Dynes [40], who substituted the factor $\frac{\Theta_D}{1.45}$ with $\frac{\omega_{log}}{1.20}$, where the frequency:

$$\omega_{log} = \exp\left[\frac{2}{\lambda}\int d\omega \log\omega \frac{\alpha^2 F\left(\omega\right)}{\omega}\right], \tag{1.16}$$

is a weighted average of the phonon frequencies. The new expression of T_c, although not obtained analitically, allows to correctly estimate T_c for all conventional superconductors that exhibit strong coupling and “high” T_c (here “high” means a T_c greater than ~5 % of Θ_D or $\lambda \geq 1.2$). Table 1.1 reports the critical temperature T_c, the ratio $\frac{2\Delta\left(0\right)}{k_B T_c}$, the upper critical magnetic field at 0 K $H_{c_2}\left(0\right)$, the Debye temperature Θ_D and the experimental and theoretical electron-phonon coupling parameter λ for selected strong coupling superconductors that are well described in the context of the Eliashberg theory.

1.3 Notes on the Ginzburg-Landau theory

Many material parameters can be introduced by referring to a simpler theoretical framework than the BCS and Eliashberg theories. Moreover, the BCS theory works well when some quantities related to the superconducting state, such as the density of superconducting electrons n_s or the superconducting gap Δ, are spatially homoge-

Table 1.1: Critical temperature T_c, energy gap to T_c ratio $\frac{2\Delta(0)}{k_B T_c}$, upper critical magnetic field at 0 K $H_{c_2}(0)$, Debye temperature Θ_D and experimental and theoretical electron-phonon coupling parameter λ for selected strong coupling superconductors [41–48].

	T_c (K)	$\frac{2\Delta(0)}{k_B T_c}$	$H_{c_2}(0)$ (T)	Θ_D (K) ($T \to 0/T > T_c$)	λ_{exp}	λ_{th}
Nb	9.2	3.8	0.82	277	1.22	1.33
Pb	7.2	4.4	0.08	105	1.55	1.68
Al	1.19	3.35	0.01	428	0.42	0.45
Nb_3Sn	18.3	4.2	24.5	208	1.80	1.78
Nb_3Al	18.7	4.4	32.4	283	1.7	1.59
Nb_3Ge	23.2	3.9	38	302	1.7	1.80
V_3Si	16.9	3.8	2.35	324	1.29	1.18

neous. However there are situations in which these quantities are not homogeneous, for example in the mixed state of type II superconductors, such as Nb_3Sn. This deficiency of the BCS theory was overcome in 1950 by Vitaly Lazarevich Ginzburg and Lev Landau who proposed a theory (the G-L theory) that accounts for spatial variations in n_s due to the presence of a magnetic field [37, 49].

The G-L theory introduces a complex order parameter, $\psi(\mathbf{r})$, whose square modulus represents the density of superconducting electrons, i. e. $|\psi(r)|^2 = n_s$. This order parameter is defined so as to be zero for $T > T_c$ and unity at $T = 0$.
Near T_c, where ψ approaches to zero, the free energy of the superconducting phase g_s is expanded in a Taylor series of $|\psi(r)|^2$ as follows:

$$
\begin{aligned}
g_s = g_n + \alpha(T)\,|\psi(\mathbf{r})\,|^2 + \frac{\beta(T)}{2}\,|\psi(\mathbf{r})|^4 + \\
+ \frac{\hbar^2}{2m}\left|\left(\nabla - \frac{ie}{\hbar}\mathbf{A}(\mathbf{r})\right)\psi(\mathbf{r})\right|^2 + \left(\frac{B^2(\mathbf{r})}{2\mu_0} - \mu_0\mathbf{M}(\mathbf{r})\cdot\mathbf{H_0}\right)
\end{aligned}
\tag{1.17}
$$

where g_n is the free energy in the normal phase, m and e are the charge carrier mass and charge, $\mathbf{A}$ is the magnetic vector potential, $\mathbf{B} = \nabla \times \mathbf{A}$ is the magnetic induction and $\mathbf{M}$ is the magnetization in presence of an applied magnetic field $\mathbf{H}_0$. The last two terms in Eq. (1.17) are the kinetic energy in the Coulomb gauge form and the energy that the system pays to expel the magnetic field from its interior. α and β are two phenomenological parameters expressed by the relations:

$$\alpha(T) = \alpha_0 (T - T_c) \qquad \text{with} \qquad \alpha_0 > 0 \qquad \text{and} \tag{1.18}$$

$$\beta(T) = \beta_0 \qquad \text{with} \qquad \beta_0 > 0. \tag{1.19}$$

If $\psi = 0$ in Eq. (1.17), the free energy reduces to that of the normal state in presence of a magnetic field.

By minimizing the free energy with respect to variations in the order parameter and the vector potential, the following Ginzburg-Landau differential equations are obtained:

$$\psi(\mathbf{r})\left(\alpha + \beta|\psi(\mathbf{r})|^2\right) + \frac{\hbar^2}{2m}\left|\left(\nabla - \frac{ie}{\hbar}\mathbf{A}\right)\psi(\mathbf{r})\right|^2 = 0 \tag{1.20}$$

$$\mathbf{J_s}(\mathbf{r}) = \frac{e}{m}\left[\hbar\nabla\phi(\mathbf{r}) - e\mathbf{A}(\mathbf{r})\right]|\psi(\mathbf{r})|^2, \tag{1.21}$$

where $\mathbf{j}_s$, the dissipationless supercurrent density, has been introduced by virtue of the Maxwell equation $\nabla \times \mathbf{B} = \mu_0 \mathbf{j}$.

In absence of magnetic fields and gradients there is no superconducting current $\mathbf{j}_s$ and Eq. (1.20) simplifies to:

$$\alpha\psi + \beta|\psi|^2\psi = 0. \tag{1.22}$$

This equation has two solutions depending on the sign of α. Above T_c, $\alpha > 0$, and the minimum free energy occurs at $|\psi|^2 = 0$, that corresponds to the normal state. Below T_c, $\alpha < 0$, and the free energy has its minimum at:

$$|\psi|^2 = |\psi_\infty|^2 = -\frac{\alpha}{\beta} = -\frac{\alpha_0 (T - T_c)}{\beta_0}, \tag{1.23}$$

where ψ_∞ is the equilibrium value of ψ at the interior of the superconductor, far away from any interface, and it approaches zero as T gets closer to T_c from below, as expected.

The Ginzburg-Landau equations predicted two characteristic lengths in a superconductor. One is the *coherence length*, ξ:

$$\xi = \sqrt{\frac{\hbar^2}{2m\left|\alpha\left(T\right)\right|}}, \tag{1.24}$$

and the other is the *penetration depth*, λ:

$$\lambda = \sqrt{\frac{m}{4\mu_0 e^2 \left|\psi_\infty\right|^2}}. \tag{1.25}$$

ξ and λ represent the distance over which $\psi\left(\mathbf{r}\right)$ and $B\left(\mathbf{r}\right)$ decay when non-homogeneities are introduced (for example at an interface or in presence of fluxons). The coherence length and the penetration depth define the dimensionless G-L parameter κ:

$$\kappa = \frac{\lambda}{\xi}, \tag{1.26}$$

that is independent on the temperature and on the magnetic field. This parameter allows to distinguish from a type I and a type II superconductor. Indeed, κ is related to the critical magnetic fields of a superconductor by the relation:

$$H_{c_2} = \sqrt{2}\kappa H_c. \tag{1.27}$$

Eq. (1.27) means that type I superconductors are those with $0 < \kappa < 1/\sqrt{2}$, and type II superconductors are those with $\kappa > 1/\sqrt{2}$. Nb_3Sn, with its high values of κ, that range from $\sim$20 to $\sim$ 40 based on the composition [50], is a type II superconductor.

In the next chapter some of the properties of Nb_3Sn, and of other superconducting compounds belonging to the same structural family (all named “A15” compounds) will be reviewed. Particular attention will be given to the results concerning the structural properties of these materials, and how these relate to the superconducting ones. Furthermore, the effects of pressure on superconductors in general, and more specifically on A15 materials, will be discussed.

Chapter 2

A15 materials

The superconductors with the β-tungsten structure (also known as A15 or Cs_3Si structure) are technologically high-relevant materials. Among them is Nb_3Sn, the workhorse for the high field magnets (see chap. 1). Superconductivity in A15 materials was observed for the first time by Hardy and Hulm in 1953 [51] [52] on silicides and germanides: among them, V_3Si, with the highest critical temperature known at that time for any binary compound (T_c=17.1 K), Mo_3Si (T_c=1.30 K), V_3Ge (T_c=6.01 K) and Mo_3Ge (T_c=1.43 K). This discovery led researchers to test several intermetallic compounds of this structure. Among these, Matthias *et al.* [25] discovered Nb_3Sn in 1954, reporting for their samples an onset of superconductivity at 18.05 K. Another representative of this group, namely Nb_3Ge with $T_c = 23.2$ K [53] [15], held the record of the highest transition temperature for a long time, until the discovery of the high-temperature superconductors [16].

Among the A15 materials, Nb_3Sn is currently the most used in the construction of high field magnets because it has H_{c_2} which is twice that of NbTi (the only material used for superconducting magnets until recently) allowing to reach values of higher magnetic field necessary for example, as already seen in chapter 1, in particle accelerators, in nuclear fusion reactors and in NMR spectrometers. Despite having superior superconducting properties and the fact that Nb_3Sn has been discovered eight years before NbTi, it has not been considered for high field applications until recently. The reason lies entirely in the mechanical properties of Nb_3Sn that, unlike NbTi which

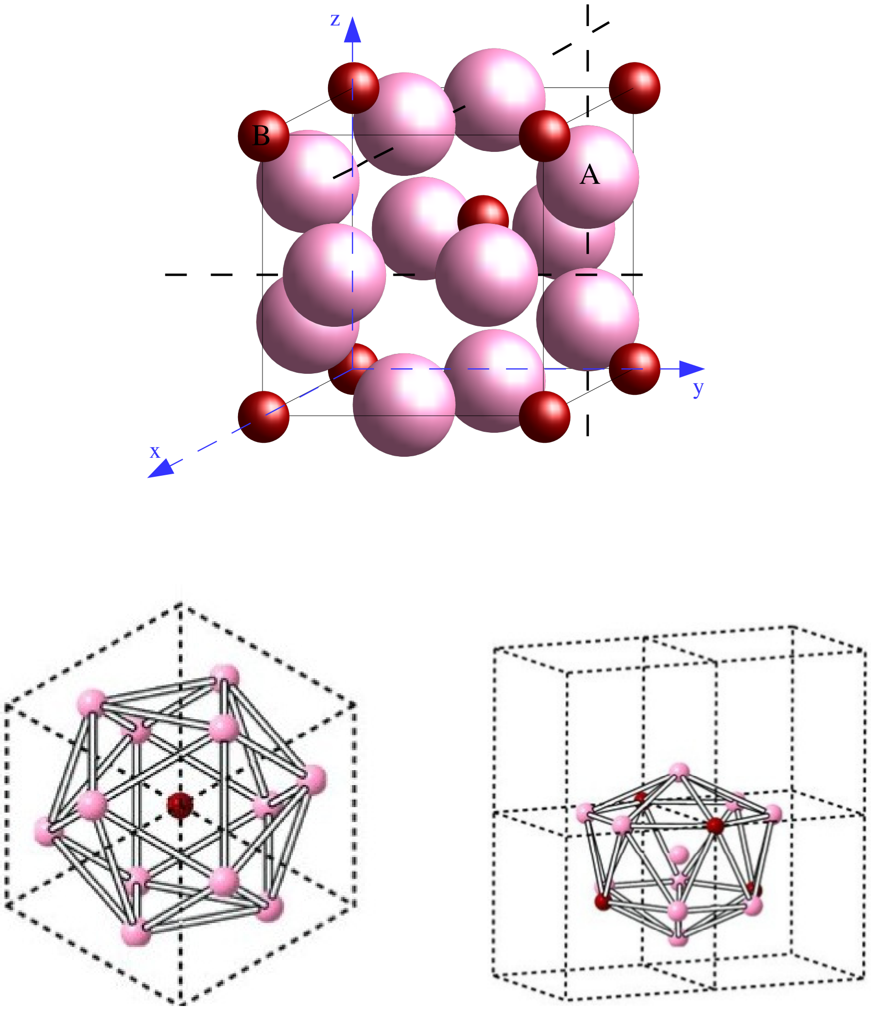

Figure 2-1: (Top) The unit cell of A_3B compounds. A atoms are dark red coloured, B atoms are pink. (Bottom left) The coordination environment of B atoms and (Bottom right) A atoms.

is a ductile alloy, is a very brittle material. This feature is an inherent source of stress-strain dependence of its superconducting properties and required a deep effort to optimize the fabrication method of Nb_3Sn wires.

A15 materials have chemical formula A_3B (where A is a transition metal and B is often a non-transition metal atom). Figure 2-1-top shows the crystal structure of the A15 compounds (A_3B). It has a cubic unit cell of eight atoms and belongs to the space group $Pm3n$ (O_h^3 in the Schoenflies notation). Lattice parameters of A15 superconductors range from 4.72 Å for V_3Si to 5.29 Å for Nb_3Sn. The A-type and B-type atoms occupy the 6c and 2a Wyckoff positions of the space group, respectively. In

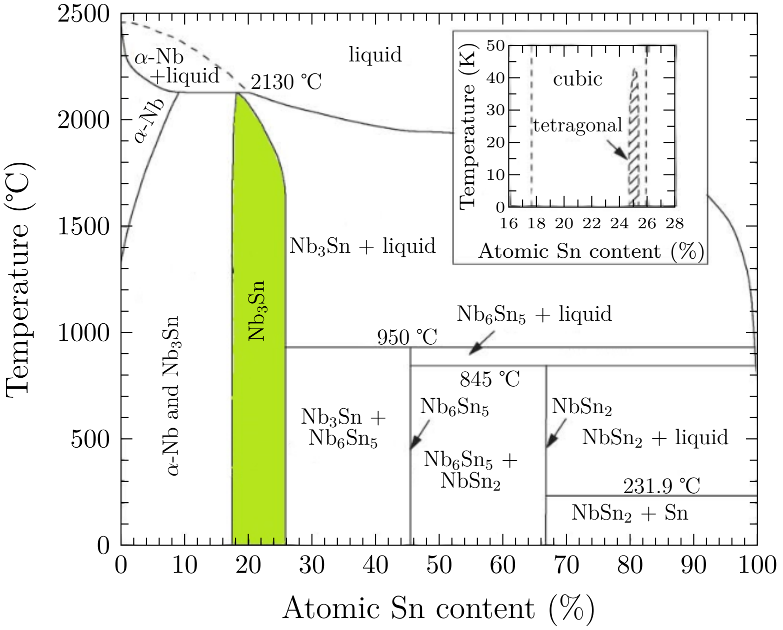

Figure 2-2: Niobium-Tin phase diagram after Charlesworth *et al.* [54].

particular, the B atoms form a body-centered cubic (bcc) lattice, while the A atoms occur on the cube faces and are arranged along chains parallel to the x, y, and z axes, at the positions $0\frac{1}{4}\frac{1}{2}$, $0\frac{3}{4}\frac{1}{2}$, $\frac{1}{2}0\frac{1}{4}$, $\frac{1}{2}0\frac{3}{4}$, $\frac{1}{4}\frac{1}{2}0$ and $\frac{3}{4}\frac{1}{2}0$. On each chain the A-type atoms distribute equidistantly and the orthogonal chains do not intersect. The A atoms have a coordination number of 2 and the B atoms of 12. In fig. 2-1 (bottom left and right), the coordination environment of the B and A atoms are represented. The Wigner-Seitz cells are a 12-hedron for B atoms and a 14-hedron for A atoms.

2.1 Physical properties of Nb_3Sn

2.1.1 Phase Diagram

In this section the phase diagram of the compound of interest for this thesis, Nb_3Sn, will be described.

In fig. 2-2 the binary phase diagram of $Nb_{1-\beta}Sn_\beta$ is depicted [54]. In thermodynamic equilibrium, three different intermetallic phases can form, depending on the value of

β, namely Nb_3Sn, $NbSn_2$ and Nb_6Sn_5. The A15 phase can exist in the wide composition range $0.18 \leq \beta \leq 0.25$ at. % Sn (green-coloured in fig. 2-2). In the insert of fig. 2-2, a zoom of the diagram is shown in the composition range from 0.18 to 0.25 at. % Sn, where it can be seen that Nb_3Sn with almost stoichiometric composition shows a tetragonal structure for temperatures lower than 40 K. The highest transition temperature is found in this compound at the edge of the stability range (temperature and composition) of the A15 phase. A deviation from stoichiometry reduces the superconducting transition temperature due to the resulting compositional disorder. In fig. 2-2 there are two other superconducting phases of the binary compound Nb-Sn, Nb_6Sn_5 and Nb_6Sn_2. However, their T_c is below 3 K, and thus they are of negligible interest for pratical applications.

2.1.2 The Batterman-Barrett Transformation

Upon cooling, many A15 superconductors exhibit a lattice transformation below a temperature $T_L > T_c$. This transition, also known as Batterman-Barrett transformation [55], is of first order and consists of a weak tetragonal distortion of the originally cubic unit cell (a shear strain distortion) accompanied by a dimerization of the atoms along the transition metal chains. The new phase belongs to the $P4_2/mmc$ (D^9_{4h} in the Schoenflies notation) space group. Generally the structural transformation occurs at a temperature T_L which is higher than T_c but not more than a factor two. However, the tetragonal transition does not occur suddenly at T_L, but precursor effects start even at higher temperatures.

The first evidence of such transition in A15 compounds was found in V_3Si [55], then it has been detected on V_3Ga and Nb_3Al by means of heat capacity measurements by Viswanathan *et al.* in 1974 [56], at 13 K and 15 K, respectively.

Nb_3Sn undergoes the cubic to tetragonal structural transition at about 40 K as shown for the first time by Keller and Hanak [57]. Mailfert *et al.* with their diffraction experiment determined a ratio a/c =1.0062, while $a = b$ [58] (see fig. 2-3).

Shirane and Axe [59], by means of neutron scattering experiments on Nb_3Sn have

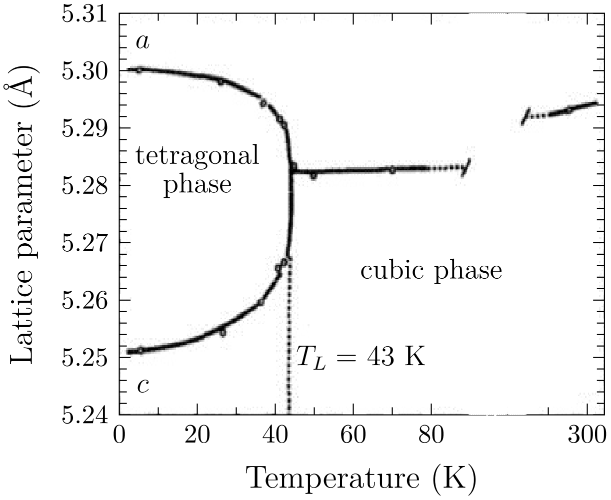

Figure 2-3: Lattice parameter versus temperature for Nb_3Sn single crystal determined by Mailfert *et al.* [58].

established the existence of a sublattice displacement below T_L. They observed that the Nb sublattices shift and that the sublattice displacement in the tetragonal structure is of symmetry type $\Gamma_{12}(+)$, as in fig. 2-4, where the Nb atoms of the chains in the y-direction in a cell move toward each other, those in the x direction move away the same amount and those in the z direction remain uniformly spaced. The redistribution of the Nb atoms along two chains is called *dimerization* and can be described as a Peierls instabilty [60–63]. In a Peierls instability charge density waves (CDWs) develop and a gap ("Peierls gap") opens up at the Fermi level as a consequence of the dimerization of linear chains of atoms (see appendix A for a description of the Peierls mechanism in 1D). In the case of Nb_3Sn N_{E_F} is reduced, because of the opening of the Peierls gap, and then also the number of electrons available for BCS pairing: the immediate consequence of this fact is the reduction of T_c.

The cause of the structural instability is assumed to lie in the electron system of the transition metal atom chains. Labbé and Friedel [64] proposed a linear chain model to explain the relatively high T_c of the A15 compounds and their structural instability. The model emphasises the importance of the d-electrons of the transition metal ions forming the characteristic orthogonal chains. All the interactions between chains, or between A and B atoms, are neglected. Since the three chains along three different

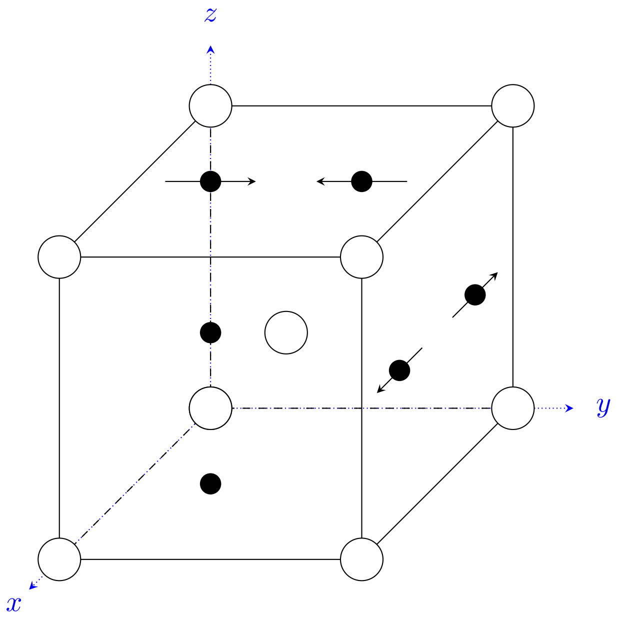

Figure 2-4: Model of the Nb atom sublattice shift due to the Batterman-Barrett transformation in Nb_3Sn (full circles Nb; empty circles Sn) [59].

directions lead to an identical DoS, the system carries a threefold degeneracy. Therefore, the Fermi energy is close to a singularity of the electronic density of states, due to the cubic symmetry. This leads to the increase in T_c, but simultaneously favours the lowering of the energy of the system through a tetragonal structural change (symmetry reduction) in which the degeneracy of the d-band structure is partly lifted. The structural distortion with suppression of degeneracy of the d-bands constitutes a Jahn-Teller transformation [65].

The tetragonal transition negatively affects the critical temperature because of the Peierls distortion. The superconducting transition, in turn, also affects the tetragonal transition. It has been observed that the developing tetragonality upon cooling is interrupted at the transition to superconductivity and that if the superconducting transition occurs already in the cubic phase, the martensitic transition is completely suppressed [66]. To understand the relation between tetragonality and superconductivity in Nb_3Sn, we consider the formula (1.14) again. It can be re-expressed as:

$$\lambda = \frac{N_{E_F}\langle I^2\rangle}{M\langle\omega^2\rangle}, \tag{2.1}$$

where M is the average atomic mass and $\langle I^2 \rangle$ and $\langle \omega^2 \rangle$ are, respectively, averages of the electron-phonon matrix element and squared phonon frequency. One effect, already mentioned in this section, is that through the Peierls gap formation, the tetragonal transition reduces N_{E_F}, thus lowering λ and hence T_C, which depends on λ exponentially (Eq. (1.15)). Another effect, is that phonon softening in the vicinity of the transition reduces $\langle \omega^2 \rangle$, thus raising λ and hence T_c. The relation between tetragonality and superconductivity arises from a competition between the BCS and Peierls gaps for a common portion of the Fermi surface. If the electron-phonon coupling for the Peierls gap λ_L, defined analogously to (2.1), exceeds that for superconductivity λ, T_L occurs above T_c and is given by:

$$T_L \propto e^{-\frac{1}{\lambda_L}}. \tag{2.2}$$

Because of the formation of the Peierls gap, less of the Fermi surface is available for the formation of the BCS gap, thus depressing T_c, as described by:

$$T_c^{1-f} T_L^f = T_c, \tag{2.3}$$

where f is the fraction of the states contributing to N_{E_F} that is associated with the Peierls gap. By comparing (2.2) to (1.10), if λ_L is less than λ, superconductivity arises preferentially to the tetragonal phase and the martensitic transition is suppressed. When the characteristic parameters of an A15 compound are varied, for example by alloy additions or deviations from stoichiometry, both λ_L and λ vary. These variations are schematically represented in fig. 2-5: on cooling, when λ_L is large, the transformation takes place before the superconducting transition, thus leading to a transition from the normal tetragonal phase (NT) to the superconducting phase of the tetragonal structure (ST); conversely, the superconducting transition takes place before the tetragonal one and suppresses it, thus leaving the cubic structure unaltered (superconducting cubic phase, SC) [66].

Moreover, the tetragonal transition adversely affects the upper critical magnetic field H_{c_2}, with a difference in $H_{c_2}(0)$ between the tetragonal and the cubic phase by ∼4 T

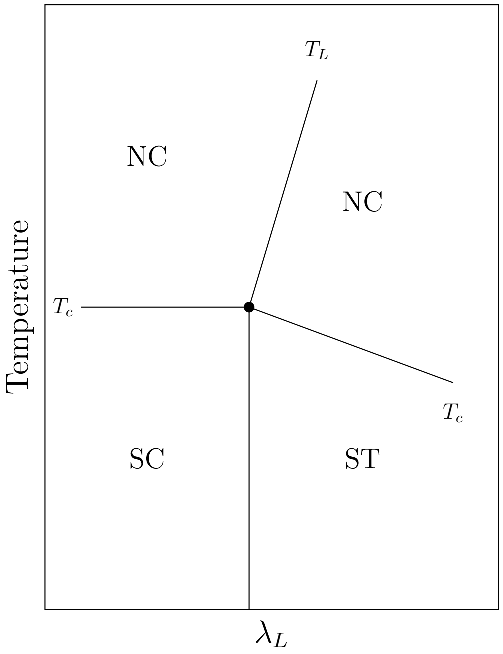

Figure 2-5: Schematic phase diagram for the superconducting and martensitic phase transitions as function of λ_L. NT, SC, ST and NC means normal tetragonal, superconducting cubic, superconducting tetragonal and normal cubic phases respectively [66].

in single crystal Nb_3Sn samples [67]. This can be best discussed in the context of the Ginzburg-Landau theory (see sec. 1.3) according to which $H_{c_2} \propto \kappa$, where κ is the Ginzburg-Landau parameter. Raising structural or compositional disorder (adding solutes or changing compositions) increases κ because of electron scattering hence improving H_{c_2}. Then, retaining the cubic phase results in an increased $H_{c_2}(0)$, while $T_c(0)$ remains unchanged. At this point, how to keep the highest T_c and have the highest H_{c_2} possible with this material is a matter of inhibiting the tetragonal transition. For this reason for technological applications, additions of Ta or Ti are applied to the pure phase to obtain the stabilization of the cubic phase [31].

The tetragonal transition takes place at the characteristic temperature T_L, but precursor effects of the transformation have been observed at temperatures well above T_L. Precursors to the tetragonal transformation, such as the existence of a large elastic softening starting from room temperature, has been shown by means of ultrasonic experiments on V_3Si [68] and Nb_3Sn [69]. In the two systems, V_3Si and Nb_3Sn, the

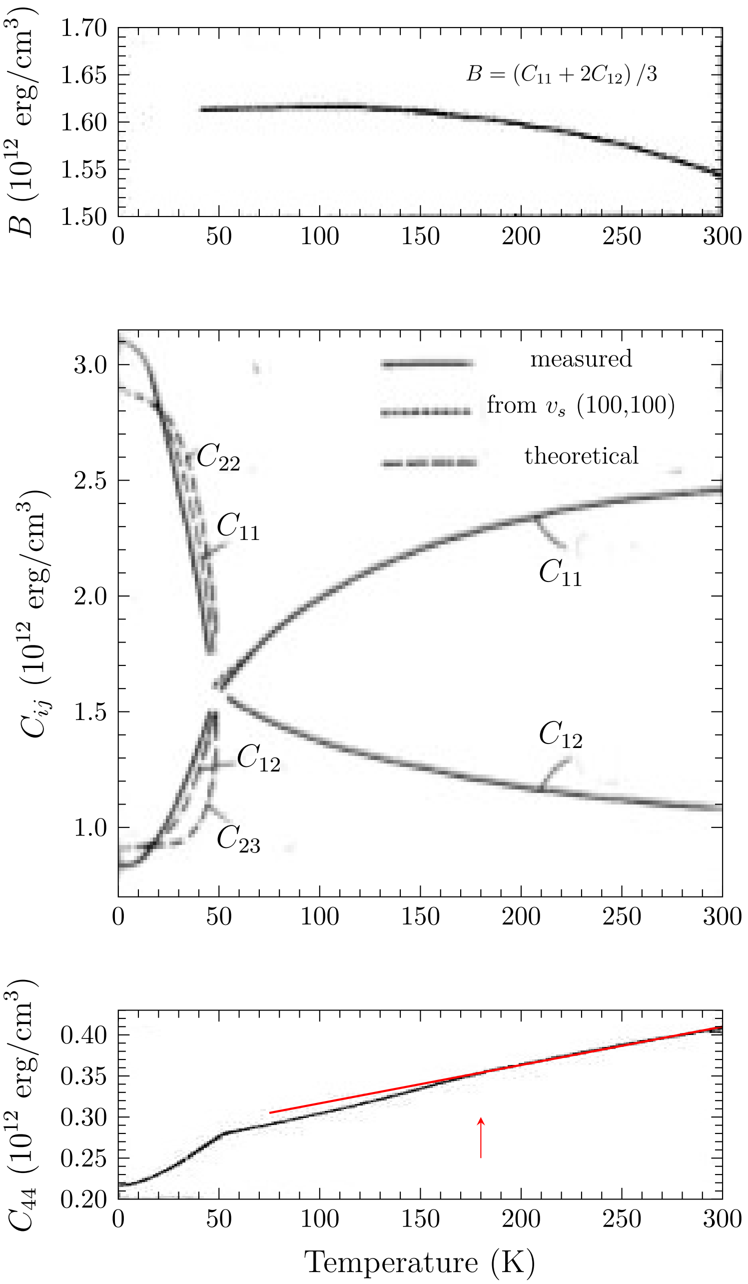

Figure 2-6: Elastic moduli versus temperature of Nb_3Sn obtained from measured sound velocities in the (100) and (110) directions [12]. The straight red line and an arrow in the c_{44} shear modulus has been sketched in order to better evidence the change of slope below 200 K.

(110) transverse acoustic (TA) and (001) longitudinal acoustic (LA) phonons were found to soften on cooling from room temperature leading to the cubic-to-tetragonal transition at T_L. This effect is reflected on the elastic properties of the material that

can be described by the elastic moduli (see appendix B).

In particular for Nb_3Sn the phonon softening implies that the shear moduli C_{44} and $C_s = \dfrac{C_{11} - C_{12}}{2}$ softens, already at room temperature, and this softening increases on cooling until the transition, which corresponds to the vanishinig of the shear modulus C_s (see fig. 2-6). As temperature is lowered from room temperature, the phonon spectrum changes. This produces the relatively large reductions of the elastic constants C_{11} and C_{44} and, as already mentioned, a value of C_s approaching zero at T_L. Interestingly, a change of slope is observed in the behaviour of the shear modulus C_{44} (see fig. B-1-right in appendix B for a schematic picture of the type of deformation to which it is related) on cooling below 200 K, as shown by the red straight line in fig. 2-6. This effect has not been commented by the authors but it could represent an indication of some change in the elastic properties of Nb_3Sn that may be further investigated. This point will be further discussed in sec. 4.2.3.

Also in the case of V_3Si the softening of the (001) LA and (110) TA mode leads to the decrease of the two shear moduli C_s and C_{44} on cooling. The larger instability occurs for the shear waves propagating along the (110) direction coupled with the shear modulus C_s. In fig. 2-7 the temperature dependence of the ratio of C_s to C_{44}, which is relatively temperature independent, is plotted. This stiffness parameter reduces on cooling between room temperature and 14 K. Around 22 K, however, the slope is reduced and some, but not complete, stabilization occurs: this partial stabilization marks the onset of the cubic to tetragonal transformation. In the superconducting state, i.e. below T_c, there is a further reduction until the growing lattice instability stops below 14 K.

Thus, these materials are characterized by a softening of the shear moduli on cooling that, sometimes, terminates in the martensitic trasformation above T_c. C_s is coupled to the Raman active mode E_g. Therefore Raman spectroscopy has been exploited to observe how this vibrational mode varies on cooling and to better understand the nature of the observed precursor effects.

With Raman spectroscopy a change of slope in the temperature dependence of the E_g mode frequency of Nb_3Sn has been observed at $T < 100$ K [70]. The E_g mode

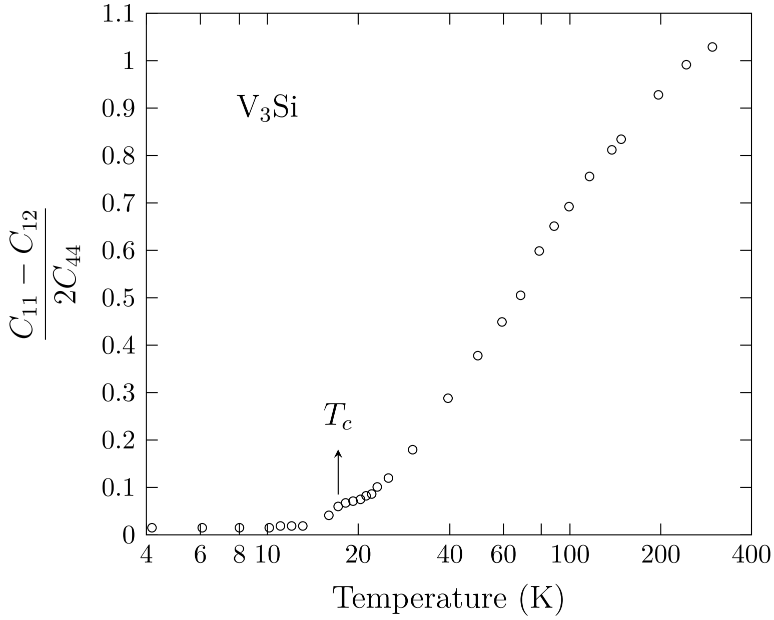

Figure 2-7: The stiffness parameter $\dfrac{C_{11}-C_{12}}{2C_{44}}$ versus temperature [68].

is related to the sublattice displacement of symmetry type Γ_{12} (see fig. 2-4) and thus to the motion of the atoms along the Nb chains. The temperature dependence of the position of the E_g peak is presented in fig. 2-8. With decreasing temperature the E_g mode frequency progressively softens on cooling, reaching a minimum at around 80 K, and then hardens on further cooling. The softening was explained by comparison to the results on the elastic constants. The softening of the E_g mode is consistent with the behaviour of the shear modulus C_s) (for which a shear wave produces a movement of Nb sublattices against each other (see fig. B-1-center in appendix B)) whose softening, already starting from room temperature, is considered as a precursor to the structural transition. Thus, in this picture, also the softening of the E_g mode can be considered a precursor to the tetragonal transition. The change of slope, with the hardening below $\sim$ 80 K, was explained with the existence of tetragonal "microdomains" forming at temperatures above the tetragonal transition. Indeed, if tetragonal domains forms, a second peak relative to the tetragonal phase arises, and it superimposes to that of the cubic phase giving it an asymmetric shape, moving the peak at higher frequencies [70]. The same effect is less pronounced in

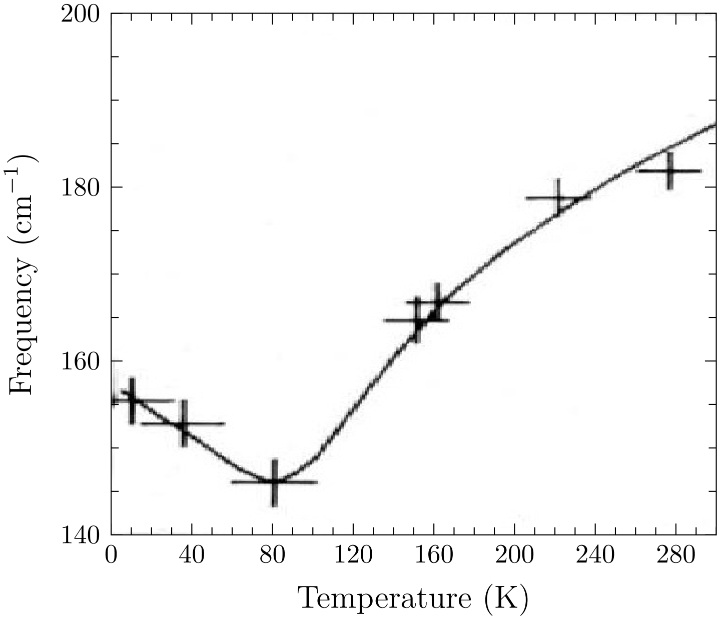

Figure 2-8: Temperature dependence of the frequency of the E_g Raman peak of Nb_3Sn [70].

non-transforming samples, where smaller portions of tetragonal domains appear to be present [70].

The Nb_3Sn properties described in this section, such as the occurrence of the martensitic transformation, the differences in the behaviour of the Raman active E_g mode between transforming and non transforming samples and the transformation temperatures T_L, that occurs between 45 K and 52 K, change from sample to sample, depending on the compositional differences and on the preparation conditions. The reason for this is in a disturbance of the periodic lattice structure. In case of disordered specimens, for example when impurities are added or out of the perfect stoichiometry (namely, for $\beta < 0.245$ [31]), one only sees the precursors of the transformation (softening of elastic moduli and E_g Raman peak), without the sample itself being transformed [70].

2.2 High pressure effects on superconductivity

Pressure (P) is a fundamental state variable: squeezing the lattice alters the atomic distances and this affects the atomic interactions by modifying the structural, vibrational and electronic properties of a material. This can be especially relevant in superconducting systems where critical parameters result from a delicate balance between structural, electronic and phonon degrees of freedom.

Among the elemental superconductors, Li, with T_c at ambient pressure of 4 mK (measured for the first time ten years ago), has a critical temperature up to 20 K at pressures above 20 GPa [71–73]. The interest in the superconductivity in dense lithium is also motivated by the fact that it is the “simplest” metal with only one valence electron and it is the superconducting element closest to hydrogen: this opens new hopes in the search for superconductivity in metallic hydrogen that has been predicted to become superconducting at high pressure with an extraordinary high T_c [74]. In this context, sulfur hydryde H_2S has been discovered to be a superconductor with a T_c of 203 K above 200 GPa [75].

The first study of pressure effects on superconductors dates back to 1925, with the work of Sizoo and Onnes [76] who took Sn and In to a hydrostatic pressure of roughly 300 bars and observed a suppression of T_c of a few mK. Since then almost all of the superconducting metallic elements have shown a decrease of T_c with pressure that has been attributed to the weakening of the electron-phonon coupling λ due to the shift of the phonon spectrum to higher frequencies [77]. However there are a few exceptions. For example, it has been observed in thallium and rhenium that a hydrostatic pressure induces a nonlinear variation of T_c with pressure [78–80]. Overall, high pressure investigations on elements have pointed out that, besides the 29 superconducting elements at ambient pressure (the highest T_c being that of Nb, that is 9.2 K), under the application of sufficiently high pressures other 24 elements become superconducting, with the maximum T_c value around 30 K for Ca (see fig. 2-9). Among these some elements are magnetic at ambient pressure some others are insulating and as pressure increases, they become metallic and then superconducting. This happens because the

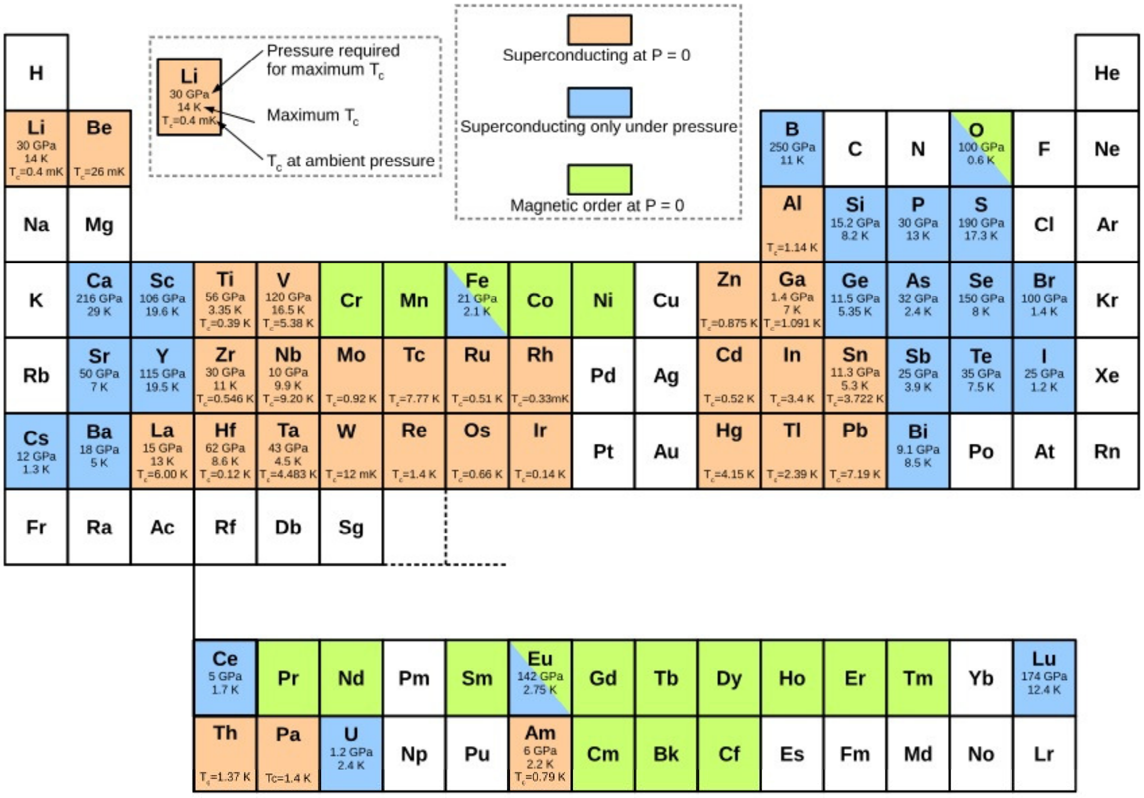

Figure 2-9: Periodic table indicating the superconducting and magnetic properties of the bulk elemental solids at ambient and high pressure, from [81].

application of a pressure, causing a reduction in the atomic distances in the lattice, broadens the electronic bands making the system more metallic.

High pressure experiments also had a great importance in the search for new superconducting compounds with higher T_c values. The T_c value of the $\mathrm{La}_{2-x}\mathrm{Ba}_x\mathrm{CuO}_4$ (LBCO) cuprate compound discovered by Bednorz and Müller in 1986 [16] was found to increase with pressure from 32 K at ambient pressure to 40 K at 13 kbar [82]. This suggested that the tuning of material parameters, for example the interatomic distances, by physical and "chemical" pressures could lead to higher transition temperatures. In fact, this idea brought to the "high-T_c revolution": simulating the effects of external pressure (variation of the lattice constants) by replacing the La atoms with the smaller isovalent Y ion (chemical pressure) led to the raising of T_c above the temperature of liquid nitrogen [17].

Summarizing, the application of high pressures has led to the discovery of many new superconductors, including 24 elemental solids, has guided the efforts to enhance the transition temperature T_c by chemical means and has yielded the dependence of T_c on structural parameters (such as the lattice parameter) which could help identifying the pairing mechanism and testing theoretical models. These results give the idea of the beneficial impact that the study of the effects of pressure on superconductors may have: high-pressure investigations together with "ab-initio material design" approach have been found extremely useful for a deeper understanding of the superconducting state.

2.2.1 The High pressure effect on A15 superconductors

To understand the pressure dependence of T_c of Nb_3Sn one has to look at the microscopic theories of phonon-mediated superconductivity, namely the BCS and the Eliashberg theory described in chapter 1. The BCS model is a rough approximation in case of strong coupling but still useful to understand the role of the main parameters involved. Eq. (1.10) allows to evaluate T_c as a function of the average phonon frequency, ω_D and of the electronic density of states, N_{E_F}. ω_D commonly increases with pressure (phonon hardening), while N_{E_F} generally decreases. Moreover, the trend of N_{E_F} can be different from case to case, depending on the shape of Fermi surfaces, that can change when raising the applied pressure. The variation of T_c with the pressure, then, results from a balance of electronic and phonon contributions: indeed, if the density of states decreases with pressure, thus lowering T_c, pressure leads to an increase in phonon stiffness, and therefore to an increase of T_c.

A15 superconductors exhibit a strong electron-phonon coupling and their superconductivity is well described by the Eliashberg theory. Within this theory the McMillan equation for the transition temperature of Eq. (1.15) shows that the pressure dependence of T_c is very complex and depends on various parameters of the electron and phonon systems. The pressure effect on μ^* (the Coulomb pseudopotential) and on $\langle I^2 \rangle$ (the squared average over the Fermi surface of the electron-phonon matrix element) are very small and then they are frequently neglected [39]. Thus the pressure

dependence of T_c reduces to two parameters, the density of states N_{E_F} and the average phonon energy $\langle\omega\rangle$, like the BCS theory.
However, it is possible to capture more information from the strong coupling T_c (Eq. (1.15)) by taking its logarithmic volume derivative. The following relation is obtained:

$$\frac{d\ln T_c}{d\ln V} = -\frac{Bd\ln T_c}{dP} = -\gamma + f\left(\lambda, \mu^*\right)\left[\frac{d\ln\eta}{d\ln V} + 2\gamma\right], \tag{2.4}$$

where B is the bulk modulus, $\gamma = \dfrac{d\ln < \omega_{log} >}{d\ln V}$, $\eta = N_{E_F} < I^2 >$ is the Hopfield parameter, and $f\left(\lambda, \mu^*\right) = 1.04\lambda\left[1 + 0.38\mu^*\right]\left[\lambda - \mu^*\left(1 + 0.62\lambda\right)\right]^{-2}$. The first term on the right, which comes from the prefactor to the exponent in the expression for T_c (Eq. (1.15)), is usually very small as compared to the second term. The sign of the pressure derivative $\dfrac{dT_c}{dP}$, therefore, is determined by the relative magnitude of the two terms in the square brackets. The first "electronic" term involves the derivative of the Hopfield parameter. McMillan [39] pointed out that whereas individually N_{E_F} and $< I^2 >$ may fluctuate appreciably, their product remains nearly constant and the coupling constant λ is governed mainly by the phonon factor $M < \omega^2 >$. However, on elastically soft materials, such as Nb_3Sn, η reflects the behaviour of N_{E_F}. An examination of high-pressure data on metal superconductors reveals that Eq. (2.4) is obeyed if η increases under pressure at the approximate rate $\dfrac{d\ln\eta}{d\ln V} \approx 1$. The expression in the curly brackets is positive since the lattice term is positive ($2\gamma \approx +3$ to $+5$) and dominates over the negative electronic term $\dfrac{d\ln\eta}{d\ln V} \approx 1$. Since Δ is always positive and the first term is relatively small, the sign of $\dfrac{dT_c}{dP}$ must be negative. This accounts for the almost universal decrease of T_c with pressure in simple metals due to lattice stiffening.

In general, it is known that an applied stress affects the superconducting properties of Nb_3Sn in a detrimental way [83]. Relevant for applications is the degradation of the critical current density and of the critical temperature T_c due to an applied axial stress on technological wires (of different manufacture) ([84] and references therein).

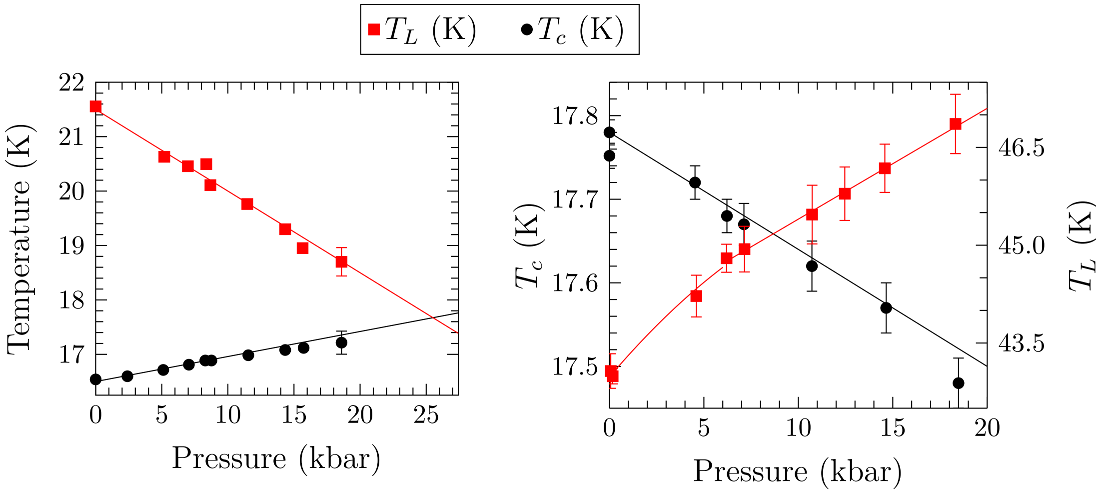

Figure 2-10: The pressure dependence of T_L and T_c in (left) V_3Si and (right) Nb_3Sn.

If, on the one hand, the effects of a non hydrostatic applied stress have been widely explored, on the other hand a detailed characterization of Nb_3Sn P-V structural phase diagram is still lacking. Below, the known results about the behaviour of the tetragonal and superconducting transitions in presence of an applied hydrostatic pressure are discussed.

In 1971, Smith [85] determined and reviewed the superconducting transition temperatures of different A15 compunds up to 25 kbar. A $T_c\,(25\text{ kbar}) = 17.83$ K has been measured on Nb_3Sn with a linear variation with pressure at a rate $\dfrac{\partial T_c}{\partial P}$ of $-\ 1.4\ \times\ 10^{-5}$ K bar^{-1}. For all the samples no irreversibilities have been found, i.e. the trend of T_c was the same when increasing or decreasing the applied pressure. Further experiments by Chu and Vieland were consistent with this previous result [86]. In particular Chu [87] also reported T_L and T_c as a function of pressure, plotted in fig. 2-10. An enhancement of the lattice transformation temperature T_L is clear, at a rate of $+(2.8\pm0.1)\ \times\ 10^{-4}$ K bar^{-1} (fig. 2-10-right). The increase of T_L when the applied hydrostatic pressure increases is not a general feature of A15 materials, indeed, for example for V_3Si the suppression at a rate of - $(1.5\pm0.1)\times\ 10^{-4}$ K bar^{-1} has been observed (fig. 2-10-left).

The effects of a hydrostatic pressure on the Batterman-Barrett transformation and on the superconducting transition were theoretically described within the Labbé-Friedel

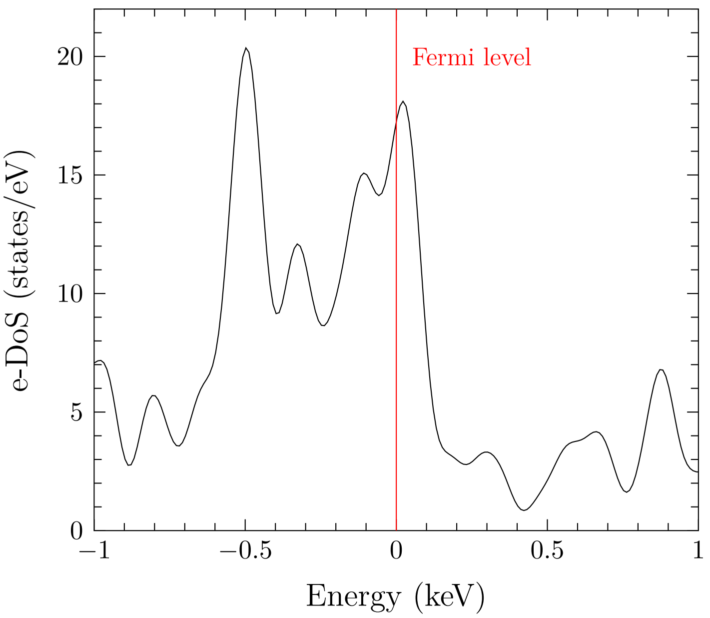

Figure 2-11: Electronic density of states of Nb_3Sn from ab-initio calculations.

linear chain model (see sec. 2.1.2). In this model T_L and T_c are functions of the number of the d-electrons entering N_{E_F}, Q. An applied pressure redistributes the charges between different bands and then changes Q (by transferring electrons from s to d bands) and the position of the Fermi level. At ambient pressure E_F is near to a peak of the density of states (see fig. 2-11) and the application of a pressure can result in an enhancement or suppression of T_L if E_F is moved either towards such peak or away from it, respectively.

Recently, new room temperature experiments at high pressure on A15 compounds have revived the interest on the pressure effect in this materials. In particular, high pressure diffraction experiments on Nb_3Ga and Nb_3Al in the GPa range, pointed out a compressibility anomaly in the P-V plot at around 16 GPa and 18 GPa, respectively [7, 8] (see fig. 2-12). These anomalies do not involve structural transitions, for example the Batterman-Barrett. Rajagopalan [9] suggested by means of ab-initio calculations that this anomaly is to be related to an electronic topological transition . He calculated the electronic structure at different pressures by means of the all electron full potential linear augmented plane wave method demonstrating that around

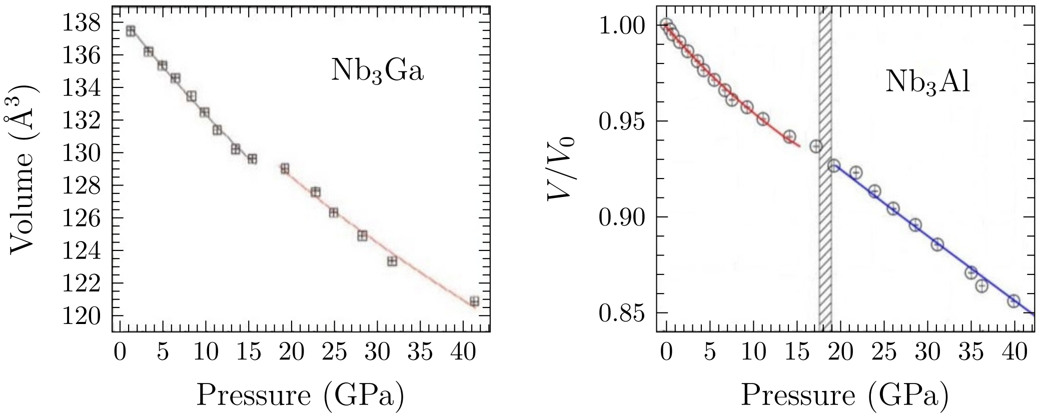

Figure 2-12: The P-V plot of (left) Nb$_3$Ga [8] and (right) Nb$_3$Al [7].

the Fermi level the bands are flat at the zone center and they are "d" like bands of Nb atoms. A "d" like band of Nb at the zone center is below the Fermi level at 12 GPa, then moves above and touches the Fermi level at about 17 GPa and under further compression the band moves down below the Fermi level around 22 GPa. The movement of this particular band causes a marked change in the Fermi surface topology. If the variation of an external parameter like pressure causes changes in the Fermi surface topology, it is likely to influence the otherwise monotonic variation of density of states. This is pointed out by Lifshitz [88] who has demonstrated large change in the density of states and consequently a change in the associated thermodynamic properties if a closed Fermi surface transforms into a an open surface.

The past year Ren *et al.* [11] reported their studies of T_c as a function of pressure of single-crystal and polycrystalline Nb$_3$Sn up to ∼10 GPa. In the whole pressure range investigated, they obtained that the normal state resistivity near the superconducting transition is described by the relation $\rho(T) = \rho_0 + AT^2$, where ρ_0 is the residual resistivity and A is a prefactor proportional to N_{E_F}. This relation has been demonstrated by Rice [89] and shows that electron-electron scattering contributes a characteristic T^2 term to the resistivity. However, above a certain temperature (∼25-35 K) $\rho(T)$ exhibits a downward deviation below 4 GPa from the T^2 dependence, fingerprint of the structural transition, and an upward deviation at higher pressure that suggests the presence of additional contributions from the structural transition and the conventional electron-phonon scattering to the resistivity. From the measurements of the

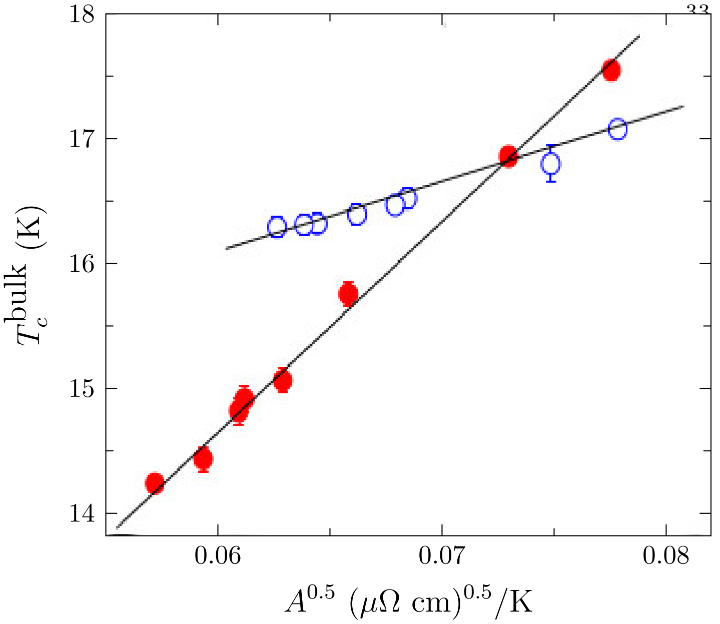

Figure 2-13: T_c plotted as a function of A for Nb_3Sn (S=single cristal) and (P=policrystalline sample) under pressure. The solid lines are guide to the eyes. [11]

resistivity as function of both temperature and pressure, they obtained a reduction of T_c with pressure, at a rate in agreement with the previously reported values, that is well described by a linear function of $\sqrt{A}$ (see fig. 2-13). These results highlight the importance of the electronic states at the Fermi level in determining T_c in Nb_3Sn under pressure as suggested in the Labbé-Friedel model.

Given the interesting results of the last years, obtained thanks to the availability of increasingly sophisticated high pressure systems with which very high pressure values can be achieved, this work is in part devoted to the study of the effect of an applied pressure on the structural and superconducting properties of Nb_3Sn. In the following chapters the results of the new diffraction experiments on Nb_3Sn conducted during this thesis work will be presented and discussed in comparison to the results reviewed in this chapter. In particular, the presence of features not previously known in the pressure range from 0 to 10 GPa and in the temperature range from room temperature to that of liquid nitrogen will be highlighted.

Before discussing these works, the samples under consideration will be described in the next chapter.

Chapter 3

The Nb_3Sn samples

In this chapter the Nb_3Sn samples that have been studied during this thesis work will be described. The studied samples are of two types: filaments taken from a wire of Nb_3Sn and pure Nb_3Sn polycrystalline samples.

3.1 Nb_3Sn wire

The Nb_3Sn filaments have been taken from an internal-tin wire that has been supplied by Outokumpu Copper Superconductors Italy (OCSI, now Luvata) [90]. The wire was a prototype product for ITER, the International Thermonuclear Experimental Reactor.

The wires used in this thesis work are internal tin wire.

The internal tin process starts with elemental niobium filaments and a tin core (with tantalum as ternary addition used to facilitate wire drawing and to increase H_{c_2}) in a copper matrix surrounded by a tantalum-niobium diffusion barrier, forming "bundles". A number of bundles distributed in concentric rings in a pure copper matrix makes up the wire. When the necessary shape and size have been achieved by means of extrusion processes, the wires undergo a multi-stage heat treatment, in which tin diffuses through copper, forming Cu-Sn alloys, which then react with Nb to form the Nb_3Sn phase. The described process is complex, but now well established and allows the production of excellent quality wires in terms of critical temperature and upper

critical magnetic field.
The wires, here, were designed with a diameter of 0.81 mm, a Cu/nonCu ratio of about 1, a filament diameter around 5 μm, and a distributed Ta-Nb diffusion barrier that prevents the reaction between the Cu matrix and Sn during the high temperature processing (see the SEM cross sections of the strand and one of its sub-elements in fig. 3-1). The Energy Dispersive X-ray (EDX) analysis of fig. 3-2 shows the distribution of the different elements within the strand cross-section: in each image the white regions correspond to one of the element (Nb, Sn, Ta, Cu). The Heat Treatments (HT), necessary to react Nb with Sn to obtain the A15-Nb_3Sn phase, have been performed at ENEA[1], following the HT recommended by the supplier. The thermal stabilizing Cu matrix has been etched away chemically to extract the filaments.

Nb_3Sn wires have been the first samples available to us for measurements. Then the first experiment of this thesis work, namely the XRD measurements at high pressure and room temperature (see sec. 4.2.2), has been made on wires. A good knowledge of the wires is important for understanding their behaviour under operating conditions, and the first experiment of this thesis was addressed to this aim. However, for a good representative characterization of pure Nb_3Sn, non-technological samples are much more suited, in particular if a structural characterization of the material is desired. Indeed, wires, can exhibit different behaviors because of impurities. For example here the tantalum inclusions (with a content of Ta $\geqslant$ 2.8 at. %) in the strands lead to the disorder necessary to avoid the tetragonal transition, allowing higher values of H_{c_2} with respect to the pure material. Therefore, the study of the properties of the material devoted to a better understanding of its structural characteristics in different conditions needs the use of pure samples. Thus, for these reasons, pure Nb_3Sn polycrystalline samples described in the section below have been studied in all the other experiments.

---

[1] Italian National Agency for New Technologies, Energy and Sustainable Economic Development-Italy

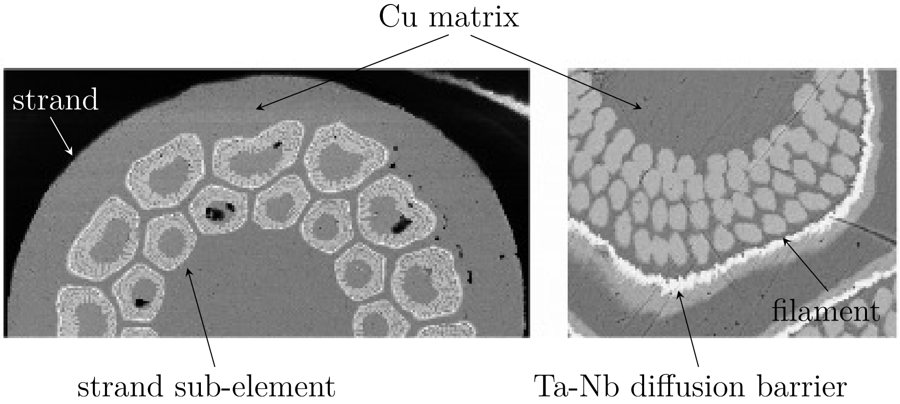

Figure 3-1: SEM cross section of the OCSI internal-tin strand (outer diameter 0.81 mm), after heat treatment (left). One of the strand sub-elements(right). [90].

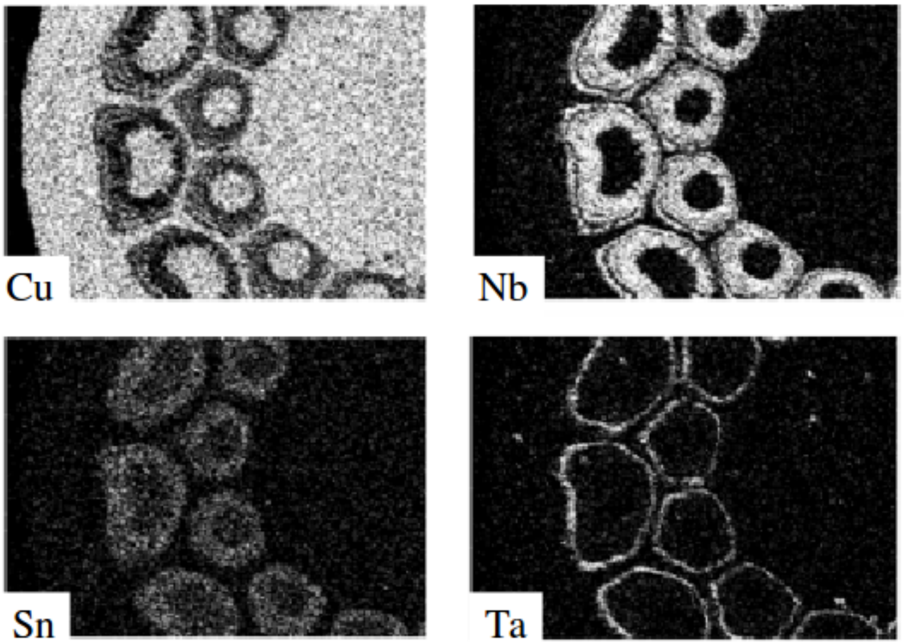

Figure 3-2: EDX analysis of the OCSI strand, after the heat treatment. The white area represents the spatial distribution of each element. Upper left: Cu; upper right: Nb; lower left: Sn; lower right:Ta [90].

3.2 Nb_3Sn polycrystalline samples

The Nb_3Sn polycrystalline samples [91] studied in this thesis have been provided by dr. Tiziana Spina and prof. René Flükiger of CERN and University of Geneva, respectively. These samples has been produced at the facility of the Applied Physics Dept. of the University of Geneva.

The samples were obtained starting from a mixture of Nb powder (99.9 % purity, desoxydized, 25÷45 μm particle size) and Sn powder (99.5 % purity, 40 μm particle size), with a ratio of Nb : Sn = 3 : 1. The masses of Nb and Sn powders have been chosen to get a Sn composition of 24.8 at. % Sn, i.e. slightly below the stoichiometric composition of 25 at. % Sn. This choice was motivated by the necessity to get single phase samples: indeed at 1250 °C, that is the temperature at which Nb and Sn reacted, the Nb rich limit of the two-phase region A15+Nb_6Sn_5 starts very close to 25 at. % Sn, and even a small composition gradient would cause the presence of a second phase (see the Nb_3Sn phase diagram in fig. 2-2) [91].

As a first step, the powders are mixed for almost 1 hour in a mixing machine, enclosed in a Nb jacket and loaded into a stainless steel billet. Then they were reacted in a HIP (Hot Isostatic Pressure) furnace at 1250 °C for 24 h (with a cooling rate of 3 °C/h) under 2 kbar Ar pressure. As shown by the phase diagram of Nb_3Sn (fig. 2-2), the choice of the sintering temperature allows to get Sn contents at compositions very close to stoichiometry.

After the HIP process, the steel jacket was mechanically removed from the Nb_3Sn block. Then sample platelets were cut by means of spark erosion and then were polished. The polishing procedure was performed with silicon carbide grinding papers to remove the cutting part containing mainly carbon and oxygen impurities arising from the spark erosion dielectric oil. The Nb_3Sn platelets obtained are then submitted to a final Flash-Anneal of 20 minutes at 900 °C under a pressure of 10^{-7} mbar for releasing the surface stresses induced by the polishing procedure.

Preliminary analysis on Nb_3Sn samples to define their initial characteristics (homogeneity and composition) have been performed at the University of Geneva by means of SEM, laboratory X-ray diffraction and magnetization measurements.

The samples are found to contain a small amount of oxygen and carbon coming from the synthesis procedure. By means of Hot Extraction [91] the total amount of oxygen was determined to 0.14 wt. % (approximately 1 at. %) and the total amount of carbon to 0.01 wt. %.

SEM analysis on a broken piece, obtained from the Nb_3Sn bulk samples, reveals that the maximum grain size is 20 μm (see fig.3-3).

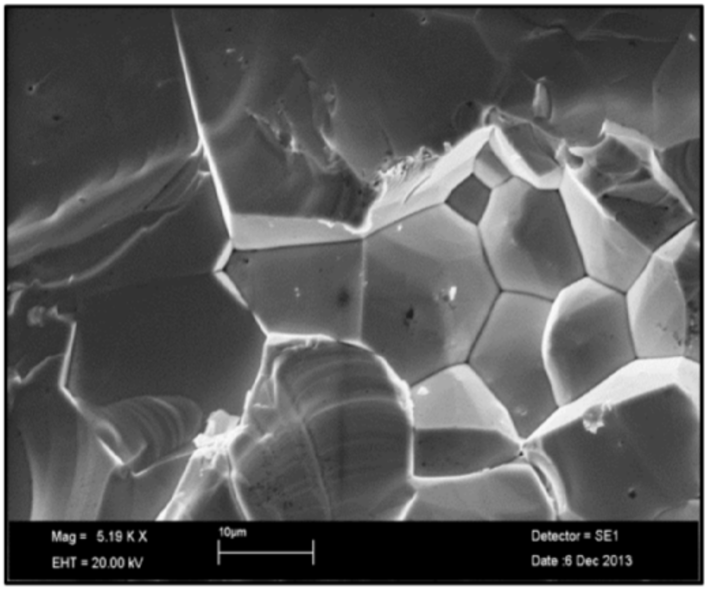

Figure 3-3: SEM of Nb_3Sn policrystalline samples.

By means of X-ray diffraction, the lattice constant was found to be $a = 5.291 \pm 0.003$ Å. The critical temperature of the Nb_3Sn platelets was measured with a SQUID magnetometer in zero field and was found to be 17.9 K.
The values obtained for the lattice parameter and the critical temperature are in good agreement with the reported values for an almost stoichiometric composition as can be seen in fig. 3-4.

In the next section further characterization of these laboratory polycrystalline samples by means of microwave measurements will be presented.

3.3 Microwave measurements

This section is devoted to the electrical characterization of the polycrystalline samples by means of the microwave technique performed at the University Roma Tre. This technique can be applied only on samples of thin film shape, such as the Nb_3Sn platelets described in sec. 3.2

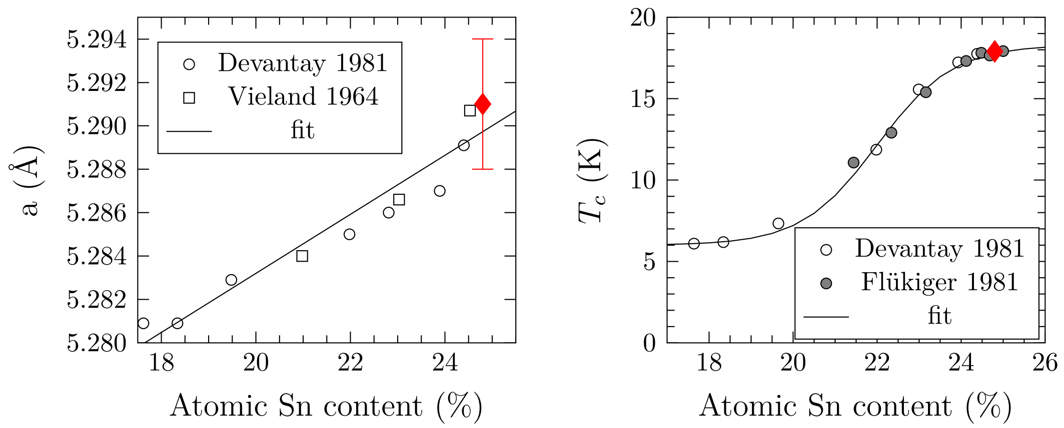

Figure 3-4: Literature results of the lattice parameter a and the critical temperature T_c as a function of the atomic Sn content (adapted from [31]). The red points are the value of a and T_c of the laboratory polycrystalline Nb_3Sn samples studied in this thesis.

The behaviours of the surface resistance as a function of temperature and of an applied magnetic field have been studied in order to obtain the critical temperature T_c and the upper critical magnetic field H_{c_2}.

The basic device for this characterization is a dielectric-loaded resonator, where a dielectric is placed in a metallic cavity within which it is possible to confine electromagnetic fields. Under ideal conditions, that is, in the absence of dissipations, oscillations of the electromagnetic field will remain indefinitely in the resonator for particular field configurations.

In real resonators energy losses for internal dissipation and external losses must be taken into account.

The quality factor, Q_U, of a resonator expresses the ratio of the stored energy W in the resonator volume to the energy dissipated in a unit time, P, at the resonance frequency ν_0 [92]:

$$Q_U = \frac{2\pi\nu_0 W}{P} \tag{3.1}$$

This is the so-called *unloaded* quality factor: it is calculated by considering only the intrinsic resonator losses, and not any other losses due to the coupling of the system with external devices.

In presence of the diectric Q_U can be re-expressed as:

$$\frac{1}{Q_U} = \frac{1}{Q_\Omega} + \frac{1}{Q_d}$$

where Q_Ω is the ohmic quality factor and Q_d is the dielectric one.

Excitation and detection of the signal is obtained by loops or antennas, which introduce additional losses. Thus, the whole assembly efficiency is characterized by the *loaded* quality factor Q_L:

$$Q_L = \frac{2\pi\nu_0 W}{P + P_e},$$

where P_e accounts for the energy losses due to the coupling of the resonator to external devices for the excitation of the system or the detection of the response signal. In general it is preferable to work with a system where $Q_L \simeq Q_U$, so that it can be assumed that the answer from the resonator is exclusively dependent on its intrinsic properties.

The resonator used for this thesis is constituted by a cylindrical structure with metallic walls enclosing a coaxial dielectric cylinder of complex relative dielectric constant $\varepsilon_r = \varepsilon_r'(1+i\tan\delta_\varepsilon)$, where $\tan\delta_\varepsilon$ is the loss tangent, as in the so-called Hakki-Coleman geometry [93] (see fig. 3-5-up). The resonator operates in the transverse electric TE011 mode, with circular, planar currents induced on the conducting bases (see fig. 3-5-down-left) and the resonance frequency is $\nu_0 \sim 15$ GHz. The presence of the high permittivity dielectric causes the electromagnetic field to be mostly contained in the dielectric and its immediate vicinity so that the losses due to the interaction between the electromagnetic field and the metal walls of the resonator can be ignored (see fig. 3-5-down-right). The resonator is placed inside a cryostat and is connected to a vector network analyzer, VNA (Anritsu), via coaxial cables: the transmission line, part inside the cryostat, is made up of cryogenic coaxial cables, in order to reduce thermal disturbances. The coaxial cables terminate in the resonator with coupling loops. A temperature sensor is placed in the metallic walls of the resonator in order to measure the temperature of the sample, and two heaters are arranged so as to uniformly heat the resonator.

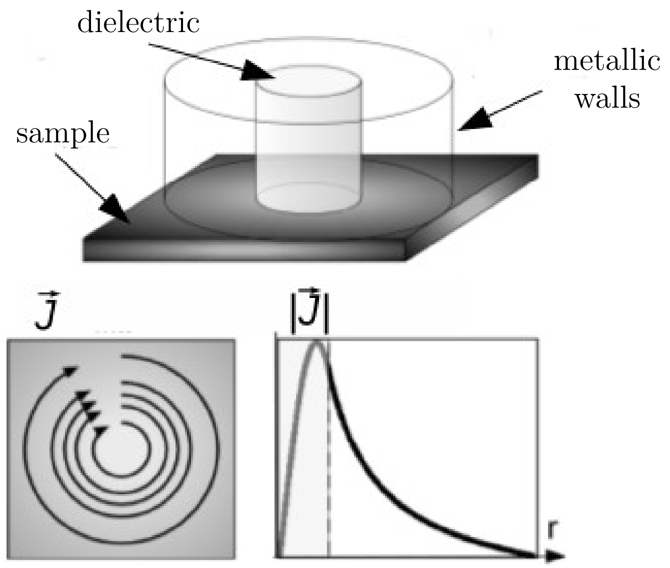

Figure 3-5: Sketch of a typical dielectric resonator. The circular geometry of the current on the sample is shown.

The quantity that is directly measured is the transmission coefficient, $S_{21}(\nu)$, that is expressed as:

$$S_{21}(\nu) = \frac{S_{21}(\nu_0)}{1 + 2iQ_L\frac{\nu-\nu_0}{\nu_0}}. \tag{3.2}$$

The coefficient $|S_{21}(\nu)|^2$ describes a lorentzian curve as a function of ν. By fitting $|S_{21}(\nu)|^2$ the quality factor Q can be obtained.

The physical quantity which is experimentally accessible with this method is the surface impedance, defined as:

$$Z_s = \frac{E_\parallel}{H_\parallel} = R_s + iX_s = \sqrt{\frac{i\omega\mu_0}{\sigma}} \tag{3.3}$$

where $E_\parallel$ and $H_\parallel$ are the fields components at the surface of the (super)conductor [92] and ρ is the complex conducibility of the (super)conductor. The real part of the surface impedance, R_s, is the quantity of interest for the desired characterization of the samples and can be obtained from the quality factor Q by means of the relation:

$$\frac{1}{Q_U} = \frac{R_s}{G_s} + \frac{R_m}{G_m} + \eta \tan\delta_\varepsilon \tag{3.4}$$

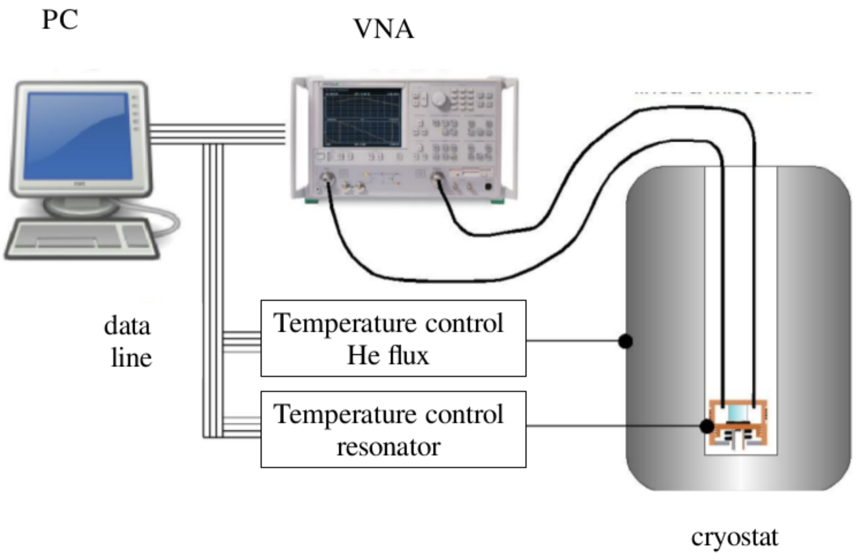

Figure 3-6: Experimental setup.

where G_s and G_m are the geometric factors of the surface covered by the superconductor and the metallic walls, respectively, R_m is the surface resistance of the metallic walls and η is another geometrical factor that accounts for the energy stored in the dielectric with respect to the total energy in the resonator [92]. In order to obtain the surface resistance of the superconductor, R_s, it is sufficient to know the measured quality factor, the geometric factors, which can be obtained by numerical simulations of the electromagnetic structure of the resonator, and R_m that can be determined with an appropriate calibration.

Measurements have been made at temperature down to 6 K and magnetic field up to 12 T.

Figure 3-7 shows the surface resistance R_s of a Nb_3Sn platelet in absence of a magnetic field. The critical temperature T_c, evaluated at the onset of the transition, is of 17.9 K, in agreement with that reported by the supplier of the samples [91]. In fig. 3-8 the obtained surface resistance R_s as a function of the temperature is plotted at different values of an applied magnetic field.

In fig. 3-9 the surface resistance at 15 K as function of the applied field is shown. It is clear how the sample reaches the normal state for field values of $\sim$ 6 T, thus being

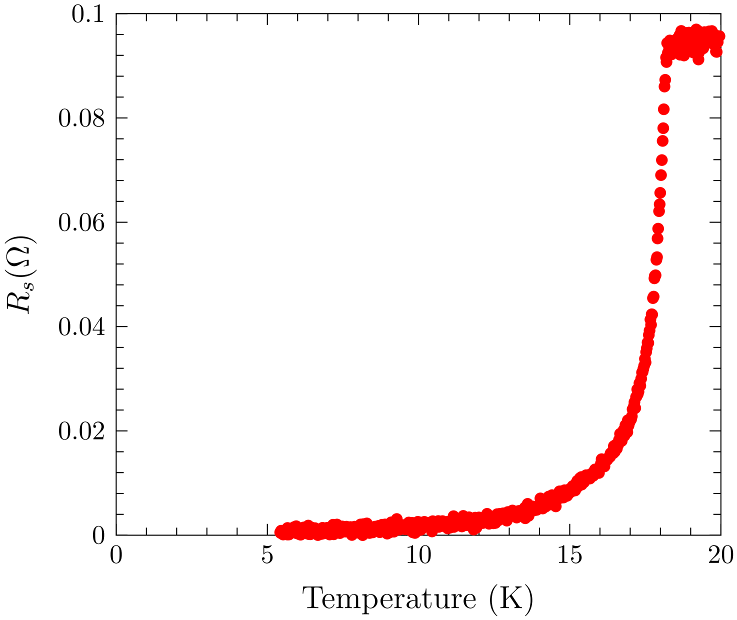

Figure 3-7: The surface resistance R_s of a Nb_3Sn platelet at 0 T.

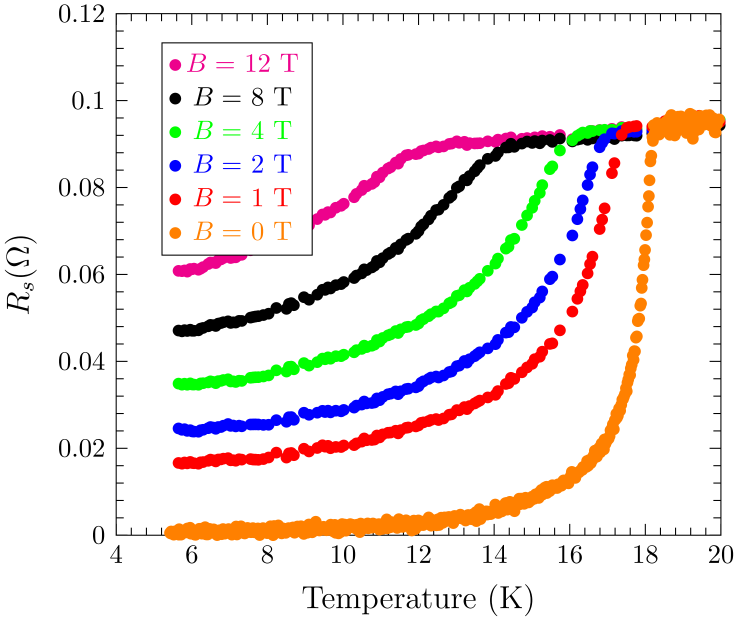

Figure 3-8: The surface resistance, $R_s(T, B)$, as function of temperature at different values of an applied magnetic field on the polycrystalline Nb_3Sn sample.

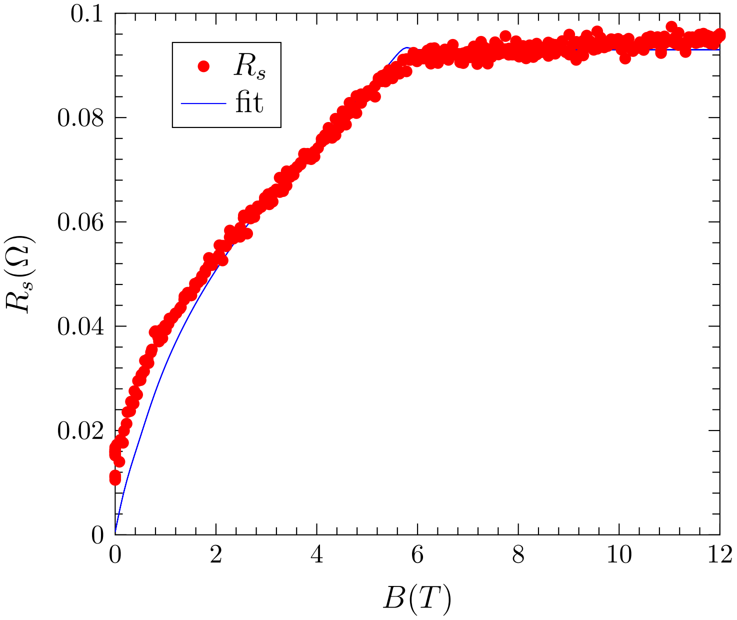

Figure 3-9: The surface resistance R_s at 15 K as function of the applied magnetic field B on the polycrystalline Nb_3Sn sample.

this value the upper critical magnetic field at 15 K.

In fig. 3-10, the fit of the $\mu_0 H_{c_2}$ values obtained from data of figs. 3-8 and 3-9 is reported. $\mu_0 H_{c_2}$ at 0 K is expected to be > 20 T, but the cryomagnet used for these experiments cannot reach this field values. In spite of this, from the data of fig. 3-10, its value can be obtained by fitting these data to the empirical relation $H_{c_2}(T) = H_{c_2}(0)\left[1-(T/T_c)^2\right]$ [37]. The value of 21 T for $H_{c_2}(0\mathrm{K})$ is obtained. This value is compared to those reported in literature in fig. 3-11, where, if we assume that this sample undergoes the tetragonal transition, because its composition is in the range where it happens, this result is in fair agreement with those reported in literature.

In the following chapter the high pressure and low temperature X-ray diffraction experiments on the Nb_3Sn samples here described are discussed in comparison to the known results.

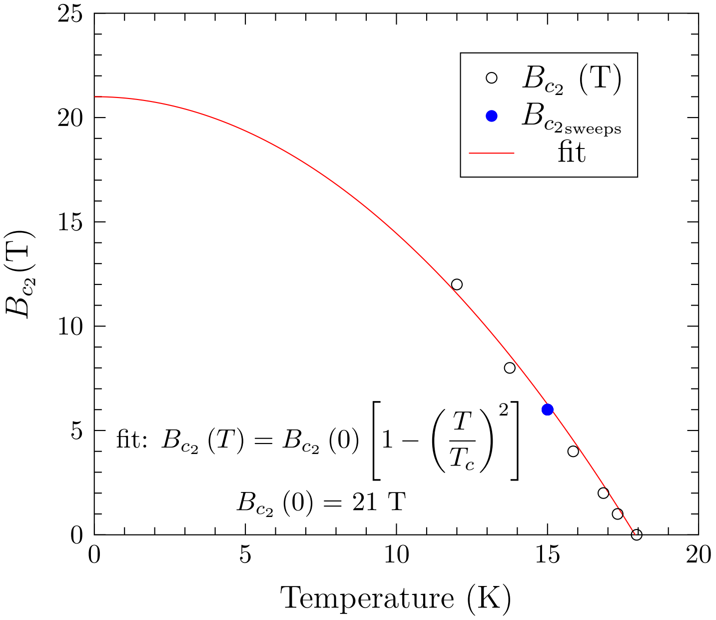

Figure 3-10: Temperature dependence of the critical field of the polycrystalline Nb_3Sn sample.

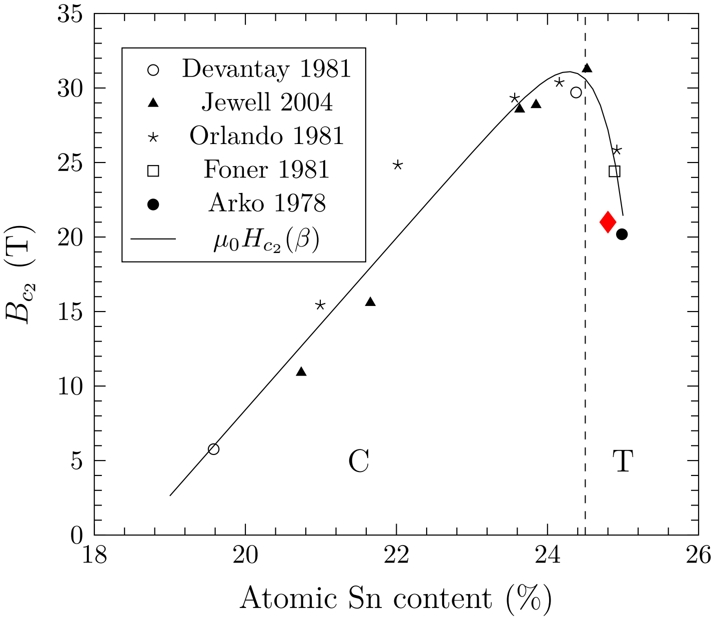

Figure 3-11: Literature results of the upper critical magnetic field as a function of the atomic Sn content (adapted from [31]). The dashed line separates the region in which the phase is cubic (C) from that in which it is tetragonal (T). The red point is the value of B_{c_2} of the polycrystalline Nb_3Sn samples studied in this thesis.

Chapter 4

X-ray diffraction characterization

X-ray diffraction (XRD) is a non-destructive technique for quantitative and qualitative analysis of crystalline materials, allowing the determination of crystal structure of solids.

The first X-ray [1] diffraction experiment dates back to 1912 and was performed by Friedrich, Knipping and Max von Laue on single crystals of copper sulfate and zinc sulfite. Four years later (1916), Debye and Scherrer published the first powder diffraction experiments [94].

Today XRD is one of the most powerful techniques to probe atomic structure of matter down to the atomic scale resolution. The advent of sychrotron radiation X-ray sources, characterized by high brilliance and continuum spectrum extending from soft to very hard X-ray ($0.1 < \lambda < 1$ Å), brought the X-ray diffraction based techniques to an accuracy without precedent. Furthermore the new generation X-ray diffraction beamlines offer the unique possibility to explore the matter under extreme conditions, such as extremely high pressures (above 10^2 GPa) and temperatures (up to 5000 K) [95,96], high magnetic fields (up to 25 T) and also low temperature down to that of the liquid helium [97].

In this work the attention is concentrated in the high pressure and low temperature regions.

Understanding the evolution of the crystal structure when subjected to an applied

---

[1] X-rays have been discovered in 1895 by the German physicist Wilhelm Röntgen

pressure is of particular importance and represents an excellent test for the theoretical models based on first-principles calculations (e. g. density functional theory based models).

This chapter summarizes the information that can be obtained from the analysis of a powder diffraction pattern exploiting, in particular, the method of the Rietveld analysis. Later, the experimental setup, the data reduction and analysis procedures will be briefly described. Finally, the analysis of the diffraction patterns as a function of an applied hydrostatic pressure (up to ∼50 GPa) and of temperature (from room temperature to ∼80 K) will be discussed and the results will be compared to the literature data.

4.1 Notes on X-Ray Powder Diffraction and Rietveld Refinement

Diffraction is the result of the interference among X-ray waves scattered by atoms arranged on a periodic crystalline lattice.
The first successful and simplest explanation of diffraction from solids is given by Bragg's law [2]. This describes the X-ray diffraction in terms of a reflection of X-rays by set of lattice planes by establishing a relationship among diffraction angle, wavelength of the incoming radiation and interplanar spacing. It is expressed by the famous formula:

$$2d_{hkl}\sin\theta_{hkl} = n\lambda, \tag{4.1}$$

where hkl are the Miller indices, d_{hkl} is the interplanar distance between hkl planes, θ_{hkl} is the angle between the propagation vector of the incoming wave and the normal to the hkl planes, n is the order of reflection and λ the wavelength of the incoming radiation. Knowing the wavelength of the incoming radiation and measuring θ_{hkl} it

---

[2] William Henry Bragg and his son William Lawrence Bragg founded X-ray diffraction science in 1913-1914 were awarded the Nobel Prize in Physics in 1915 "for their services in the analysis of crystal structure by means of X-rays."

is possible to calculate the interplanar distance that is directly related to the lattice parameters of the crystal.

The intensity of a diffraction peak in a powder diffraction pattern is expressed by the formula:

$$I_{hkl} = K \times M_{hkl} \times LP\left(\theta\right) \times T_{hkl} \times \left|F_{hkl}\right|^2 \times I_{th}, \tag{4.2}$$

where:

- K is a scale factor required to normalize experimentally observed integrated intensities with absolute calculated intensities;
- M_{hkl} is the multiplicity factor and it accounts for the presence of multiple symmetrically equivalent reflections;
- $LP\left(\theta\right)$ is the Lorentz-polarization factor that depends on the polarization of the incoming beam and the geometry of the experimental setup;
- T_{hkl} accounts for possible deviations from a complete randomness in the distribution of grain orientations;
- $\left|F_{hkl}\right|^2$ is the structure factor, that depends on the details of the crystal structure of the material: coordinates and types of atoms and their distribution among different lattice sites.
- I_{th} accounts for the atomic thermal displacement and depends on the so-called Debye-Waller factor $B = 8\pi\langle u_i^2\rangle$ where $\langle u_i^2\rangle$ are the mean square displacements of the ith-atom from its equilibrium position, $\mathbf{d}_i$.

Although, the powder method was developed as early as 1916 by Debye and Scherrer, for more than 50 years its use was often limited to qualitative and semi-quantitative phase analysis and macroscopic stress measurements. The major breakthrough in the value of the powder method as a quantitative tool was the development of the Rietveld method.

The Rietveld method (also known as the full pattern or the full profile refinement) is now the most commonly employed structure refinement procedure of powder diffraction data. It has been devised by the Dutch crystallographer Hugo Rietveld in 1966 [98] for the structure determination from a neutron powder-diffraction diagram and has been extended to X-ray powder diffraction data in 1977 with the work of Young, Mackie and Von Dreele [99].

This method is a technique for crystal structure refinement which uses the entire powder pattern instead of analyzing individual Bragg reflections separately. This approach minimizes the impact of overlapped and degenerate peaks by calculating the entire powder pattern of a crystalline model by means of Eq. (4.2), including various experimental and sample dependent peak-broadening effects. Parameters in the model such as atomic positions, lattice parameters, and experimental factors that affect peak-shape and background are varied, using a least-squares approach, until the agreement between the calculated and measured diffraction profiles are optimized.

This is a refinement method: once the crystal structure has been chosen the Rietveld procedure refines the positions of the atoms and the lattice parameters keeping the structure unchanged.

Rietveld refinement employs the nonlinear least squares method where the function which has to be minimized by least squares is the residual M:

$$M = \sum_{i=1}^{n} \mathrm{w}_i \left(Y_i^{obs} - Y_i^{calc} \right)^2 , \tag{4.3}$$

where w_i is the weight assigned to the ith data point and the sum is over all data points.

The quality of the refinement using the Rietveld method is indicated by some figures of merit. These are:

- the *profile residual factor*, R_p:

$$R_p = \frac{\sum_{i=1}^{n} \left| Y_i^{obs} - Y_i^{calc} \right|}{\sum_{i=1}^{n} Y_i^{obs}}; \tag{4.4}$$

- the *weighted profile residual factor*, R_{wp}:

$$R_{wp} = \sqrt{\frac{M}{\sum_{i=1}^{n} w_i \left(Y_i^{obs}\right)^2}}; \tag{4.5}$$

- the *reduced* χ^2 or *goodness of fit*:

$$\chi^2 = \frac{M}{N_{obs} - N_{var}}, \tag{4.6}$$

  where N_{obs} is the number of point in the histogram and N_{var} is the number of free least square parameters;

- the *expected weighted profile residual*, $R_{wp(exp)}$:

$$R_{wp(exp)} = \frac{R_{wp}}{\sqrt{\chi^2}}. \tag{4.7}$$

A simple analysis of the figures of merit listed above indicates that a better fit results in lower values of all residuals.

4.2 XRD experiments on Nb$_3$Sn

In this section the XRD measurements on the samples described in chap. 3 are discussed. Two experiments have been made: one, at high pressure and room temperature and another in the temperature range 77-300 K and ambient pressure.

4.2.1 Data reduction

The powder diffraction pattern have been collected by means of area detectors, for which the patterns consist of a set of concentric rings (see fig. 4-1-left).
One of the advantage of using such a type of detector is that they accumulate the whole diffraction patterns in reduced (seconds) times. Moreover, area detectors record part or even whole powder diffraction rings, enabling effects such as texture, granu-

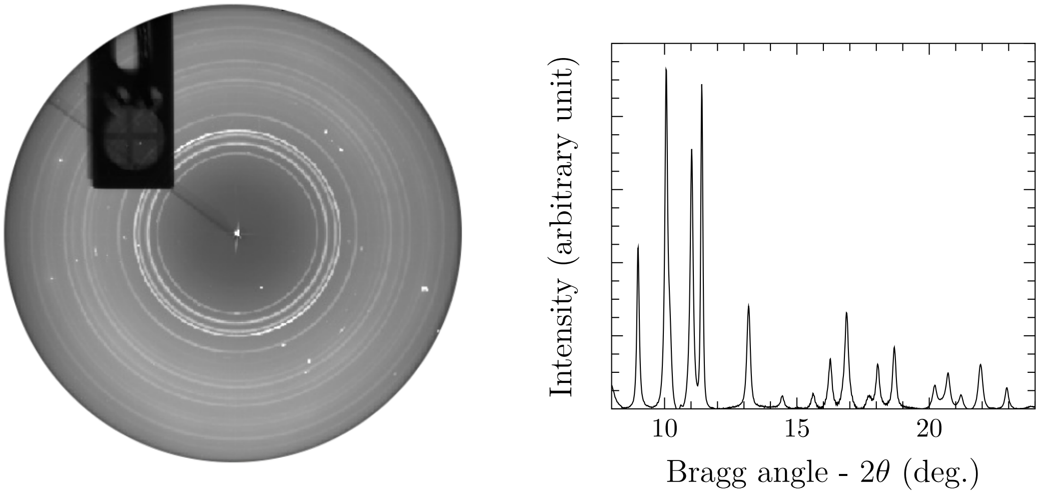

Figure 4-1: (left) Debye rings and (right) powder diffraction pattern from a fine grained sample of Nb_3Sn.

larity, and preferred orientation to be observed directly.

The 2D images obtained have been reduced to Intensity-2θ plot (see for example fig. 4-1-right). Because of their considerable weight, large area detector are not easy to handle or to align exactly. Moreover, detector spatial distortion due to the manufactoring can lead to inaccurate measurements. For this reason, first of all, the instrumental geometry requires a proper calibration that is obtained measuring and refining the diffraction pattern of a reference compound. Typically LaB_6 certified from NIST laboratories is used. By centering the Bragg rings of the standard on the primary beam position, and overlapping them to the known circular rings of the standard it is possible to obtain all the calibration parameter. They are in general six independent parameters: the distance between the sample and detector, two orthogonal tilt angles of the detector, two orthogonal detector coordinates for the position of the beam centre, and the wavelength of the X-rays. The calibration procedure, as well as the data reduction from 2D patterns to 1D plots, i. e. intensity versus the diffraction angle 2θ, has been done using the DAWN software [100]. An example of the calibration with the LaB_6 standard is shown in fig. 4-2, where the results of the parameters calculated by the DAWN software are also present, except for the beam

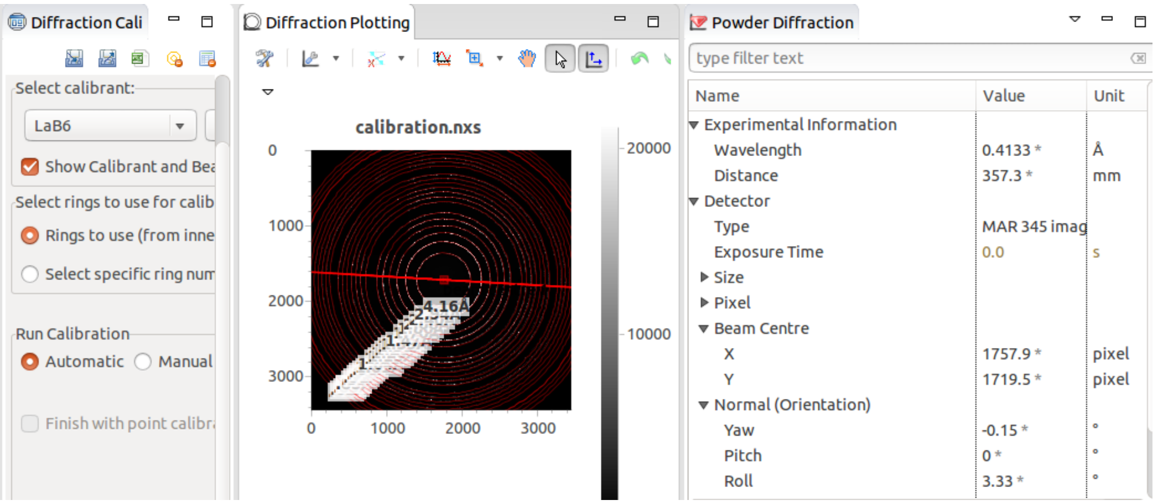

Select calibrant: LaB6

Name	Value	Unit
Experimental Information		
Wavelength	0.4133 *	Å
Distance	357.3 *	mm
Detector		
Type	MAR 345 imag	
Exposure Time	0.0	s
Size		
Pixel		
Beam Centre		
X	1757.9 *	pixel
Y	1719.5 *	pixel
Normal (Orientation)		
Yaw	-0.15 *	°
Pitch	0 *	°
Roll	3.33 *	°

Figure 4-2: Example of LaB_6 calibration for the diffraction patterns.

energy that has been fixed from the beamline monochromator calibration. After calibration the diffraction pattern has been masked to remove overexposed spots and portions of the area detector that were hidden from obstacles (like the beamstop). The next step was the conversion of the 2D images into 1D data by azimuthal integration (see the result of this operation in fig. 4-3). The diagram on the left shows the raw data after integration of a 2D imaging plate pattern. After background correction, using a 13 degree polynomial, the diffraction pattern results as in fig. 4-3-right. This background is mainly attributed to the Compton scattering of the diamonds [95]. The data so obtained are ready for the analysis.

4.2.2 HP-XRD diffraction at room temperature

This X-ray diffraction experiment was performed on the I15 beamline at Diamond Light Source [101] using an incident monochromatic beam with a wavelength $\lambda = 0.4133$ Å (E $\approx$ 30 KeV). The X-ray signal diffracted by the sample has been collected on a MAR345 imaging plate system, located at a distance of 350 mm from the sample. Several Nb_3Sn grains and a ruby crystal were loaded in the high pressure chamber of two membrane DAC (described in app. C) (fig. 4-4) with 200 μm and 500 μm culet size, respectively. The DAC with the larger culet size allowed measure-

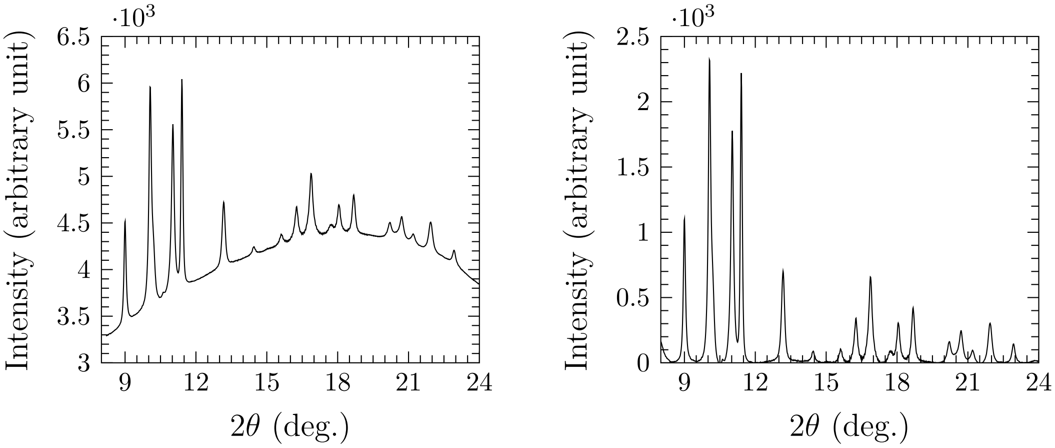

Figure 4-3: (Left) Diffraction pattern of the data at 2.56 GPa (run2) after 2D image integration and (right) after a 13 degree polynomial background subtraction.

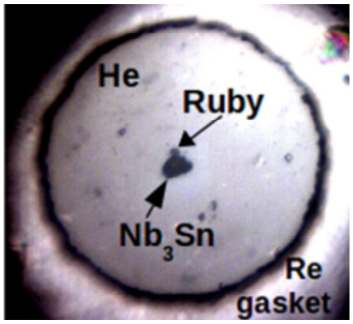

Figure 4-4: Picture of a sample completely embedded in the pressurized He transmitting medium, with the ruby pressure gauge near the sample.

ments up to ∼ 10 GPa, while with the other, with a smaller culet size, measurements up to 45 GPa have been possible. A 200 μm-thick Re sheet was used as a gasket, drilled by spark erosion. The samples were obtained by grinding Nb_3Sn filaments of the Nb_3Sn wire described in sec. 3.1. The samples were embedded in pressurized He transmitting medium to ensure hydrostatic conditions. During the experiment the pressure was measured from the fluorescence of the ruby gauge, according to the calibration [102], as explained in appendix C. All measurements were made at room temperature. The exposure time for each XRD pattern was between 100 s and 120 s. The diffraction geometry was determined using a LaB_6 reference sample [103] [104]. The diffraction patterns were integrated using the DAWN [100] software.

In Fig. 4-5 the measured powder diffraction pattern at the lowest and the high-

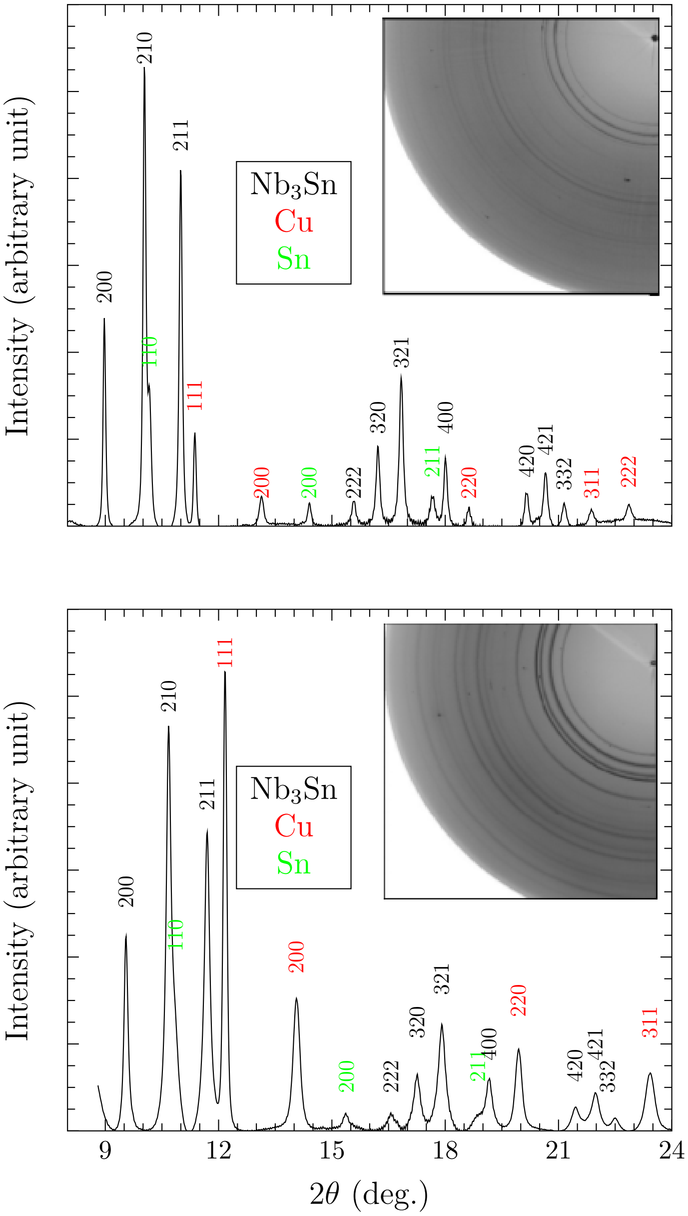

Figure 4-5: Integrated powder X-ray diffraction patterns of the samples (powdered filaments of Nb_3Sn) at lowest (upper panel) and highest (lower panel) pressure reached. Diffraction peaks of Nb_3Sn (black), Cu (red) and Ta (green) are labeled by colors. The insets show a part of the recorded raw diffraction images.

est pressures reached in the experiment are plotted together with the corresponding integrated signals. No intensity variation around the rings can be appreciated in the whole pressure range investigated, as shown in the two representative diffraction images of fig. 4-5, meaning that the samples do not have any preferred orientation of the crystallites or texture. In both panels the presence of Ta and Cu is detected, coming from the Cu matrix and the Ta-Nb diffusion barrier (see sec. 3.1). The indexing of the peak, also shown in fig. 4-5 has been obtained with the GSAS/EXPGUI software [105], taking as model the CIF files of Nb_3Sn, Ta and Cu from the Crystallography Open Database (COD) [106] and verified using the Bragg law (4.1) combined to the relation:

$$\frac{1}{d^2} = \frac{h^2 + k^2 + l^2}{a^2} \tag{4.8}$$

The quantitative analysis of the diffractograms has been carried out by two methods.

A preliminary analysis (peak position analysis) has been performed by fitting some representative peaks of the patterns in order to obtain their position, amplitude and width. The fits were made with the Gnuplot software. In particular a macro has been written in order to have a quick preliminary analysis tool before moving on to the more sophisticated Rietveld refinement. Gnuplot contains routines for non-linear least square analysis that can be quickly and efficiently used for preliminary purposes. From the position of the Bragg peaks, the lattice parameters and then the volumes have been computed. Three representative Nb_3Sn peaks, (400), (321) and (222) were fitted each to a pseudo-Voight function being a linear combination of a Gaussian curve $G(x)$ and a Lorentzian curve $L(x)$:

$$f\left(x\right) = A\left(\eta L\left(x\right) + \left(1-\eta\right) G\left(x\right)\right) + bkg, \tag{4.9}$$

where η and $1-\eta$ are the measure of the lorentzian and gaussian contribution to the shape of the peaks, respectively, and bkg is a linear background. The free parameters of the fit are the position, amplitude and width of the peaks, and the coefficient of the linear background.

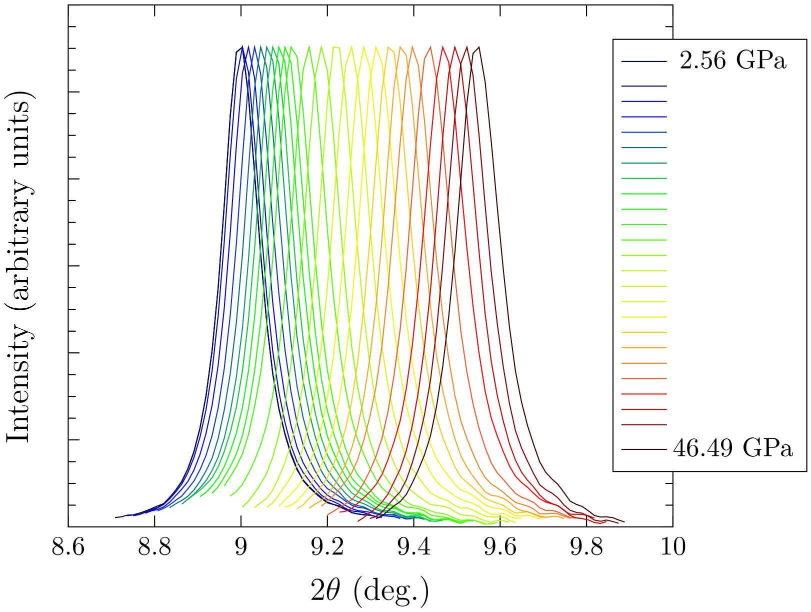

Figure 4-6: The 200 diffraction peak of Nb_3Sn at all the pressures of run2.

The more accurate analysis is based on the Rietveld method (described in sec. 4.1). Rietveld refinements of the diffraction patterns have been carried out using the GSAS/EXPGUI software [105]. Since the Rietveld refinement refines the entire spectrum, the three phases (Nb_3Sn, Ta and Cu) have been analyzed together. A constant wavelength (CW) profile function number 2, as described in the GSAS manual [107], has been used for the peak profile: this is a modified pseudo-Voight function, the so-called Thompson modified pseudo-Voight [108]. A 13 coefficients Chebyshev polynomial function is used to model the full profile background. For each of the three phases the free parameters for the Rietveld refinements are the lattice constant, the scale factors for each phase, the isotropic temperature factors (Uiso), the Gaussian coefficients, GU, GV, GW and GP and the Lorentzian coefficients, LX and LY. The lattice constant is related to the peaks position while the scale factor and Uiso contribute to the intensity of the peaks. The peaks shape is determined by the Gaussian and Lorentzian coefficients that are related to properties of the samples, such as microstrain and particle size.

In fig. 4-6 a single peak (the 200 of Nb_3Sn) is plotted at all the pressures of the run2. The peak position moves to higher 2θ values as pressure increases because lattice

constant gets smaller with compression. As far as it can be appreciated by eye there is no peaks broadening. However the peaks broadening will be discussed more in detail later in this section.
Looking at the diffraction patterns in fig. 4-5, no peak splitting or merging is observed in the Nb_3Sn signal as pressure increases: hence, no structural phase transition is expected. This also holds for Cu and Ta that, as already known, do not show structural phase transitions in the explored range of pressures.

The volumes of the Nb_3Sn cell obtained were plotted as function of pressure in fig. 4-7. In the P-V plot of fig. 4-7-upper panel there are no evidences that could be attributed to a structural phase transition. P-V data were fitted to the Rydberg-Vinet equation of state (EoS) [109] for isotropic compression:

$$P(V) = 3K_0 x^{\left(-\frac{2}{3}\right)}\left(1 - x^{\frac{1}{3}}\right) \times \exp\left[\frac{3}{2}\left(K_0' - 1\right)\left(1 - x^{\frac{1}{3}}\right)\right] \tag{4.10}$$

where $x = V/V_0$, V_0 is the volume at the atmospheric pressure and K_0 and K_0' are the bulk modulus and its pressure derivative respectively. The small systematic shift between the data sets in fig. 4-7 is charateristic of the angular dispersive detector used, due to the highly correlated geometrical parameters that describe such a type of detection method. However, this does not affect the relative shifts of lattice parameters and volumes obtained at different pressures in this work, as the sample has not been moved during each run after the initially calibration and alignement.
The normalized difference between experimental $V(P)$ and the fit curves, namely $\frac{V_{exp} - V_{fit}}{V_{exp}}\%$, is plotted in the lower panel: a deviation from isotropic compression is evident below ~10 GPa. This hints the possibility of an anomalous behaviour of the

Table 4.1: The V_0, K_0 and K_0' values from the fits of $P - V$ data.

run1			run2		
V_0 (Å^3)	K_0 (GPa)	K_0'	V_0 (Å^3)	K_0 (GPa)	K_0'
147.80 ± 0.03	171 ± 4	4 ± 1	148.7 ± 0.1	169 ± 4	3.4 ± 0.2

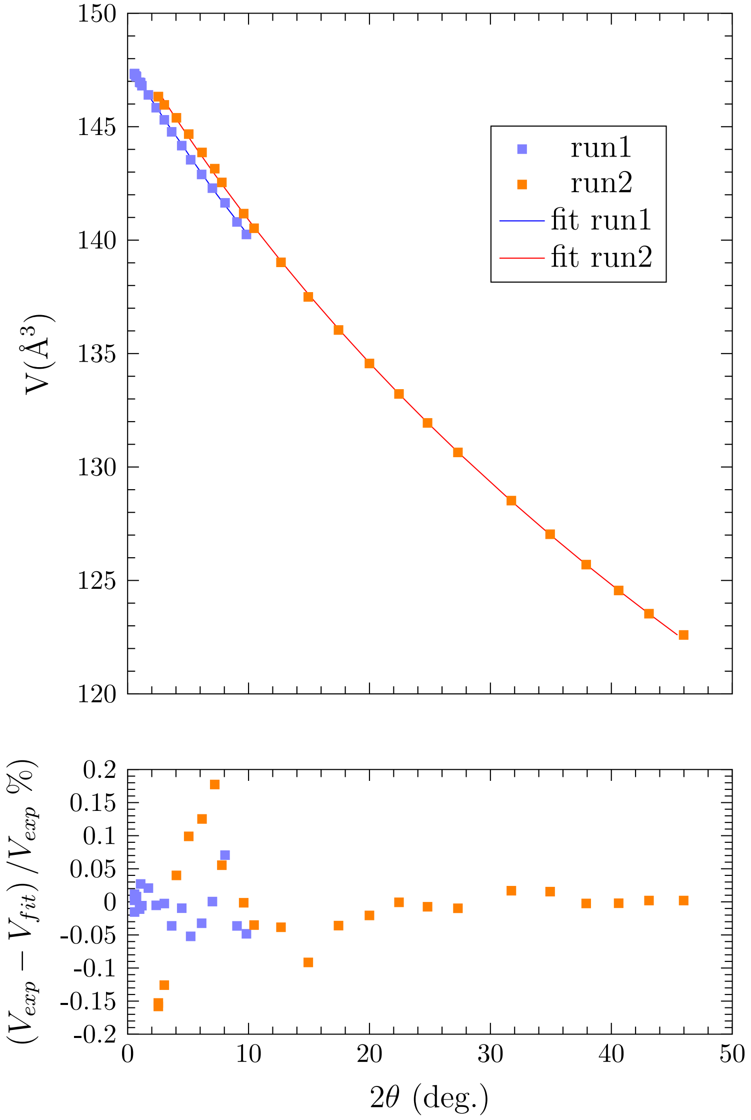

Figure 4-7: (top): measured volume of Nb_3Sn as a function of the pressure. (bottom): difference between measured and fitted volume, with the anomaly below 10 GPa.

compressibilty of Nb_3Sn when a pressure in the range 0-10 GPa is applied.

The results from the two runs are in agreement, except for a weak change of V_0 that is influenced by the small shift between the two sets of data (see table 4.1). Moreover, the values are in agreement with those reported in literature, where a V_0 of 148 Å^3 and a bulk modulus of 160 GPa have been reported [110].

The anomaly is more evident if one focuses on the difference between the positions of the peaks corresponding to different crystal directions, $2\theta(hkl) - 2\theta(h'k'l') = \Delta_{hkl,h'k'l'}$. In particular, we focus on the relative positions of three peaks: (400), (222) and (321).

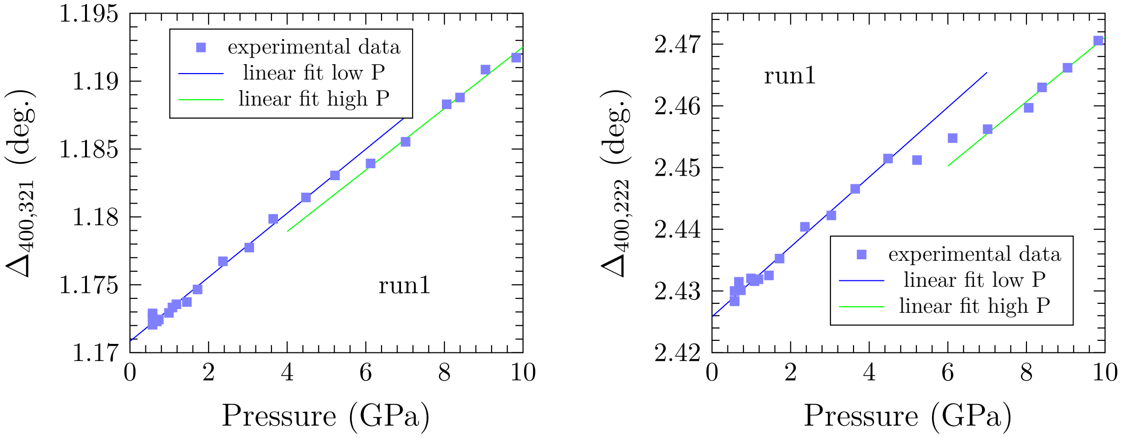

Figure 4-8: Peak position differences, $\Delta_{400,321}$ and $\Delta_{400,222}$, as function of pressure: an anisotropy of the elastic properties around 6 GPa can be seen.

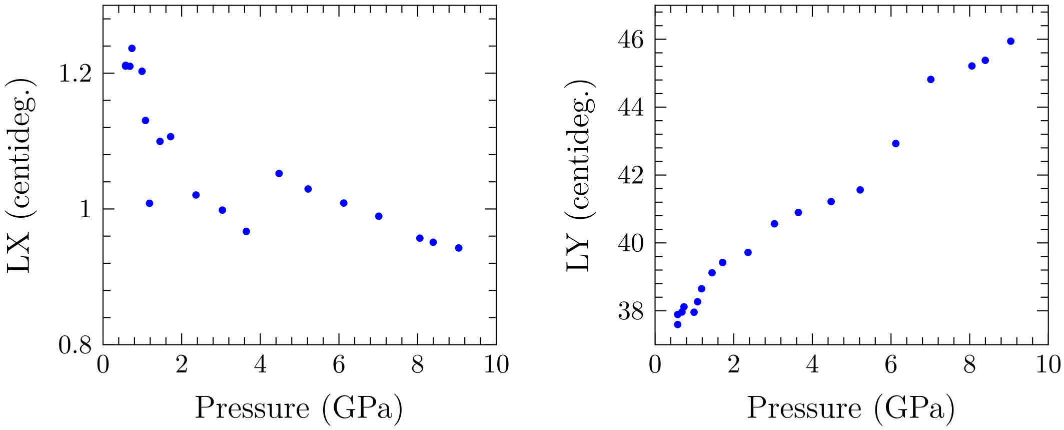

Figure 4-9: The specimen-broadening parameters LX and LY relative to run1.

$\Delta_{400,321}$ and $\Delta_{400,222}$ are plotted in fig. 4-8: they increase as a function of pressure but a plateau around 5-6 GPa can be seen in both cases. Even if no structural phase transition occurs, this finding (fig. 4-8) suggests an anomalous behaviour as a function of pressure: the compressibility along the direction (400) seems to vary in a different way with respect to the (321) and (222) directions, suggesting some anisotropy of the elastic properties. This type of information cannot be obtained from the Rietveld refinement where the positions of the peaks are constrained to the structure, so, despite the simplicity of the method, an additional information otherwise unobservable has been obtained and can be related to the anomalous behaviour of the residues (EoS fit in fig. 4-7) found by Rietveld analysis.

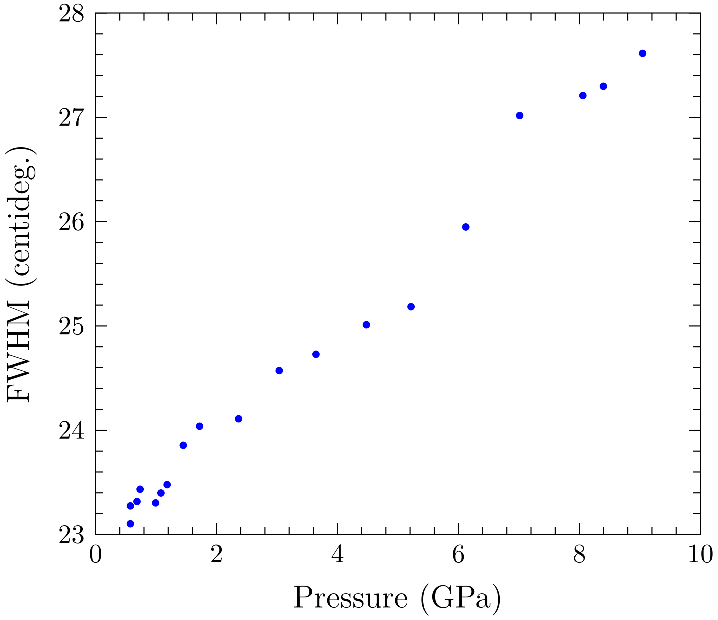

Figure 4-10: FWHM at $\theta = \pi/6$ relative to run1.

The Rietveld analysis also gave information about the broadening of the peaks due to properties of the samples, such as the crystallite size, inversely proportional to L_X, and the microstrain, proportional to L_Y. L_X and L_Y of run1 are reported in fig. 4-9. In particular, L_Y shows an interesting behaviour: it increases with a slope gradually lower up to 6 GPa and then continue to increase with the same slope after having abruptly moved to higher values. In the present work the behaviour observed for L_Y means that microstrain, that is proportional to L_Y, increases in the whole pressure range considered, but in correspondence of the anomaly above described its trend changes. This is another evidence for the compressibility anomaly at about 5-6 GPa. The FWHM of the peaks at each angle is a function of L_X and L_Y, as expressed in the following formula:

$$FWHM(\theta) = \frac{L_X}{\cos\theta} + LY\tan\theta. \tag{4.11}$$

The FWHM of the peak at different scattering angles has been calculated by means of Eq. (4.11) and is reported in fig. 4-10. It increases with pressure, unlike as roughly observed in fig. 4-6. In general the FWHM of XRD peaks increases with external

Table 4.2: Rydberg-Vinet fit parameter for Cu and Ta relative to run1.

	Cu		Ta	
	from [111]	this work	from [112]	this work
V_0	47.1 ± 1	47.28 ± 0.02	36.01	35.92 ± 0.01
K_0	140 ± 4	132 ± 4	193 ± 3	166 ± 5
K_0'	5.52	5 ± 1	3.58 ± 0.11	3 ± 1

pressure because of the strain (micro or macro) created in the lattice due to the applied pressure and it varies in a systematic way in the hydrostatic limit. Indeed, here, the increasing behaviour is mainly dictated by the L_Y parameter, as can be observed by comparing fig. 4-10 and fig. 4.11. It can be seen in fig. 4.11 how the anomaly of the L_Y parameter also reflects in the FWHM. Thus the peaks broadening increase with pressure and and above the anomaly is greater than below it.

Finally, the Rietveld analysis gave additional information that has been used to evidence the above observed anomaly. Indeed, the presence of Cu and Ta allowed to have internal reference standards with which to compare the results. Then to better understand the anomaly observed the results of the Rietveld analysis on Cu and Ta have been considered. The Rydberg-Vinet fit results of Cu and Ta are reported in table 4.2, resulting in good agreement with reference values except for the bulk modulus of Ta which is smaller than that reported in literature. This difference results from the error on V_0 that originate in the systematic shift of the volumes, as discussed in describing the figure 4.7. The Cu and Ta data are useful because, knowing that for them there is no phase transition in the explored pressure range, they allow to evidence the presence of the deviation from the isotropic compression for which the Rydberg-Vinet equation is valid. In particular, the compressibility of the three phases were compared.

The compressibility of a system at constant temperature is given by $\beta = -\frac{1}{V}\left(\frac{\partial V}{\partial P}\right)$. The ratio between the compressibility of the different phases, $\frac{\beta_{\mathrm{Nb_3Sn}}}{\beta_{\mathrm{Cu}}}$, $\frac{\beta_{\mathrm{Nb_3Sn}}}{\beta_{\mathrm{Ta}}}$ and $\frac{\beta_{\mathrm{Cu}}}{\beta_{\mathrm{Ta}}}$ has been calculated where $\beta = \frac{V - V_0}{P - P_0}$ and V_0 is the volume at the lowest value of

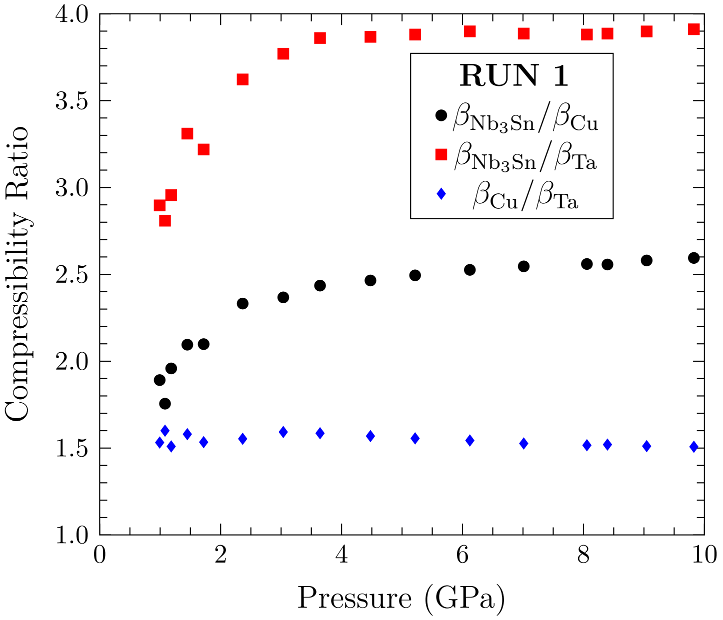

Figure 4-11: Ratio of the normalized volumes of the different phases.

pressure $P_0 = 0.57$ GPa. The $\frac{\beta_{Nb_3Sn}}{\beta_{Cu}}$, $\frac{\beta_{Nb_3Sn}}{\beta_{Ta}}$ and $\frac{\beta_{Cu}}{\beta_{Ta}}$ are reported in fig. 4-11 in order to evidence different trends between the different phases. From literature the compressibility of Cu and Ta are 0.0073 GPa^{-1} and 0.0050 GPa^{-1}, then their ratio results to be 1.46. The ratio $\frac{\beta_{Cu}}{\beta_{Ta}}$ obtained in this work is constant with pressure increase and is ∼1.51, in agreement with the literature results. Instead, the ratios $\frac{\beta_{Nb_3Sn}}{\beta_{Ta}}$ and $\frac{\beta_{Nb_3Sn}}{\beta_{Cu}}$ increase for pressures up to about 4 GPa and then remain constant. This finding strongly supports the hypothesis that an anomaly in the compressibility is present in Nb_3Sn under hydrostatic compression in the few GPa region.

Anomalies in the P-V plane were observed also in Nb_3Al around 18 GPa [7] and in Nb_3Ga around 15 GPa [8], but still we are not able to establish if the nature of the anomalies observed is the same. In particular, these materials show a pressure induced isostructural phase transition where no significant volume collapse has been observed (see fig. 2-12). Since the crystal structure type does not change, it is the volume compressibility of the two materials that show an anomalous behaviour as pressure increases. It is known that most of the isostructural phase transitions are correlated with variations of the electronic structure. The case of Nb_3Al has been further studied by means of first-principles calculations [8] which suggested that a "d" like band of Nb at the Brillouin zone center is just below the Fermi level and moves above touching the Fermi level at a pressure of ∼17 GPa. Then, under further compression the band moves down below the Fermi level. The movement of this particular band, causing a change in the Fermi surface topology (electronic topological transition, ETT), has been proposed to explain the isostructural phase transition seen in Nb_3Al. Moreover, Reddy *et al.* [10] calculated also the band structure of different A15 compounds, showing that Nb_3Al, Nb_3Ga, Nb_3In, Nb_3Ge and Nb_3Sn are likely to show Fermi surface topology variations when a hydrostatic pressure is applied. In particular Nb_3Sn has been shown to exhibit the ETT at a pressure of 25 GPa, while it occurs at 21.5 GPa and 17.5 GPa in Nb_3Al and Nb_3Ga, respectively. While this work estimates a pressure for the ETT close to that of the anomaly in the compressibility, the value of pressure at which the ETT could occur in Nb_3Sn is very far from that where we observed the compressibility anomaly and then the two results could represent different findings. However, we cannot exclude that the compressibility anomaly of Nb_3Sn has some relation to changes in the electronic properties of the material under pressure (see chap. 6).

It is worth to remember here that we have studied Nb_3Sn samples taken from wires, where the presence of Ta affects the structural behaviour of the material, avoiding the tetragonal transition, for istance. This Ta addition could also affect the anomaly described above, that to be understood need a comparison with high pressure XRD studies on pure Nb_3Sn, not available to us at the time of this experiment.

In summary, this diffraction experiment shows a compression anomaly of Nb_3Sn below 10 GPa, without any structural phase transition. As a result of this work, Nb_3Sn with Ta and Cu additions seems to preserve its cubic structure up to ∼ 50 GPa. Neverthless, the anomaly detected suggests some deviation from isotropic compression, that to be better understood needs further studies.

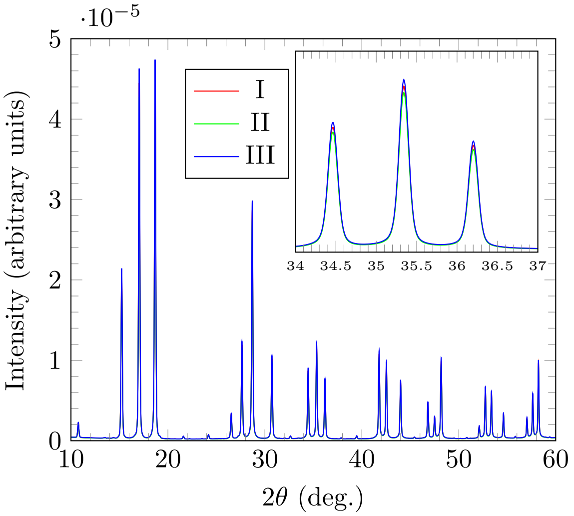

Figure 4-12: The three spectra collected 88 K. In the inset a zoom in the 34-37 degrees interval is shown.

4.2.3 XRD diffraction at low temperature

This X-ray diffraction experiment was performed on the MCX beamline at the ELETTRA synchrotron light source using an incident monochromatic beam with a wavelength of 0.7 Å (E $\approx$ 17.712 keV). The samples were powders taken from the polycrystalline laboratory samples described in sec. 3.2 contained in a 0.1 mm diameter glass capillary. The diffraction patterns were collected at ambient pressure and in the temperature range 300-80 K, at steps of around 10 K. Three scans were measured at each temperature for sake of comparison. Overall the spectra have been measured at forty-four temperature values, of which 22 on cooling and 22 on heating (measurements named from now on 'DOWN' and 'UP', respectively). The 2D images were integrated as described before and Intensity vs 2θ diffractograms were analyzed. For each temperature the three spectra have been compared in order to evaluate the quality of the data: no significant differences between the three spectra at every temperature have been observed, showing also the stability of the temperature during measurements (see for example fig. 4-12).

In fig. 4-13 a single peak (the 321) is plotted at all the temperature values of the DOWN run. The peak position moves to higher 2θ values as temperature decreases meaning that the lattice parameter gets smaller upon decreasing the temperature, as

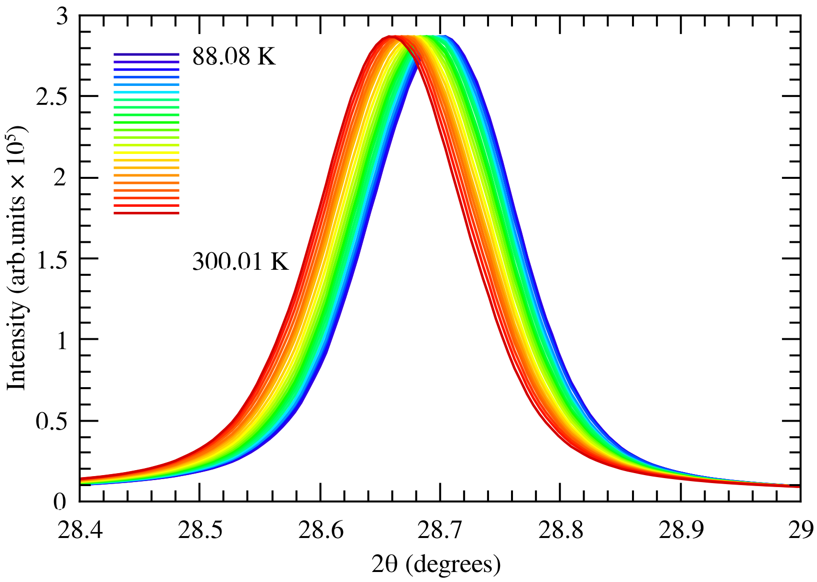

Figure 4-13: The Nb_3Sn 321 diffraction peak as function of temperature on cooling (DOWN run). The peak intensity has been normalized to the peak maximum. The very good statistical quality achieved by 2D setup can be appreciated.

expected, due to thermal contraction.

It is known, as already discussed in sec. 2.1.2, that Nb_3Sn has a simple cubic structure at room temperature and transforms into the tetragonal one at around 40 K. Then we expect that the structure of the studied sample is cubic in all the temperature range accessible for the present experiment. For this reason the spectra were analized taking as model a cubic lattice as explained in section 4.2.2.

The indexing of the peak has been obtained with the GSAS software, taking as model the CIF file from the COD [106] [113] and verified using the Bragg law combined to the relation 4.8, where the lattice parameter used has been taken from the room temperature value of 5.291 Å reported in [91]. For example, the location of Bragg peaks for a pattern at 88.08 K is shown in fig. 4-14.

In analogy with what has been done for the XRD experiment at high pressure, the analysis of the data has been conducted by means of the Rietveld method, in the same way as described in sec. 4.2.2. For example the fit obtained is reported in fig. 4-14. The profile function used for the refinement is the number 2 (described in the previous section) in the GSAS software. The free parameters during Rietveld refinement are

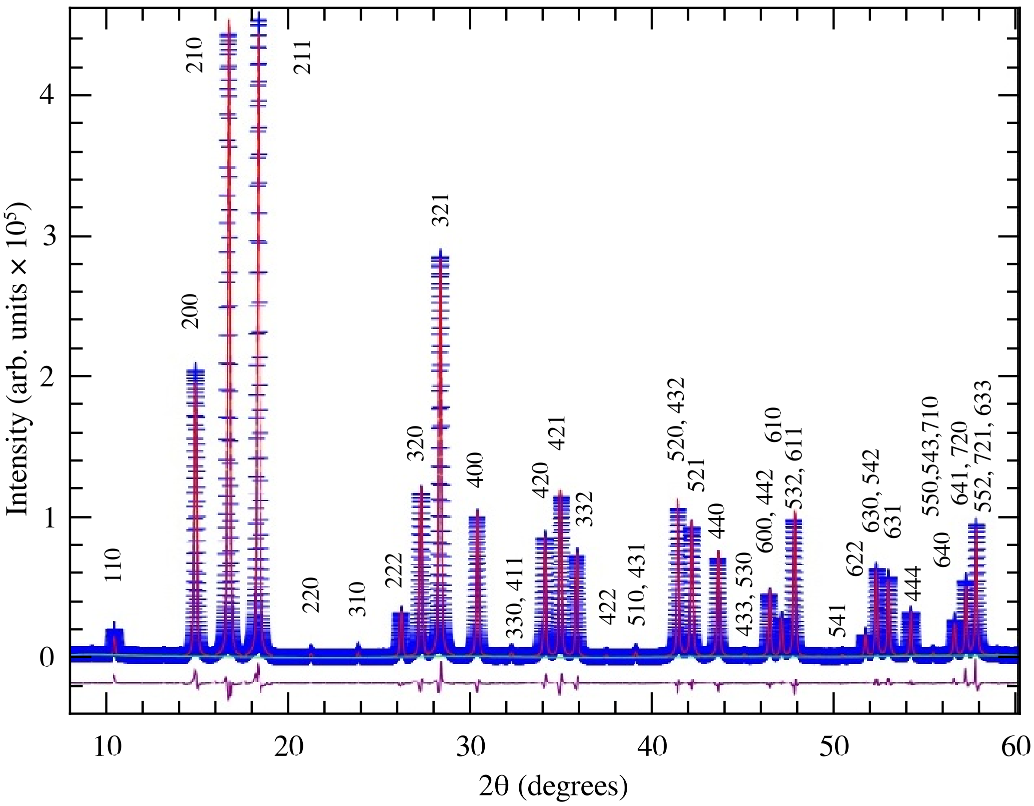

Figure 4-14: The diffraction pattern at 88.08 K (DOWN run): all the peaks are indicated. Superimposed the Rietveld refinement of the full spectrum obtained with the software GSAS/EXPGUI (red curve). The difference between the observed (cross symbols) and the fitted pattern is shown with a line at the bottom of the graph.

the lattice constant, the scale factor, the isotropic temperature factors (Uiso) for the Nb and Sn atoms, the Gaussian coefficients, GV and GW, and the Lorentzian coefficients, LX and LY. At each temperature value the three spectra were analized independently: this allowed an accurate evaluation of statistical uncertainty on the refined parameters. The results obtained from the fits of each triplet of spectra are in agreement, then for each temperature the results reported are the average of the three spectra and the uncertainty is calculated as $\frac{\sigma}{\sqrt{3}}$.

The room temperature volume and lattice parameter obtained from the Rietveld analysis are summarized in the table 4.3.

The lattice parameter and volume as function of the temperature are presented below, with particular attention to the presence of nonlinearities. The results presented come

Table 4.3: The volume and lattice parameter values from Rietveld analysis at room temperature.

Volume ($Å^3$)		Lattice parameter (Å)	
DOWN	UP	DOWN	UP
148.464 ± 0.001	148.161 ± 0.001	5.29510 ± 10^{-5}	5.29505 ± 10^{-5}

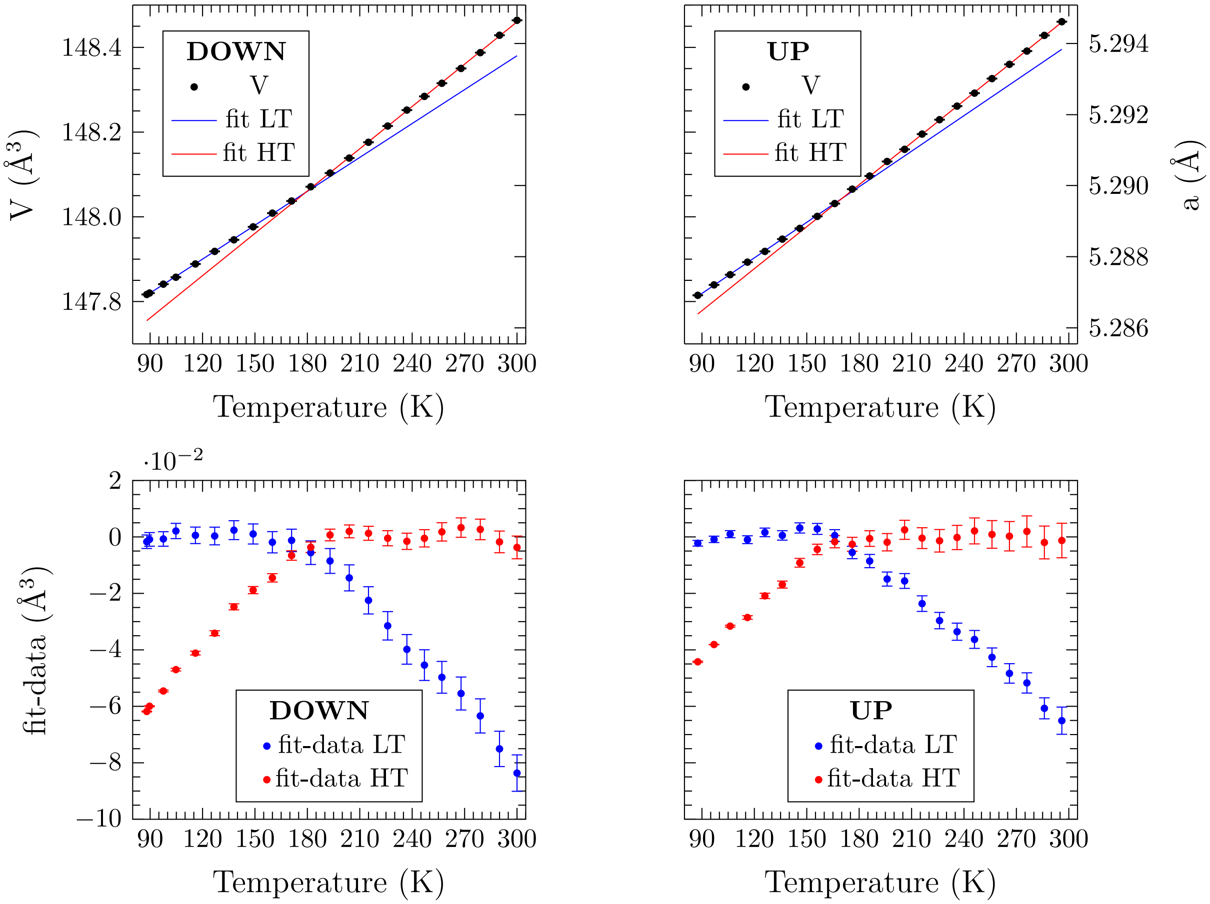

Figure 4-15: Top graphs: The volume and lattice parameter obtained with the Rietveld refinement of the data. Bottom graphs: the difference between the linear fit in the two regions, LT and HT, showing better the change of the lattice parameter slope.

from the Rietveld analysis. The volume, V, and the lattice parameter, a, are plotted against temperature in fig. 4-15 (upper graphs). A change in linearity around 180 K is present. The region above 180 K and that below this temperature (named HT and LT region, respectively) are well described by two different linear functions, where the slope in the LT region is around 20% smaller than that in the HT region showing

Table 4.4: Table of the thermal expansion coefficient.

	Results of Rietveld refinement			
	DOWN HT	UP HT	DOWN LT	UP LT
V_0 (Å^3)	148.061 ± 0.001	148.076 ± 0.001	147.813 ± 0.001	147.812 ± 0.002
K (10^{-5})	2.25 ± 0.02	2.23 ± 0.02	1.80 ± 0.01	1.85 ± 0.04

that at lower temperature the compressibility of the system is lower. Comparing UP and DOWN curves it is evident that this discontinuity is reversible and without any hysteresis.

The volume against temperature in the HT and LT region has been fitted to the thermal expansion law to evaluate the variation of the compressibility. The thermal expansion law is expressed as:

$$V(T) = V_0 + KV_0\Delta T, \tag{4.12}$$

where V_0 is the volume at the lowest temperature value of the considered range and K is the thermal expansion coefficient. The fit curves are plotted in fig. 4-15. The obtained thermal expansion coefficients are reported in table 4.4. The thermal expansion coefficient in the HT region is about 20% greater than in the LT region.

The UP and DOWN data give results in agreement with each other, hence from now on the discussion will refer only to the DOWN data set for easily reading.

The anomaly observed as a function of temperature is a novelty, not reported in literature (to our knowledge). In the following we try to understand the origin of such anomaly, in particular if there is some relationship with the known tetragonal transition expected around 40-50 K. For this purpose the lattice parameter at 40 K was calculated by using the thermal expansion law with V_0 and K obtained from the fit in the LT region and then it was compared to the value reported in literature (fig. 4-16). The lattice parameter obtained at 40 K is 5.286 ± 0.003 Å. We compared this value with that reported by Mailfert *et al.* [58], that is 5.281 Å, in order to see if the slope variation of the lattice parameter at 180 K leads to the value of the reticular

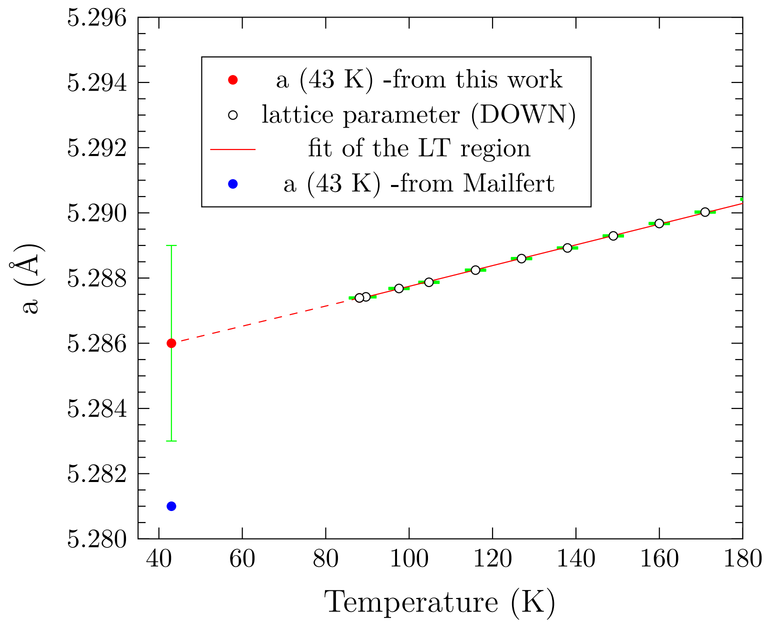

Figure 4-16: The lattice parameter has been extrapolated at 43 K to be compared with that reported in [58] (see fig. 2-4).

parameter that should have occurred immediately before the tetragonal transition. In the work of Mailfert the difference of the lattice parameter between room temperature and the tetragonal transition temperature (43 K) Δa is 0.014 Å, while we obtain a Δa of 0.009 Å: the order of magnitude of Δa is the same, signalling that with the slope of the lattice parameter found in the LT region the amount of thermal contraction between room temperature and ∼40 K is very similar to that obtained by Mailfert. This could mean that the slope variation up to 180 K could be considered as a precursor effect of the transition. However, this is only an hypothesis that could hold (if confirmed) if the lattice parameter evolves linearly as temperature decreases down to 40 K.

To deepen the meaning of the anomaly observed in the compressibility, the results of the Rietveld analysis were analyzed in greater detail. The refined parameters (Uiso and peak shape parameters) do not show significant effects at 180 K, except for the specimen-broadening parameters LX and L_Y, reported in fig. 4-17. LX has the same dependence on the scattering angle as the peak broadening due to crystallite size effects expressed as: $\beta_\tau = \dfrac{\lambda}{\tau \cos\theta}$, where β_τ is the peak broadening and τ is the average

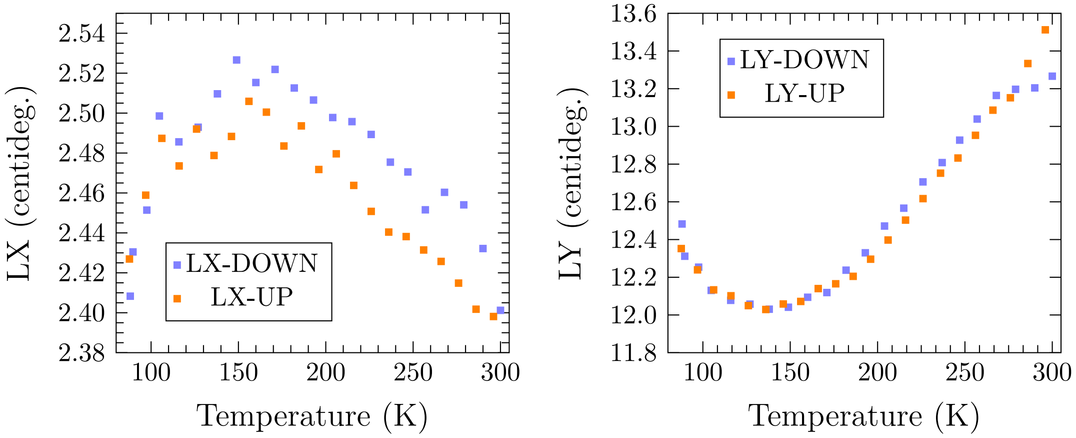

Figure 4-17: The specimen-broadening parameters LX and LY: again the anomaly at 175 K can be appreciated, here as an inversion of slope of the two parameters.

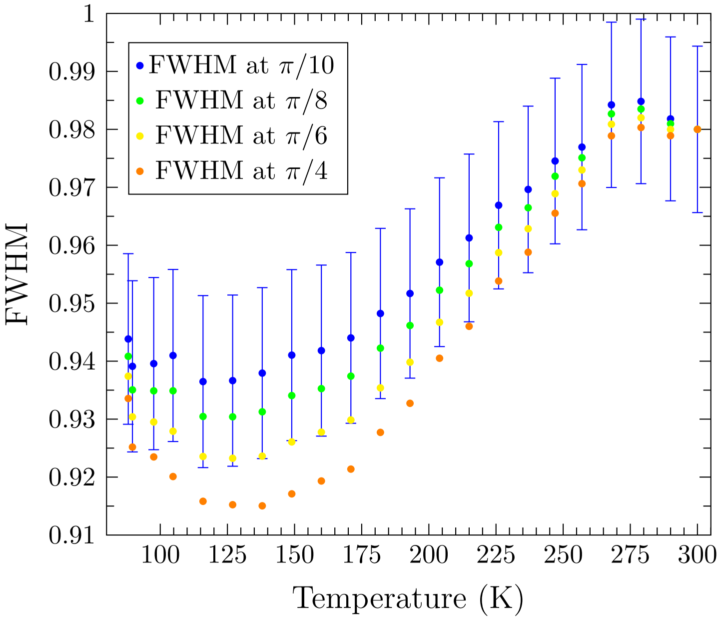

Figure 4-18: The FWHM at different values of the angle θ as function of temperature (from the DOWN set).

crystal size, while LY is proportional to the microstrain ϵ (expressed as: $\beta_\epsilon \propto \epsilon \tan\theta$, where β_ϵ is the contribution to the peak broadening of the microstrain). LX and LY contribute to lorentzian FWHM as expressed in (4.11). In fig. 4-18 the FWHM at different values of the scattering angle as function of temperature, normalized to the value of the FWHM at room temperature, is reported for the DOWN set of data. By comparing fig. 4-17 and fig. 4-18 it can be seen that the contribution of LY to the FWHM is larger than that of LX at all considered angles and temperatures, and then LY determines the overall behaviour of the FWHM as function of temperature. LX and LY seem to have particular behaviour with temperature, with change of slope around 150 K. However, these variations as function of temperature cannot be considered as anomalies because of the large error bars with respect to the variations themselves, that result in the large error bars of the FWHM in fig. 4-18.

As some authors have suggested precursor effects of the tetragonal transition at temperatures higher than 40-50 K (see chap. 1), the next step was to try to understand if the observed anomaly could be related to the tetragonal transition. For this reason the analysis of the data with the method of Rietveld refinement using as model the tetragonal phase ($P4_2/mmc$ space group) has been performed along the same lines described for the cubic phase. The results of the refinements obtained using the tetragonal structure are not better than those obtained using the cubic model, therefore we cannot establish that there is actually a tetragonal phase. However, in fig. 4-19 the ratio $\frac{c}{a}-1$ (differences between the ratio $\frac{c}{a}$ of the tetragonal phase and its expected value for the cubic phase, that is 1) as function of the temperature is plotted. The ratio $\frac{c}{a}-1$ increases lowering the temperature, with an abrupt rise below about 120 K. By extrapolating the $\frac{c}{a}-1$ we obtain 9.4×10^{-4}: this value is far from those reported by Godeke that are between 26 to 42×10^{-4} [31]. However we cannot state here if the behaviour of $\frac{c}{a}-1$ is linear in the temperature range from 120 K down to the tetragonal transition, but we cannot discard the hypothesis that the anomaly we saw at 120 K is not related to the tetragonal transition at around 40 K. Rather, we are confident that this anomaly is a precursor of the tetragonal transition. Support for this interpretation comes from past Raman studies, summarized in chapter 2, that pointed out a precursor effect for temperatures near our anomaly (around 100 K). This was observed as an inversion in the trend of the E_g mode that is related to the motion of the Nb atoms along the orthogonal chains (see fig. 2-8). The authors of [70] interpreted their results as deriving from small tetragonal domains forming even at temperatures also above 100 K. In analogy with [70] our finding suggests that

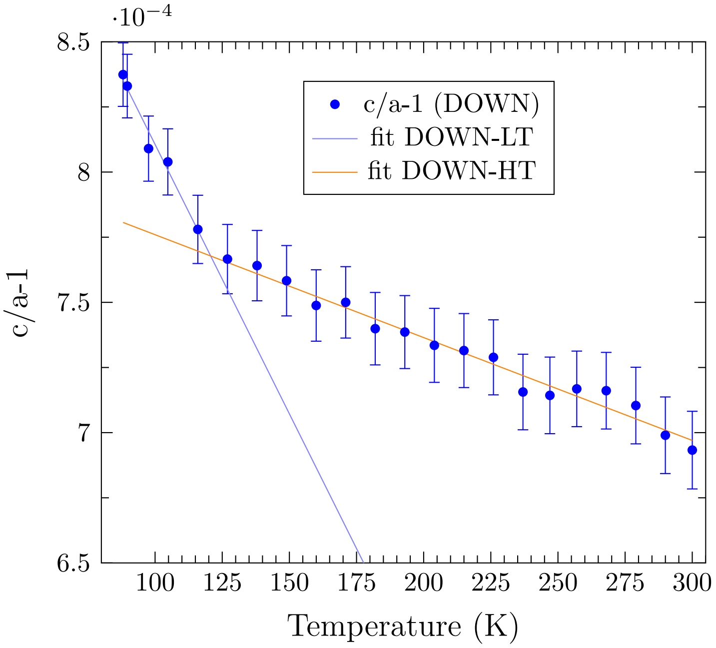

Figure 4-19: The ratio $\frac{c}{a} - 1$ as function of the temperature: an abrupt change of slope at around 120 K is present.

precursor effects may start already at 120 K.

In summary, the diffraction experiment as function of temperature gave us the following results:

- a compressibility anomaly around 180 K never observed before is present. It has been observed as a change of slope of the linear dependence of the lattice parameter (volume) as temperature decreases: in particular the slope decreases when crossing the temperature of $\sim$ 180 K, meaning that the compressibility of the material decreases below this temperature. In particular if the slope of the lattice parameter found in the LT region remains unchanged on further cooling, the resulting thermal contraction between room temperature and tetragonal transition temperature $\sim$40 K is very similar to that reported in literature by Mailfert [58]. This could mean that the slope variation up to 180 K could be considered as a precursor effect of the tetragonal transition. This hypothesis could hold if the lattice parameter evolves linearly as temperature decreases down to 40 K.

- an anomaly in the $\frac{c}{a} - 1$ is observed at 120 K, where a change of slope occurs. This results in an enhancement of the tetragonal deformation below 120 K, even if no tetragonal transition is here observed. This could be considered as a precursor effect of the tetragonal transition: it is observed here at 120 K, whereas past Raman studies suggest it starts from around 100 K [70].

The results obtained from XRD at high pressure and low temperatures described in this chapter contain previously unobserved information on the structural properties of Nb_3Sn. However, XRD studies give us average information about the samples, being based on a technique that detects only the long range order of a material. From this XRD characterization some anomalies are highlighted that need futher studies. In particular for a better understanding of what are the mechanisms underlying the observed anomalies a closer look at the short-range arrangement of the atoms is appropriate. For this reason, after this XRD characterization, we studied our samples by means of X-ray absorption spectroscopy, a local probe technique.

Chapter 5

High pressure EXAFS characterization

XAFS (acronym of X-ray Absorption Fine Structure) spectroscopy is a powerful non-destructive technique for local atomic structure and electronic characterization of matter. Owing its chemical selectivity and short range order sensitivity XAFS allows to investigate the short-range environment around a selected element in materials in any aggregation state (solid, liquid, gases) and morphology (thin films, rods, dots), in extremely variable situations (wide temperature, pressure, magnetic and electric field ranges) [114].
The phenomenon at the basis of the XAFS spectroscopy is the X-ray absorption (XA): in a very simple (toy) model (see fig. 5-1) an X-ray is absorbed by a core level of an atom and a photoelectron, promoted to the continuum states, interacts with the potentials of surrounding atoms and is scattered back to the absorbing atom. The interference between primary and backscattered photoelectron waves weakly modulate the X-ray absoption coefficient: such weak modulation (fine structure, FS) contains detailed structural information about the atomic structure just around the absorber.

In this chapter the theory allowing to describe the XAFS signal in terms of structural parameters will be described. Then, the high pressure experiment on Nb_3Sn, the data analysis and the obtained results will be discussed.

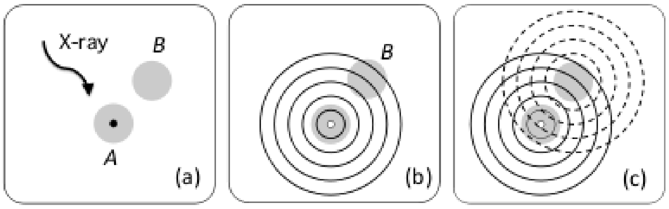

Figure 5-1: EXFAS phenomenon scheme: (a) the photon impinges the atom A (the black circle indicates the orbital of the core electron); (b) a core electron of the atom A absorbs the energy of the photon and is photoemitted. It is represented by its outgoing wave function (the white circle indicates the hole in the core state); (c) the outgoing and the backward diffused wave functions from the atom B interfere.

5.1 The X-ray absorption spectra

When an X-ray beam is trasmitted through a sample of thickness x, its intensity Φ_0 is attenuated according to the Beer-Lambert's law:

$$\Phi = \Phi_0 exp[-\mu(E)x], \tag{5.1}$$

where $\mu(E)$ is the linear absorption coefficient, that depends on the energy E of the incoming photon and on the composition and the density of the sample. The absorption coefficient is the quantity that is measured in a XAFS experiment.
Fig. 5-2 shows the typical trend of the absorption coefficient as function of energy E. Three general characteristics of the absorption coefficient $\mu(E)$ can be observed:

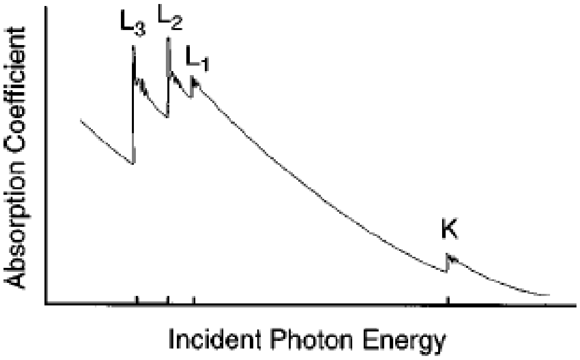

Figure 5-2: Absorption coefficient as function of the incoming radiation.

1. it decreases as the energy of the incident radiation increases, roughly as E^{-3};

2. it shows discontinuities (absorption edges) whenever the energy of the incoming photon is sufficient to excite an electron from a more inner shell. The absorption edges of different atoms correspond to different energies. Thanks to this, an important feature of XAFS spectroscopy derives: XAFS allows to selectively study the local structure of the different atoms present in a material;

3. when the absorber atom is embedded in a material (or polyatomic molecular gas) it is possible to see weak oscillations above the edge otherwise absent for isolated (monoatomic gas) atoms. These "fine structure" oscillations are typically weak, 1-10% of the jump edge discontinuity and represent the XAFS signal.

The XAFS signal is usually divided into two regions: XANES (X-ray Absorption Near Edge Structure) which indicates the threshold region and typically extends up to a few tens eV (50-100 eV) after the edge, and EXAFS extending several hundred eV over the XANES region to over 1.5 keV. The XANES region contains structural (coordination symmetry of the absorbing site) and electronic (oxidation state, density of empty states close to the Fermi level) information. Despite the potentially valuable information, the quantitative analysis of XANES features could be a difficult task owing the complex physics involved (full multiple scattering effect) and lacking of an analytical model for the data fitting [115]. On the contrary, the structural signal in the EXAFS region is easier to simulate as a combination of partial contributions allowing to describe the local structure around the absorber in terms of "neighbour coordination shells". The Gaussian model is generally valid for these shells, allowing a relatively simple analytical curve for data refinement (standard EXAFS formula, Eq. (5.14)) that provides the structural information in terms of the average coordination distance, multiplicity (coordination number) and disorder (variance of the distribution) [114].

Although the presence of a fine structure has been found since 1920 [116], XAFS was poorly considered until the 1970s, when the availability of the intense and continuous synchrotron radiation sources, the development of a more accurate theoretical model [117] [118] [119] [120] and the availability of powerful computers and advanced computational methods , have allowed XAFS to reach the front-line of science.
Several books and various review articles have been published on the different aspects of XAFS since then.
The first review on XAFS applications dates back to 1988 with the book of Koninsberger and Prins [121] where they described the spectroscopic techniques EXAFS and its surface extension SEXAFS, and XANES together with many examples of applications in several research fields.
Then, an important contribution to the EXAFS theory came with the work of Filipponi *et al.* [122], where the contribution of multiple scattering (MS) to the EXAFS region are developed in terms of n-body correlation functions and one of the software codes for EXAFS data analysis, GNXAS, is presented.
Finally, it is worth to mention the review of Rehr and Albers [123], where the theoretical advances that contribute to the understanding of EXAFS spectroscopy are discussed, focusing mainly on those occured in the nineties.

5.2 Origin of the EXAFS structure signal

In the extended region the structural EXAFS signal $\chi(k)$ is represented by the normalized difference:

$$\chi(k) = \frac{\mu - \mu_0}{\mu_0}, \tag{5.2}$$

between the embedded (μ) and isolated μ_0 atom linear absorption coefficients. Here k is the wave vector of the photoelectron given by $k = \sqrt{\left(\frac{2m}{\hbar^2}\right)(E - E_b)}$, where E_b is the energy of the electron in the core-orbital and E the photon energy.
In the following it will be shown how to interpret the structural information contained in the expression (5.2).

The absorption coefficient is defined as $\mu(E) = n\sigma(E)$ where n is the number of atoms per volume unit and $\sigma(E)$ is the absorption cross section, that is proportional to the probability w_{fi} that an electron in the initial atomic bound state $|\Psi_i\rangle$ goes into the continuum state $|\Psi_f\rangle$, due to the interaction with the electromagnetic field of X-rays. In the framework of the time-dependent perturbation theory to the first order, the probability w_{fi} is given by the Fermi-golden rule and the absorption coefficient results:

$$\begin{aligned}\mu(\omega) \propto |\langle\Psi_f|H'|\Psi_i\rangle|^2\rho(E_f - E_i - \hbar\omega) &= |\langle\Psi_f|\sum_j e^{i\mathbf{k}\cdot\mathbf{r}_j}\mathbf{p}_j\cdot\hat{\eta}|\Psi_i\rangle|^2\rho(E_f - E_i - \hbar\omega) \\ &\overset{dipole}{\approx} |\langle\Psi_f|\sum_j \mathbf{p}_j\cdot\hat{\eta}|\Psi_i\rangle|^2\rho(E_f - E_i - \hbar\omega). \end{aligned} \tag{5.3}$$

where the sum is over all the electron of the atom, $\rho(E_f - E_i - \hbar\omega)$ is the continuum density of states, with $E_f = E_i + \hbar\omega$, $\mathbf{p}_j$ is the momentum of the j-th electron and H' is the interaction term of the hamiltonian.

In the presence of an electromagnetic field the hamiltonian of a single electron system is expressed as:

$$H = \frac{\mathbf{p}^2}{2m} + V(\mathbf{r}) + \frac{e}{mc}\mathbf{A}(\mathbf{r},t)\cdot\mathbf{p} = H_0 + H'. \tag{5.4}$$

where H_0 is the hamiltonian of the isolated electron and $\mathbf{A}$ is the potential vector of the electromagnetic field, which is described by a sinusoidal time dependence, a polarization vector $\hat{\eta}$, a wave vector $\mathbf{k}$ and a frequency ω.

In the last step in formula (5.3) the *dipole approximation* has been applied, for which $e^{i\mathbf{k}\cdot\mathbf{r}} \approx 1$ when $|\mathbf{k}\cdot\mathbf{r}|^2 \ll 1$. The approximation is suitable because the electromagnetic field interacts only with a core orbital, whose extension is smaller than the X-ray wavelength. The transitions that contribute to the absorption coefficient, thus, are the allowed transitions in the dipole approximation. They are given by the following selection rules: $\Delta l = \pm 1$, $\Delta s = 0$, $\Delta j = \pm 1, 0$, $\Delta m = 0$. The wave functions Ψ_i and Ψ_f can be factorized in the contributions ψ_i and ψ_f of the active electron (the photoelectron) and Ψ_i^{N-1} and Ψ_f^{N-1} of the passive electrons: this is called the *one-electron approximation.*

In the EXAFS region the energy of the photoelectron is high enough to allow the interaction between the photoelectron and passive electrons to be neglected and the contribution of the passive electrons will be taken into account by the superposition integral of the passive electrons wave functions $S_0^2 = |\langle \Psi_f^{N-1} | \Psi_i^{N-1} \rangle|^2$ (*sudden approximation*). If these wave functions in the final state remain equal to the initial state, i.e., there is no relaxation, then $S_0^2 = 1$. S_0^2 represents an empirical parameter that in the analysis is fixed after the analysis of the EXAFS signal of a reference compound (same absorber). Typical values are in between 0.7 and 0.9.

A last approximation is to ignore the density of states $\rho(E_f - E_i - \hbar\omega)$ that in the EXAFS region varies in a negligible manner with energy.

As a result of the approximations made, the absorption coefficient becomes:

$$\mu(\omega) \approx S_0^2 |\langle \psi_f | \sum_j \mathbf{p}_j \cdot \hat{\eta} | \psi_i \rangle|^2. \tag{5.5}$$

Since the initial state of the photoelectron is that of its core-level, the calculation of $\mu(E)$ reduces to the calculation of the wave function of the final state of the photoelectron. The final state varies because of interference with the backscatterd waves from the neighboring atoms and produces the fine structure in the absorption coefficient.

The absorption coefficient in the case of an isolated atom is:

$$\mu_0(\omega) \propto \left| \langle \psi_f^0 | \mathbf{p} \cdot \hat{\eta} | \psi_i \rangle \right|^2 \tag{5.6}$$

where $|\psi_f^0\rangle$ is an outgoing wave function.

When the atom is in matter, the wave function of the final state in the position of the absorbing atom can be written as:

$$|\psi_f\rangle = |\psi_f^0 + \delta\psi_f\rangle \tag{5.7}$$

and the absorption coefficient becomes:

$$\mu(\omega) \propto \int d\mathbf{r} \left|\psi_f^0 + \delta\psi_f \mathbf{r} \cdot \hat{\eta}\psi_i^*\right|^2 \approx$$
$$\int d\mathbf{r} \left|\psi_f^0 \mathbf{r} \cdot \hat{\eta}\psi_i^*\right|^2 + 2Re \int \left[\psi_i \mathbf{r} \cdot \hat{\eta}\psi_f^{0*}\right] \left[\psi_i^* \mathbf{r} \cdot \hat{\eta}\delta\psi_f\right] d\mathbf{r}, \tag{5.8}$$

where the first term is just the absorption coefficient of an isolated atom, μ_0. By substituting (5.8) in (5.2) one obtains:

$$\chi(k) = \frac{2Re \int \left[\psi_i \mathbf{r} \cdot \hat{\eta}\psi_f^{0*}\right] \left[\psi_i^* \mathbf{r} \cdot \hat{\eta}\delta\psi_f\right] d\mathbf{r}}{\int |\psi_i^* \mathbf{r} \cdot \hat{\eta}\psi_f^0|^2 d\mathbf{r}}. \tag{5.9}$$

The numerator of (5.9) contains the product between two terms: the first represents the outgoing wave function of the photoelectron, while the second contains the $\delta\psi_f$, the modulation of the final state due to the backscattering effect. The product gives the interference at the origin of the EXAFS signal. The integral in the equation (5.9) is evaluated where $\psi_i \neq 0$, i. e. at the absorber atom position. The core state wave function is localized at the position of the absorber atom , in that way it acts as source and detector for the photoelectron making the XAFS technique a local probe.

In order to obtain the EXAFS function the final wave function has to be calculated. With reference to fig. 5-3, where the potential energy of the electron is approximated by a muffin-tin potential that consists of a spherical scattering potential centered on each atom (regions I and III) and a constant value in the interstitial region (II), the final wave function can be written as:

$$\psi_f \approx \psi_f^0 e^{i\delta_1} \left(\frac{e^{2ikR}}{R}\right) f_B(k,\pi) \left(\frac{e^{2ikR}}{R}\right) e^{i\delta_1} \tag{5.10}$$

where ψ_f^0 is the outgoing wave in the region I that is the same as for an isolated atom, the first $e^{i\delta_1}$ term is the phase-shift of the outgoing electron at the border of region I due to the interaction with the potential of region I, f_B is the backscattering factor that represents the interaction of the photoelectron with the B atom in the

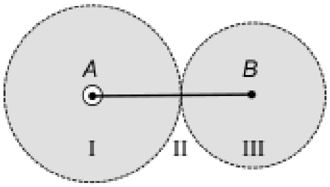

Figure 5-3: Scheme of the two atoms system: A is the absorber atom and B the backscatterer. The grey regions represent the muffin-tin potential spheres [115].

plane wave approximation where considering the high energy of the photoelectron, the scattering is considered on a spatial region very small with respect to the atomic distance R, the second $e^{i\delta_1}$ term is the phase-shift of the backscattered photoelectron due to the interaction with the potential of region I and the two equal factors $\frac{e^{2ikR}}{R}$ are the propagation of the spherical wave arriving on B in region II and the ones backscattered from B evaluated in region I. By substituting (5.10) into the EXAFS function (5.9), with $f_B(k,\pi)e^{2i\delta_1} = |f_B(k,\pi)|e^{i\phi}$ one obtains:

$$\chi(k) = S_0^2 \sum_j N_j \frac{f_{Bj}(k,\pi)}{kR_j^2} sin[2kR_j + \phi_j(k)], \tag{5.11}$$

where the index j identifies the j-th neighbour,R_j away from the absorber. Ideal crystallographic structures may have several neighbours strictly at the same distance (coordination shell), the N_j terms takes into account for such multiplicity (coordination number).

The transitions that contribute to $\mu(E)$ can be elastic or inelastic. In elastic transitions the passive electrons, simply relax their orbitals in presence of the core-hole left by the photoelectron. Instead in inelastic transitions after the absorption of the photon by the core electron, there are other excitations, the shake-up and shake-off processes, that involve the external electrons. So the absorption coefficient can be calculated as the sum of an elastic and an inelastic contribution.

Then, at this point, the inelastic term has to be included. This accounts for inelastic scattering events in which the photoelectron loses energy and cannot anymore go back to the absorber. These losses result in a damping of the final wave function that depends on the electron mean-free path $\lambda(k)$, leading to the decay factor $e^{-2R/\lambda k}$

on the EXAFS amplitude. In the EXAFS region the electron mean-free path takes values $\lambda \sim 10 - 20$ Å, contributing to make EXAFS a local probe.

Finally, in real systems at finite temperature the thermal vibrations must be taken into account along with possible static disorder (impurities, lattice local distortions): these introduce a configurational disorder giving rise to a distribution of neighbour in the coordination shells corresponding to a distribution of the neighbour distances. The sampling time of the photoelectron ($\sim 10^{-16}$ s) is much shorter than the atomic vibrational periods ($\sim 10^{-13}$ s). This means that in an EXAFS experiment one samples a distribution of istantaneous interatomic distances, $\rho(r)$, for each coordination shell [124]. Thus, the EXAFS formula for one coordination shell can be more generally expressed as:

$$\chi_j(k) = (S_0^2/k)N_j Im \left\{ \frac{f_{Bj}(k,\pi)}{k} e^{2i\delta_1} \int_0^\infty \rho(r_j) \frac{e^{-\frac{2r_j}{\lambda}}}{r_j^2} e^{2ikr} dr \right\}, \tag{5.12}$$

where all the r-dependent factors represent the effective distribution of distances:

$$P(r,\lambda) = \rho(r_j) \frac{e^{-\frac{2r_j}{\lambda}}}{r_j^2} e^{2ikr} dr. \tag{5.13}$$

A simple model (generally valid) assume a Gaussian shaped $\rho(r_j)$ with average distance r_j and variance σ_j^2. For small degrees of disorder ($\sigma_j^2 \ll 1$), the $exp(-2r_j/\lambda)$ term can be considered constant [123], and the integral becomes the Fourier transform of a Gaussian shell giving rise to a $exp(-2k^2\sigma_j^2)$ in the EXAFS formula:

$$\chi(k) = S_0^2 \sum_j N_j \frac{f_{Bj}(k,\pi)}{k} \frac{e^{-\frac{2R_j}{\lambda(k)}}}{R_j^2} e^{-2k^2\sigma_j^2} sin[2kR_j + \phi_j(k)], \tag{5.14}$$

where:

$$\sigma^2 = \langle (r - \langle r \rangle)^2 \rangle \tag{5.15}$$

is the variance of the Gaussian distribution that represents the Mean Square Relative Displacement (MRSD) of the absorber-neighbour pair and enters the Debye-Waller factor of the EXAFS formula, $e^{-2k^2\sigma^2}$.

We notice that the Gaussian approximation is definitely valid in most of the EXAFS analysis, moreover it allows to take into account multiple scattering terms. The more sophisticated models (cumulant expansion) may apply for sophisticated analysis but require deep knowledge and great experience to avoid artifacts coming from the strong correlation among the cumulant terms.

5.3 EXAFS measurements on Nb_3Sn

Nb K-edge XAFS measurements on the laboratory polycrystalline samples have been carried out at the beamline BM23 of the European Synchrotron Radiation Facility (ESRF) [125]. The BM23 optical scheme is presented in fig. 5-4: it is located on a ESRF bending magnet with $B = 0.85$ T. The beamline has the maximum flux of 1.6×10^{12} photons s^{-1} (0.1 % bandwith^{-1}) at the ESRF critical energy of 21 keV, close to the Nb K-edge (about 19 keV). The first element in the optics hutch is a double-crystal monochromator fixed-exit double-cam-type monochromator. The two crystals are in (+,-) geometry and diffract in the vertical plane. The crystals are mounted on a single rotating plate. The first crystal is mounted on a double-cam system which maintains a constant height for the exit beam during a scan by changing the perpendicular separation of the crystals.

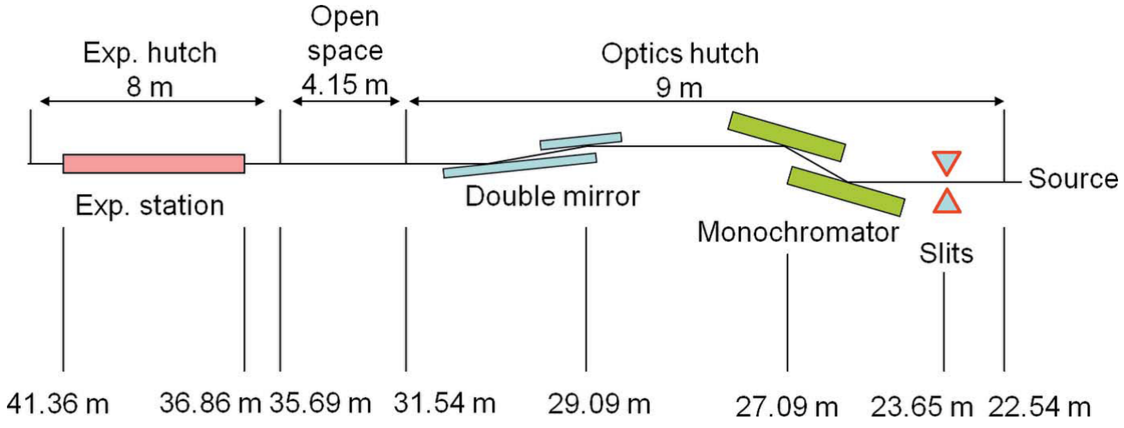

Figure 5-4: BM23 beamline: optical layout [125].

For the experiment the micro-XAS station has been used. It has a set of Pt-coated mirrors in a Kirkpatrick-Baez (KB) geometry in which the incident angle can be varied between 2 and 8 mrad allowing XAS experiments between 5 and 40 keV. The mirrors produce a focal spot of less than 4 μm × 4 μm FWHM. The stability of the beam is better than 1 μm keV^{-1} in both transverse directions. The micro-XAS station is also equipped with two mini ionization chambers for detecting the incoming and transmitted radiations and an optical microscope to inspect and align the sample on the X-ray spot.

The Nb K-edge XAS spectra were collected in transmission mode, at room temperature and pressures up to $\sim$ 30 GPa, using a DAC (see appendix C) equipped with nanocrystalline diamonds, Re gasket and silicone oil as pressure transmitting medium. Nanocrystalline diamonds are mandatory for collecting XAS at such high energy (19-20 keV), because single crystal diamond produces a large number of Bragg peaks giving rise to spikes and noise in the spectra. The finely grained samples are embedded in the silicone oil together with a small ruby allowing for pressure calibration using the ruby fluorescence technique (app. C).

The signal μ, proportional to the total absorption of sample and diamonds, is calculated as $\mu = \ln \frac{I_0}{I}$, where I_0 and I are the incident and transmitted intensities measured by the mini ionization chambers. As example, the measured absorption coefficient at the pressure of 7 GPa is plotted in figure 5-5. The fine structure oscillations are clearly visible above the Nb K-edge (18986 eV) extending more than 800 eV above the edge.

The analysis of XAFS data is performed in two main steps: the data reduction and the quantitative refinement of the EXAFS structural signal.
For the data reduction is used the ATHENA software [126]. This data treatment include various step, explained below.

- *pre-edge subtraction*: the pre-edge, μ_{pre}, is evaluated by a linear fit of the data before the edge and the $\mu' = \mu - \mu_{pre}$ is then calculated. μ_{pre} represents the

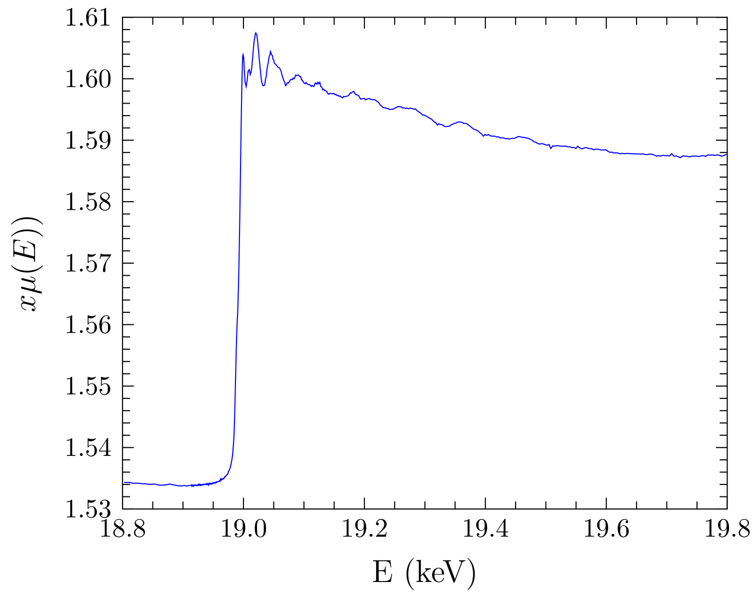

Figure 5-5: $x\mu(E)$ at 7 GPa.

absorption of diamonds, windows and any edge except the K-edge in the sample.

- *post-edge evaluation*: The post-edge μ_0, proportional to the bare atomic background is evaluated in ATHENA by means of a polynomial that approximates the trend of the region above the threshold. The pre-edge and post-edge functions have been calculated excluding the energy range near the threshold, which has a strong dependence on the local structure, dependence that the normalization constant must not have. The two functions, obtained with ATHENA, are plotted in figure 5-6.
- *normalization*: the EXAFS structural signal is calculated as $\chi = \dfrac{\mu' - \mu_0}{\mu_0}$.
- *energy scale*: the photoelecron wavenumber k is calculated choosing the threshold energy, $E_0 = 18986$ eV at 7 GPa. In ATHENA this is determined automatically with the first large peak in the first derivative of μ, but however it can be also selected manually, as it has been done here.
- *background subtraction*: it consists in removing from the spectra the low frequency components, while retaining the high frequency components. In order to eliminate the background contribution, ATHENA uses an algorithm (Autobk)

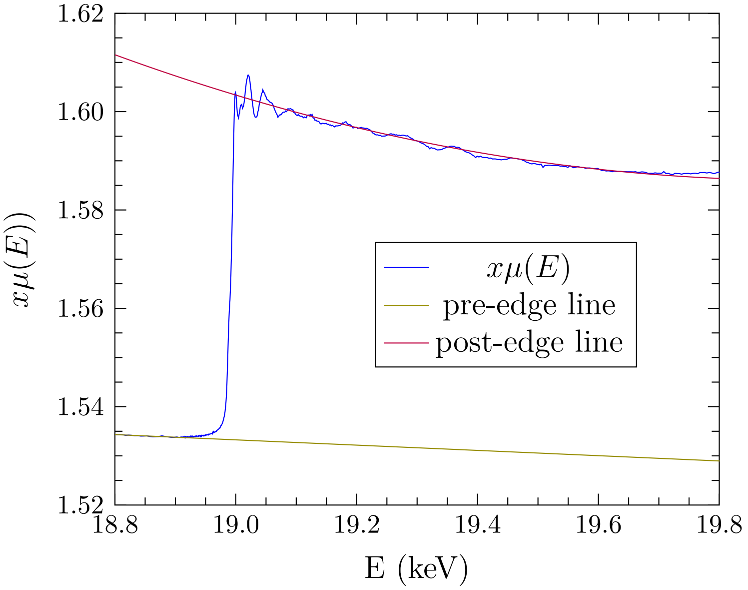

Figure 5-6: Pre-edge and post-edge subtraction and normalization at 7 GPa.

that is based on the Fourier theory: it subtracts from the absorption coefficient above the threshold a spline function thus going to minimize the Fourier components below a cutoff frequency. In Athena this frequency is defined through the parameter *Rbkg*; an acceptable value of this parameter is about half path from the first neighbor ($Rbkg = 1.3$ for this data reduction). In fig. 5-7 is shown the plot of the normalized absorption coefficient and the background calculated with ATHENA.

- the last step is to calculate the Fourier transform of the EXAFS function $\chi(k)$, i. e. the complex function $\chi(R)$.

In fig. 5-8 and 5-9 the obtained k^2-weighted $\chi(k)$ and the modulus of the FT at the different values of pressure are presented. k^2 weighting helped to compensate for the decay with k of $\chi(k)$, allowing to better highlight the features of the spectra at high k-values. From fig. 5-8 it can be seen that the amplitude of the EXAFS oscillations increases with pressure, meaning that the disorder decreases as pressure increases, as expected. Moreover, the EXAFS oscillations shift to higher k-values as the pressure increases, as it is usually expected due to the shortening of bond lengths. This is reflected in the peaks shift of $|\chi(R)|$ towards lower R-values (fig. 5-9). Indeed,

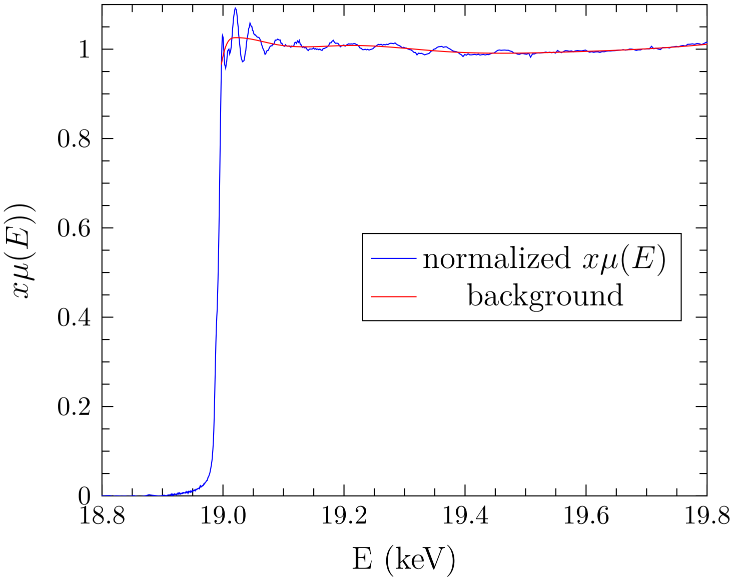

Figure 5-7: Background subtraction at 7 GPa.

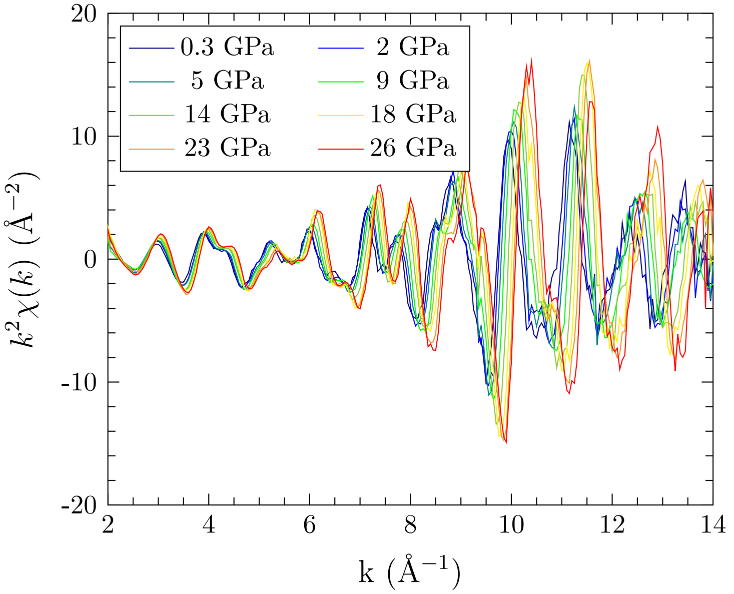

Figure 5-8: The extracted $k^2\chi(k)$ EXAFS signals as a function of pressure.

the positions of the peaks of $|\chi(R)|$ correspond to the interatomic distances, except for a systematic shift to lower R-values due to the scattering phase-shift $\phi(k)$ (see Eq. (5.14)). For most systems a crude approximation to the phase shift is $\phi(k) \sim -k$, which gives a peaks shift in $|\chi(R)|$ of -0.5 Å relative to the interatomic distances [127].

The preliminary analysis of the reduced data has been done using the ARTEMIS

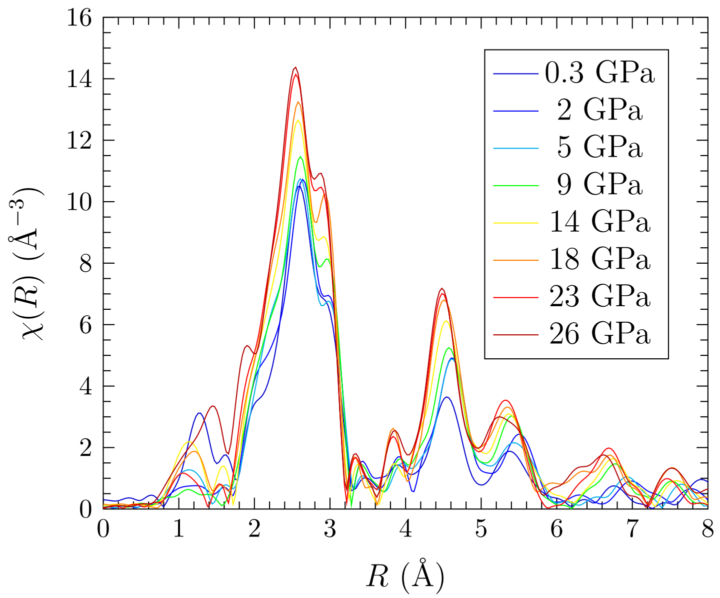

Figure 5-9: The magnitude of the complex $\chi(R)$ as function of pressure.

software [126]. Artemis works within the framework of the FEFF's multiple-scattering path expansion. Artemis models the data as a summation of contributions from one or more scattering paths. The fitting procedure included the following steps:

1. a cluster of atoms has been defined starting from the crystallographic structure described in a CIF file downloaded from the COD;

2. the ATOMS program, included in ARTEMIS, allows to read the crystallographic data of a selected material and convert it to a format suitable for FEFF, that starting from this theoretical crystal structure computes the list of possible scattering paths together with the amplitude and phase functions for each contribution, $f_B(k)$ and δ respectively, to construct the theoretical signals;

3. the first three paths corresponding to the first three neighbors have been selected for the analysis;

4. the fits were carried out by varying the following parameters: the displacement with respect to the theoretical distance *delr* that defines the interatomic distance and the MSRD factor σ^2. The coordination N of each shell is fixed to nominal values $N_I = 2$, $N_{II} = 4$ and $N_{III} = 8$, for the first (Nb-Nb), second

(Nb-Sn) and third (Nb-Nb) shell respectively. The amplitude S_0^2 is fixed to 0.8 for all the spectra, while the edge energy E_0 has been fixed to 18986 eV.

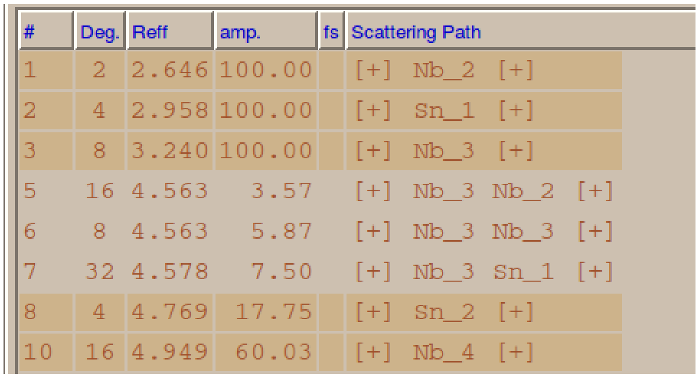

#	Deg.	Reff	amp.	fs	Scattering Path
1	2	2.646	100.00		[+] Nb_2 [+]
2	4	2.958	100.00		[+] Sn_1 [+]
3	8	3.240	100.00		[+] Nb_3 [+]
5	16	4.563	3.57		[+] Nb_3 Nb_2 [+]
6	8	4.563	5.87		[+] Nb_3 Nb_3 [+]
7	32	4.578	7.50		[+] Nb_3 Sn_1 [+]
8	4	4.769	17.75		[+] Sn_2 [+]
10	16	4.949	60.03		[+] Nb_4 [+]

Figure 5-10: The list of the first ten scattering paths produced after running FEFF on the ATHENA software. The following information about each path are given in the columns: (I col.) order of the path, (II col.) multiplicity, (III col.) half-length of the scattering path, (IV col.) relative amplitude and (V col.) path, where the backscatterer atoms are listed and the absorbing atom is indicated with [+].

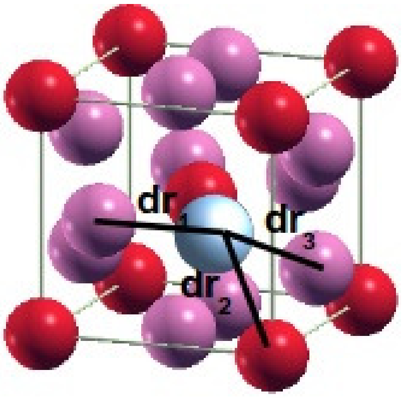

Figure 5-11: Scattering paths of the first three shells.

In fig. 5-10, the list of some of the first paths as has been obtained after running FEFF is shown. One can distinguish single- and multiple- scattering path. For example, the path number 1 in the list is a single-scattering path from the Nb atom to the first neighbor Nb atoms at a theoretical distance (R_{eff}) of 2.646 Å, with coordination $N = 2$ that gives a strong contribution to the EXAFS spectrum. The path number 5, instead, is a multiple-scattering path, where the photoelectron is diffused by two other Nb atoms before reaching the absorber atom. Here the coordination of the shell

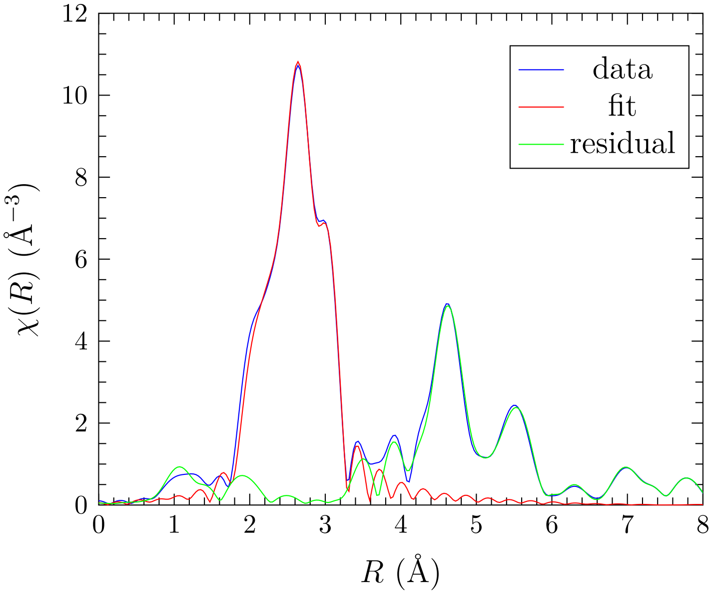

Figure 5-12: Result of the fit to the $|\chi(R)|$ function obtained with ARTEMIS at 2 GPa. The gray region is the fitting region.

is 16 and the theoretical path length is 4.563 Å.

For the analysis only the first three paths of the list have been taken into account. In fig. 5-11 the scheme of the Nb_3Sn cell is shown together with the paths that have been considered for the fit. The result of the fit at 2 GPa and 26 GPa is plotted in fig. 5-12 and 5-13. Visually they are good fit, but the values of the reduced chi square increase with pressure, from ∼7 at 0.3 GPa to ∼34 at 26 GPa, indicating that the model used for the fit does not describe the system as well as it does at low pressure. In fig. 5-14 and 5-15 the deviations from the theoretical bond length of each shell normalized to the theoretical lengths and the disorder as function of pressure are reported. From fig. 5-14 it is possible to see that the interatomic distances decreased in the same way along the directions of the considered three scattering paths, thus showing that compressibility throughout the range of pressures considered is always relative to a cubic system. The term of disorder of figure 5-15 decreases with increasing pressure, as expected, but is bigger in the case of Nb-Nb bonds with respect to the Nb-Sn bond. This means that disorder in the Nb chains is greater. More, the behavior is different for the different shells involved. The first and the third shell, involving only Nb atoms, show a discontinuity in the slope around 9 GPa. Above

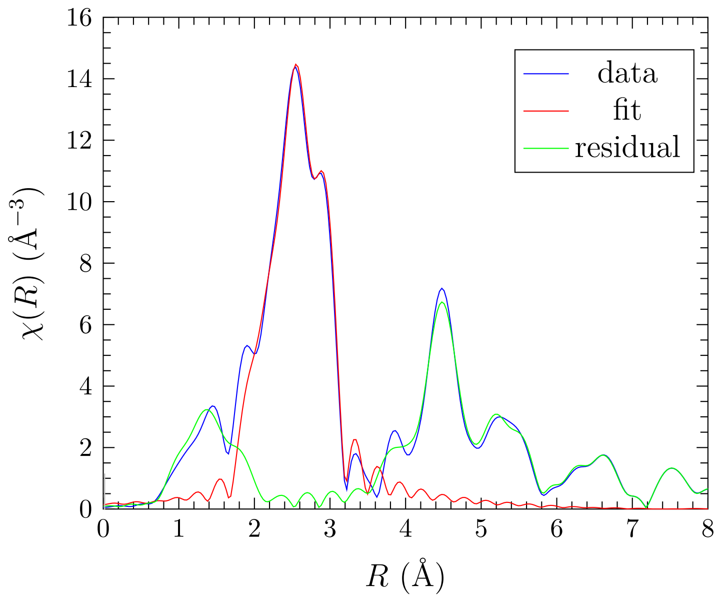

Figure 5-13: Result of the fit to the $|\chi(R)|$ function obtained with ARTEMIS at 26 GPa. The gray region is the fitting region.

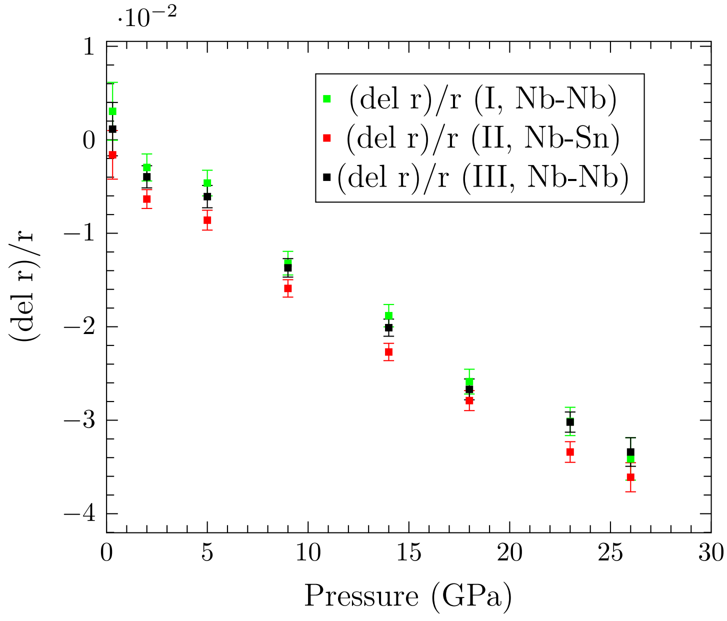

Figure 5-14: *delr* as function of pressure.

this pressure value the decreasing behaviour is very small in the case of the third shell, while the MSRD of the first shell remains constant. The second shell (Nb-Sn), instead, decreases linearly.

The observed discontinuities in the MSRD of the first and third shell could be related

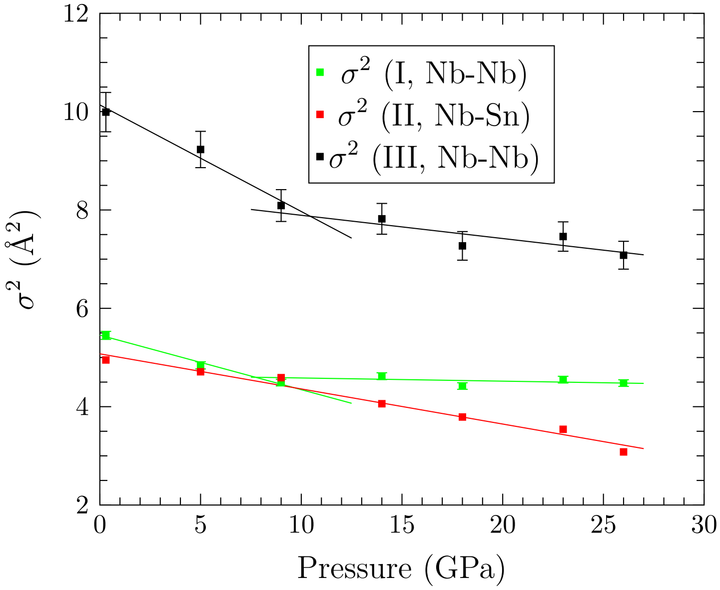

Figure 5-15: The MSRD factor σ^2 as function of pressure.

to distortion of the Nb chains that should be better investigated with a non-gaussian model. Indeed, it is known from literature that Nb_3Sn is characterized by a dimerization of Nb chains on cooling. If this is the case also when a pressure is applied, one has to take into account deviations to the Gaussian distribution, in particular deviation that results in an asymmetric shape of the distribution. This can be the reason why the fits with the Gaussian model lose in goodness with increasing the pressure.

Our preliminary analysis has been used as the starting point for a more sophisticated analysis carried out applying the Evolutionary-Algorithm Reverse Monte Carlo (RMC) method as implemented in the EvAX algorithm [128]. The RMS analysis has been carried out by I. Schiesaro in her degree thesis [129]. In the following the main results of this analysis are discussed.

5.4 Results from EA-RMC analysis

The EA-RMC analysis starts from an atomic cluster representative of the atomic structure in the sample. A cubic supercell made by 27 (3×3×3) unit cells (216 atoms) has been used, with periodic boudary conditions. The RMC process consists in moving randomly the atoms in the cluster. At each move a new EXAFS function is calculated and compared with the experimental spectrum. If the agreement improves the move is accepted, otherwise it's accepted with a defined probability. This allows to avoid local minima. An evolutionary algorithm is applied by EVAX in order to improve the convergence. The RMC model allows to generate a "model atomic cluster" for which the calculated EXAFS reproduces the experimental EXAFS. The EXAFS model is calculated including single and multiple scattering signals up to 5 scattering legs and 6.5 Å half length. Looking at the model cluster very precise details about the local structure in the supercell can be obtained. Data analysis procedure is better described in the master thesis [129]. Here we look at the main results, in particular concerning the Nb-Nb nearest neighbour distribution.

We focus here on the distances of the first three coordination shells (the ones before analyzed), the distributions of which are reported in fig. 5-16. From the histograms it is clear that the disorder of the three considered shells decreases with increasing pressure: in fact the distributions narrow with pressure. Interestingly, the first shell shows a higly asymmetric distribution at low pressure, with a long tail at low value of the path length, that changes into a bimodal distribution above 5 GPa.

To have a further indication on the possible motion of the atoms with the increasing pressure the correlation between the distances of the first shell have been studied. For each atom present in the Nb chain we calculated the distances of a Nb atom with the atom to its left and with the atom to its right. The distance of a Nb atom with the atom to its left was plotted as function of the distance with the atom to its right for all the pressure values in figure 5-17.

Observing the image starting from the lowest pressure it is possible to notice the simultaneous presence of two different behaviors. Some distances appear anti-correlated:

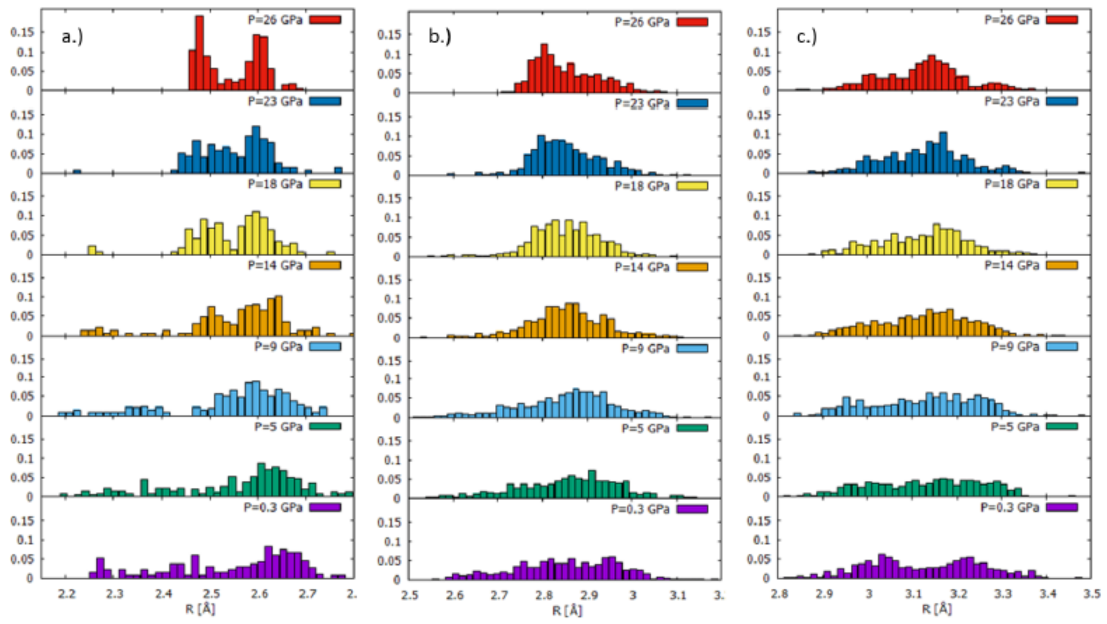

Figure 5-16: Distance distributions of the first (a), second (b) and third shell (c) at different pressures.

indeed, the data enclosed in the red ellipse in fig. 5-17 represent the situations where a long distance on one side of the central Nb atom is associated with a short distance on the other side (see the schematic representation of this motion at the bottom right of the figure, red circle). Instead, the data enclosed in the green circle take values between 2.4 Å and 2.7 Å and they are distributed in a compact and homogeneous way where long distances are associated with long distances and short distances with short distances (see the schematic representation of this motion at the bottom right of the figure, green circle).

When long and short distances alternates along a chain, there is a shift along the direction of the chain. while in the second case (green), in which the two distances vary by the same amount, it is possible observe a movement of the atom in the center in a perpendicular direction to the chain with a consequent variation of the angle between the three atoms. Comparing the graph at 0.3 GPa with that at higher pressures it is possible to notice how at the lowest pressure the distribution of the red distances is uniform. As the pressure increases, from 9 GPa onwards, the anti-correlated motion becomes increasingly weak until it disappears totally at 23 GPa. The increase in pres-

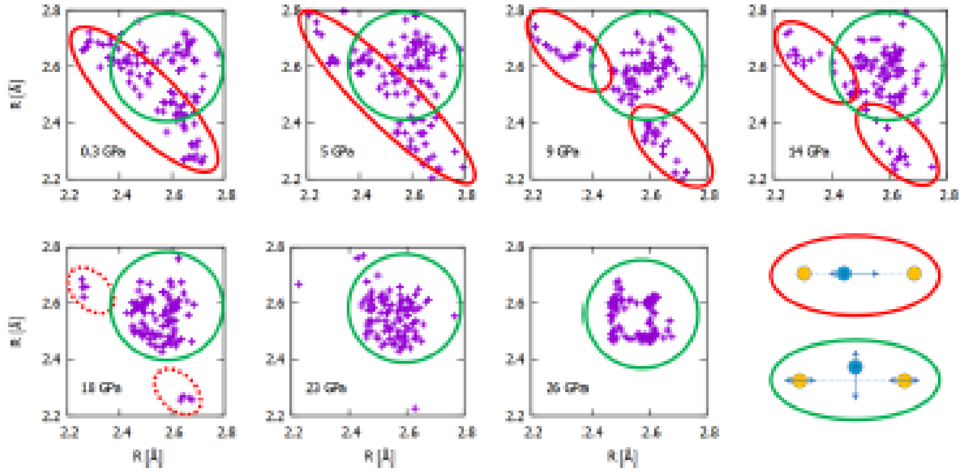

Figure 5-17: Correlation between first shell Nb atoms.

sure may be associated with one decrease in the degrees of freedom, and therefore to a limitation of the possible movements of atoms. The motion that associates a greater distance with a smaller one costs a lot in energy. In contrast, when the two distances vary by the same amount, it is possible observe a movement of the Nb atom in the center in a perpendicular direction. The behavior described here is in agreement with the results about the distribution of the distances described in fig. 5-16 where it has been seen how the distributions narrow as the pressure increases due to the reducing disorder. The same thing is observed in fig. 5-17, where distances tend to occupy one progressively smaller area. Finally, at 26 GPa, there is an interesting effect: the distribution of distances, now restricted to a limited interval, now arrange according to the vertices of a square: the atoms corresponding to the top-left and bottom-right vertices are paired showing an alternation between long distance and short distance, while those along the other two vertices correspond to the succession of two long distances or two short distances. This particular distribution of the distances in fig. 5-17 at 26 GPa point out a local structure like those observed in Peierls' instabilities (see app. A) characterized by a dimerization of atoms chains. However, XRD experiments do not show any phase transition: this means that this instability is limited to a few unit cells, leaving the cubic structure of the system unchanged.

In summary, this XAFS experiment on Nb_3Sn revealed a greater disorder of the Nb-Nb distances of the first and third shells, with a discontinuity around 7 GPa. This result, product of a preliminary analysis in which the distribution of the distances was assumed to be Gaussian, suggested to study in more detail the characteristics of the Nb-Nb bonds. The analysis with the RMC method, made it possible to clarify the results of the preliminary analysis. In particular this analysis method allowed to find that a Peierls instability is induced on Nb_3Sn by appling a pressure and that the pressure anomaly observed with the high pressure XRD experiment of the previous chapter has to be likely related to the Peierls-like dimerization of Nb chains.

Chapter 6

DFT based first-principles calculations

Density Functional Theory (DFT) is a theory of correlated many-body systems. Over the past few decades, DFT has been the most successful, widely used method in condensed-matter physics, computational physics and quantum chemistry to describe properties of condensed matter systems, which include not only standard bulk materials but also complex materials such as molecules, proteins, interfaces and nanoparticles [130].

DFT is a way of studying a system of interacting particles by mapping it to a much easier to solve non interacting problem. In doing this, the main idea of DFT is to describe a many-body interacting system via its particle density and not via its many-body wave function. This means that the computational cost of a DFT calculation is relatively low when compared to traditional methods, such as the Hartree-Fock theory, that deal directly with the many-body wave function. This difference is based on the fact that a many-body wave function is a function of $3N$ variables (the coordinates of all N atoms in the system) while the electron density, used in DFT, is a function of only the three spatial variables. The result of this is that traditional multiparticle wave function methods when applied to systems of many particles encounter the so-called exponential wall when the number of atoms N exceeds a critical value which currently is in the neighborhood of $N_0 \approx 10$. On the other hand, the current state of the art of applied DFT can handle systems with up to $N_0 = 10^2$-10^3 atoms [130].

To understand the exponential wall above cited, imagine the wave function of a N_2 molecule, having two nuclei and fourteen electrons. For N particles, the Schrödinger equation is a partial differential equation in $3N$ dimensions. If one wishes to express the wave function on a grid with about 100 points along each spatial direction, and considering two spin states for each electron, the resulting wave function is represented by $2^{14}100^{3\times16} \approx 10^{100}$ complex numbers.
The Nb_3Sn system is described by 2 Sn atoms and 6 Nb atoms per unit cell, with 13 valence electrons for each Nb atom and 14 for each Sn atom. Given the above considerations, it's clear that DFT is necessary if one wants to calculate the properties of Nb_3Sn from first-principles.

In this thesis some methods based on DFT have been exploited to investigate the properties of Nb_3Sn as a function of a high hydrostatic pressure. In particular, the *ab-initio* calculated lattice parameter of cubic Nb_3Sn as a function of pressure has been used as input for the calculations of the phonon dispersion curves and the electronic band structures along different high symmetry directions in the Brillouin zone. The critical temperature, then, has been calculated as a function of an hydrostatic pressure by means of the Allen-Dynes modification of the McMillan formula defined by equations (1.15) and (1.16).

In the next section an overview of the principles of DFT and its perturbative extension Density Functional Perturbation Theory (DFPT) will be given. Then the calculations made during this thesis work will be described together with the results obtained, first focusing the attention on the ambient pressure results and then extending the discussion to the high pressure results.

6.1 Notes on Density Functional Theory

The entire field of modern DFT rests on two fundamental mathematical theorems proved by W. Kohn and P. Hohenberg in 1964 [130–132]. These theorems are stated as follows:

- *Theorem I*: The ground state density $n(\mathbf{r})$ of a bound system of interacting electrons in some external potential $V(\mathbf{r})$ determines this potential uniquely, except for an additive constant.
  Hence $n(\mathbf{r})$ fully determines the hamiltonian of the system and it determines implicitly the many-body wave function for all states through the solution of the appropriate Schrödinger equation. This means that all the properties of a system are completely determined once the ground state density $n(\mathbf{r})$ is defined. This result is important because it means that it is possible to solve the Schrödinger equation by finding a function of three spatial variables, i. e. the electron density, rather than a function of $3N$ variables (where N is the number of electrons), i. e. the wave function.

- *Theorem II*: A functional for the energy $E[n]$ in terms of the electron density $n(\mathbf{r})$ can be defined, valid for any external potential $V(\mathbf{r})$. For any $V(\mathbf{r})$, the ground state energy of the system is the global minimum value of this functional, and the density $n(\mathbf{r})$ that minimizes the functional is the ground state density $n_0(\mathbf{r})$.

The functional for the total energy can be written as [132]:

$$\begin{aligned} E_{HK}\left[n\right] =& T\left[n\right] + E_{ee}\left[n\right] + \int d^3 r V\left(\mathbf{r}\right) n\left(\mathbf{r}\right) + E_{NN} = \\ & F_{HK}\left[n\right] + \int d^3 r V\left(\mathbf{r}\right) n\left(\mathbf{r}\right) + E_{NN} \end{aligned} \tag{6.1}$$

where the terms on the center are, in order, the electron kinetic energies, the interaction between electrons, the interactions between electrons and the external potential (included that due to the presence of the nuclei) and the interaction between the positive nuclei. $F_{HK}[n]$ contains the functional for the kinetic energy, $T[n]$, and that for the electron-electron interaction, $E_{ee}[n]$. The latter can be written as follows:

$$E_{ee}[n] = \frac{1}{2}\int d^3r d^3r' \frac{n(\mathbf{r})\, n(\mathbf{r}')}{|\mathbf{r}-\mathbf{r}'|} + E_{XC}[n] = E_H[n] + E_{XC}[n], \tag{6.2}$$

where $E_H[n]$ is the Hartree functional, that describe the Coulomb interaction between electrons, and $E_{XC}[n]$ is the exchange-correlation energy, that include all the quantum mechanical effect of the electron-electron interaction.

The main problem of DFT, as stated by Hohenberg and Kohn, is to provide an expression for the functionals $T[n]$ and $E_{XC}[n]$.

A solution to the lack of accurate approximations for the kinetic energy functional $T[n]$ is given in the work of W. Kohn and L. J. Sham, appeared in 1965 [133]. In the Kohn and Sham approach one assumes that the ground state electron density of the interacting system is equal to that of some chosen non-interacting reference system. This means that the task of finding the right electron density for a system can be expressed in a way that involves solving a set of equations in which each equation only involves a single electron. Following the Kohn and Sham assumption, the Hohenberg-Kohn ground state energy functional can be rewritten as:

$$E_{KS}[n] = T_s[n] + \int d^3r V(\mathbf{r})\, n(\mathbf{r}) + E_H[n] + E_{XC}[n] + E_{NN}, \tag{6.3}$$

where $T_s[n]$ is the independent-particle kinetic energy expressed as a function of the single electron wave functions. In this expression of the energy functional the only term for which no explicit form can be given is $E_{XC}[n]$. In order to minimize $E_{KS}[n]$, the variational principle together with the ortonormality condition for the orbitals are applied. The resulting equations are the self-consistent Kohn-Sham equations:

$$\left[\frac{\hbar^2}{2m}\nabla^2 + V(\mathbf{r}) + V_H(\mathbf{r}) + V_{XC}(\mathbf{r})\right]\psi_i(\mathbf{r}) = \varepsilon_i \psi_i(\mathbf{r}), \tag{6.4}$$

where $V(\mathbf{r})$ is potential that defines the interaction between an electron and the collection of atomic nuclei, $V_H(\mathbf{r})$ describes the Coulomb repulsion between the electron being considered in one of the Kohn-Sham equations and the total electron density defined by all electrons in the problem and $V_{XC}\left(\mathbf{r}\right)$ defines exchange and correlation contributions to the single-electron equations. The resulting elctron density is given by:

$$n\left(\mathbf{r}\right)=\sum_{i=1}^{N}\left|\psi_i\left(\mathbf{r}\right)\right|^2. \tag{6.5}$$

The results of Kohn, Hohenberg, and Sham showed that the ground state of a system of interacting electrons can be found by minimizing the energy functional, and that this can be achieved by finding a self-consistent solution to a set of single-particle equations. However, there is still an issue: to solve the Kohn-Sham equations the exchange-correlation function, $E_{XC}\left[n\right]$, has to be determined. In fact, the true form of the exchange-correlation functional whose existence is guaranteed by the Hohenberg-Kohn theorem is not known, except for the case of a uniform electron gas in which the electron density is constant at all points in space. This situation is very different from that of any real material since it is variations in electron density that define chemical bonds and generally make materials interesting for their properties. However, it is possible to obtain approximate forms for $E_{XC}\left[n\right]$ from the model of the uniform electron gas.

The simplest approximation for $E_{XC}\left[n\right]$ is the so-called *Local-Density Approximation* (LDA) [132], in which the exchange-correlation potential at each position is the known exchange-correlation potential for a uniform electron gas at the electron density observed at that position.

The best known class of functional after the LDA uses information about the local electron density and the local gradient in the electron density; this approach defines a *Generalized Gradient Approximation* (GGA) [132]. Because there are many ways in which information from the gradient of the electron density can be included in a GGA functional, there are a large number of distinct GGA functionals. One of the most widely used functionals in calculations involving solids is the Perdew-Wang functional (PW91) [134], that is also used for the calculations of this thesis work.

Formally DFT only provides the ground state density and total energy, and there are well known failures in the representation of electronic excited states [135]. If however the ground state is perturbed very lightly, so leaving the system close to its electronic ground state, one can easily apply the traditional quantum formalism for perturbation theory, giving density functional perturbation theory (DFPT). The first development of DFPT came from Baroni, Giannozzi, and Testa in Trieste [136]. A large number of electronic structure simulation packages now implement and use DFPT. The most commonly used are QUANTUM ESPRESSO [137] and ABINIT [138], but also VASP [139], octopus [140], CASTEP [141] and many others. DFPT has become one of the most popular methods of ab-initio calculation of lattice dynamics [142]. However, the applicability of the method extends beyond the study of vibrational properties. Many interesting physical properties (response functions) are the result of the application of an external perturbation to a system under investigation. Response functions are second, third, or higher order derivatives of the total energy with respect to applied perturbation(s). Typical perturbations can be atomic displacements, homogeneous external electric or magnetic fields, strain or chemical change. Linear response provides an analytical way of computing the second derivative of the total energy with respect to a given perturbation. Depending on the nature of this perturbation, a number of properties can be calculated. A perturbation in ionic positions gives the dynamical matrix and phonons; in magnetic field - NMR response; in unit cell vectors - elastic constants; in an electric field - dielectric response, etc.

DFPT starts from the assumption of the adiabatic approximation of Born and Oppenheimer [142] according to which the kinetic energy of the nuclei is supposed to be constant. The Born-Oppenheimer Hamiltonian H_{BO} depends parametrically upon the nuclear positions $\mathbf{R}$ and describes the problem of the interacting electrons moving in the electrostatic field of nuclei at fixed positions:

$$H_{BO} = -\frac{\hbar^2}{2m}\sum_i \frac{\partial^2}{\partial \mathbf{r}_i^2} + \frac{e^2}{2}\sum_{i\neq j}\frac{1}{|\mathbf{r}_i - \mathbf{r}_j|} - \sum_{i,I}\frac{Z_I e^2}{|\mathbf{r}_i - \mathbf{R}_I|} + \frac{e^2}{2}\sum_{I\neq J}\frac{Z_I Z_J}{|\mathbf{R}_I - \mathbf{R}_J|} \tag{6.6}$$

where $\mathbf{r}$ are the electronic coordinates, (i,j) and (I,J) letters respectively label electron and nuclei, and Z is the nuclear charge. In H_{BO} the first term is the kinetic energy of the electrons and the other terms are the various electrostatic interaction terms (the repulsive electron-electron, the attactive electron-nucleus, and the repulsive nucleus-nucleus). The ground state Born-Oppenheimer energy of the system described by H_{BO} is $E_{BO}(\mathbf{R})$. It determines the *Potential Energy Surface* and the equilibrium geometry of the system. By adding to H_{BO} the kinetic energy of the nuclei, the Schrödinger equation for the nuclear motion, which determines the dynamics of the lattice of the system, is obtained:

$$\left(-\sum_I \frac{\hbar^2}{2M_I}\frac{\partial^2}{\partial \mathbf{R}_I^2} + E_{BO}(\mathbf{R})\right) = \varepsilon\Phi(\mathbf{R}) \tag{6.7}$$

where ε is the total energy and M_I are the masses of the atoms.

Consider a three-dimensional crystal, with N unit cells, translational vectors $\mathbf{l}_n$ (that identify the position of a unit cell with respect to an origin) and a basis of atoms in the positions $\mathbf{b}_\nu$. Atoms are labeled by the two indices $(n\nu)$, where the index n denotes the unit cell of the crystal and the index ν the atoms inside the unit cell. The nuclei are not fixed to their classical zero-temperature ideal positions but perform small displacements $\mathbf{u}_{n\nu}$ around their equilibrium positions $R_{n\nu}$, such that $\mathbf{u}_{n\nu} = R_{n\nu} - (\mathbf{l}_n + \mathbf{b}_\nu)$. If all the $\mathbf{u}_{n\nu}$ are small, then the Born-Oppenheimer energy of the crystal can be expanded in a Taylor series as a function of the nuclear displacements in the harmonic approximation:

$$E_{BO}(\{\mathbf{u}_{n\nu}\}) = E_{BO}(0) + \sum_{n\nu\alpha}\sum_{n'\nu'\alpha'}\left(\frac{\partial^2 E_{BO}}{\partial \mathbf{u}_{n\nu\alpha}\partial \mathbf{u}_{n'\nu'\alpha'}}\right)_0 \mathbf{u}_{n\nu\alpha}\mathbf{u}_{n'\nu'\alpha'} \tag{6.8}$$

where $E_{BO}(0)$ is the minimum of the energy in the static approximation, when all the displacements are zero, $\alpha, \alpha' = x, y, z$, $\nu, \nu' = 1, 2, ...n_b$ and $n = 1, 2, ..N$. The first order term in the series represents the forces acting on each nucleus, which vanish at the equilibrium when E_{BO} reaches a minimum. Hence the linear contribution in the expansion disappears. Anharmonic effects are described by higher order terms in Eq. (6.8). The matrix of the second derivatives of $E_{BO}(\{\mathbf{u}_{n\nu}\})$ evaluated at the equilibrium configuration:

$$D_{n\nu\alpha,n'\nu'\alpha'} = \left(\frac{\partial^2 E_{BO}}{\partial \mathbf{u}_{n\nu\alpha} \partial \mathbf{u}_{n'\nu'\alpha'}} \right)_0 \tag{6.9}$$

is called the *matrix of the interatomic force constants* (IFC) and from the definition in Eq. (6.9) is real and symmetric.

The classical equations of motion for the nuclei are:

$$M_\nu \frac{d^2 \mathbf{u}_{n\nu\alpha}}{dt^2} = - \sum_{n'\nu'\alpha'} D_{n\nu\alpha,n'\nu'\alpha'} \mathbf{u}_{n'\nu'\alpha'}. \tag{6.10}$$

Assuming that the $\mathbf{u}_{n\nu\alpha}$ undergo a time evolution in the form of a plane wave:

$$\mathbf{u}_{n\nu}(t) = \mathbf{A}_\nu(\mathbf{q}, \omega) e^{i(\mathbf{q}\cdot\mathbf{l}_n - \omega t)} \tag{6.11}$$

and replacing (6.11) in (6.10) it results:

$$- M_\nu \omega^2 A_{\nu\alpha} = - \sum_{n'\nu'\alpha'} D_{n\nu\alpha,n'\nu'\alpha'} e^{-i\mathbf{q}\cdot(\mathbf{l}_n - \mathbf{l}_{n'})} A_{\nu'\alpha'} \tag{6.12}$$

The solutions of (6.12) are the vibrational frequencies ω that are determined by the eigenvalues of the Hessian of E_{BO}:

$$\det \left| D_{\nu\alpha,\nu'\alpha'}(\mathbf{q}) - M_\nu \omega^2 \delta_{\alpha\alpha'} \delta_{\nu\nu'} \right| = 0 \tag{6.13}$$

where

$$D_{\nu\alpha,\nu'\alpha'}(\mathbf{q}) = \sum_{n'} D_{n\nu\alpha,n'\nu'\alpha'} e^{-i\mathbf{q}\cdot(\mathbf{l}_n - \mathbf{l}_{n'})}. \tag{6.14}$$

The matrix $D(\mathbf{q})$, with elements $D_{\nu\alpha,\nu'\alpha'}(\mathbf{q})$ is the *dynamical matrix* of the crystal in reciprocal space.

So, the calculation of the equilibrium geometry and of the vibrational properties of a system amounts to computing the first and second derivatives of its Born-Oppenheimer energy surface.

There are two approaches that allow to get these energy derivatives: one based on the *finite differences* and another based on the Hellmann-Feynman theorem [143, 144] (or "force theorem"). The Hellmann-Feynman theorem states that the first derivative of the eigenvalues of a Hamiltonian, H_λ , that depends on a parameter λ is given by the expectation value of the derivative of the Hamiltonian:

$$\frac{\partial E_\lambda}{\partial \lambda} = \left\langle \Psi_\lambda \left| \frac{\partial H_\lambda}{\partial \lambda} \right| \Psi_\lambda \right\rangle, \tag{6.15}$$

where Ψ_λ is the eigenfunction of H_λ corresponding to the eigenvalue E_λ. In the context here, nuclear coordinates act as parameters in the electronic Hamiltonian (6.6). By applying the Hellmann-Feynman theorem, the force acting on the νth nucleus in the electronic ground state is thus:

$$\mathbf{F}_\nu = -\frac{\partial E_{BO}(\mathbf{R})}{\partial \mathbf{R}_\nu} = -\left\langle \Psi(\mathbf{r}, \mathbf{R}) \left| \frac{\partial H_{BO}(\mathbf{R})}{\partial \mathbf{R}_\nu} \right| \Psi(\mathbf{r}, \mathbf{R}) \right\rangle, \tag{6.16}$$

where $\Psi(\mathbf{r}, \mathbf{R})$ is the electronic ground state wave function of the Born-Oppenheimer Hamiltonian. H_{BO} depends on $\mathbf{R}$ via the electron-ion and ion-ion interaction. The Hellmann-Feynman theorem states in this case that:

$$\mathbf{F}_\nu = -\int n_{\mathbf{R}}(\mathbf{r}) \frac{\partial V_{\mathbf{R}}(\mathbf{r})}{\partial \mathbf{R}_\nu} d\mathbf{r} - \frac{\partial V_N(\mathbf{R})}{\partial \mathbf{R}_\nu} \tag{6.17}$$

where $V_{\mathbf{R}}(\mathbf{r})$ is the electron-nucleus interaction (third term in (6.6)), $V_N(\mathbf{R})$ is the electrostatic interaction between different nuclei (fourth term in Eq. (6.6)) and $n_{\mathbf{R}}(\mathbf{r})$ is the ground state electron charge density corresponding to the nuclear configuration R. The Hessian of the Born-Oppenheimer energy surface appearing in Eq. (6.9) obtained by differentiating the Hellmann-Feynman forces with respect to nuclear coordinates,

$$\begin{aligned} \frac{\partial^2 E_{BO}(\mathbf{R})}{\partial \mathbf{R}_\nu \partial \mathbf{R}_{\nu'}} = -\frac{\partial \mathbf{F}_\nu}{\partial \mathbf{R}_{\nu'}} = & \\ \int \frac{\partial n_{\mathbf{R}}(\mathbf{r})}{\partial \mathbf{R}}_{\nu'} \frac{\partial V_{\mathbf{R}}(\mathbf{r})}{\partial \mathbf{R}}_{\nu} d\mathbf{r} + \int n_{\mathbf{R}}(\mathbf{r}) \frac{\partial^2 V_{\mathbf{R}}(\mathbf{r})}{\partial \mathbf{R}_\nu \partial \mathbf{R}_{\nu'}} d\mathbf{r} + \frac{\partial^2 V_N(\mathbf{R})}{\partial \mathbf{R}_\nu \partial \mathbf{R}_{\nu'}}. \end{aligned} \tag{6.18}$$

Equation (6.18) states that the calculation of the Hessian of the Born-Oppenheimer energy surfaces requires the calculation of the ground state electron charge density $n_{\mathbf{R}}(\mathbf{r})$ as well as of its linear response to a distortion of the nuclear geometry, $\dfrac{\partial n_{\mathbf{R}}(\mathbf{r})}{\partial \mathbf{R}_\nu}$. This fundamental result was first stated in the late 1960s by De Cicco and Johnson (1969) and by Pick, Cohen, and Martin (1970).

This result makes it possible to derive the vibrational properties of the materials within the DFT framework and it is the fouding ground for part of the results reported in the following.

6.2 Details of Calculations on Nb_3Sn

DFT and DFPT as implemented in the Quantum ESPRESSO (QE) software distribution [137] have been used to perform the band structure and phonon dispersion relations calculations on Nb_3Sn. The DFT scheme employed adopts a Generalized Gradient Approximation (GGA) of the electron exchange and correlation energy using the Perdew-Wang formula (PW91) [134]. Electron-ion interactions have been modelled with ultrasoft pseudopotentials (US-PP) in the context of a plane wave expansion basis set. Pseudopotentials replace the strong Coulomb potential of the nucleus and the effect of the tightly bound core electrons by an effective ionic potential acting on the valence electrons. The ultrasoft pseudopotentials in particular allow to create pseudofunctions that are as smooth as possible, remaining accurate and transferable (a pseudopotential generated in an atomic calculation should be adequate for non atomic calculations, i.e. molecules or solids). With the word "smooth", here one refers to the fact that they are accurate and transferable without extending too far in the Fourier space. In this thesis work the pseudopotentials Nb.pw91-nsp-van.UPF and Sn.pw91-n- van.UPF from the Quantum ESPRESSO pseudopotential data base: http://www.quantum-espresso.org/pseudopotentials have been used.

All the calculations presented in this thesis have been performed on the CRESCO cluster (ENEA, Frascati, Italy).

6.2.1 Convergence tests

The ground state electron density of the system in the DFT framework is defined by the solution to the Kohn-Sham equations. To solve this problem on a computer a series of numerical approximations must be done: for example, integrals in multi-dimensional space must be evaluated by examining the function to be integrated at a finite collection of points or solutions that formally are expressed as infinite sums must be truncated to finite sums, and so on. In each numerical approximation, it is possible to find a solution that is closer and closer to the exact solution by using more and more computational resources. A calculation is said to "converge" when the computed solution accurately approximates the true solution of the mathematical problem posed by DFT with a specific exchange-correlation functional. For this reason, before starting any ab-initio study it is necessary to calculate some parameters that guarantee the convergence of the calculations that must be made to determine the desired properties of the material.

In the following the different convergence tests carried out in the work phase dedicated to setting up the calculations are discussed.

The first convergence test done is devoted to examine the calculations convergence with respect to the Brillouin zone (BZ) sampling. In order to do this, Self Consistent Field (SCF) calculations of the system total energy with different quantities of k-point grids in the reciprocal space were carried out. The method used for the generation of the k points in the BZ follows the convention of Monkhorst and Pack [145], where the k points are distributed in a rectangular grid of dimensions $M_x \times M_y \times M_z$, evenly spaced throughout the BZ. The calculation has been done for a 4×4×4, 8×8×8, 12×12×12 and 16×16×16 k-point grids ($M_x = M_y = M_z = M$ because the system is cubic). The computed total energy as function of M, is shown in fig. 6-1-left, where it is clear that when $M \geq 8$ the total energy is fairly independent of the number of k points. For this reason a 8×8×8 Monkhorst-Pack k-point grid for the BZ sampling has been employed for the simple cubic cell of Nb_3Sn. This means that for this system the integrals in reciprocal space were evaluated at least in 8×8×8=516 points of

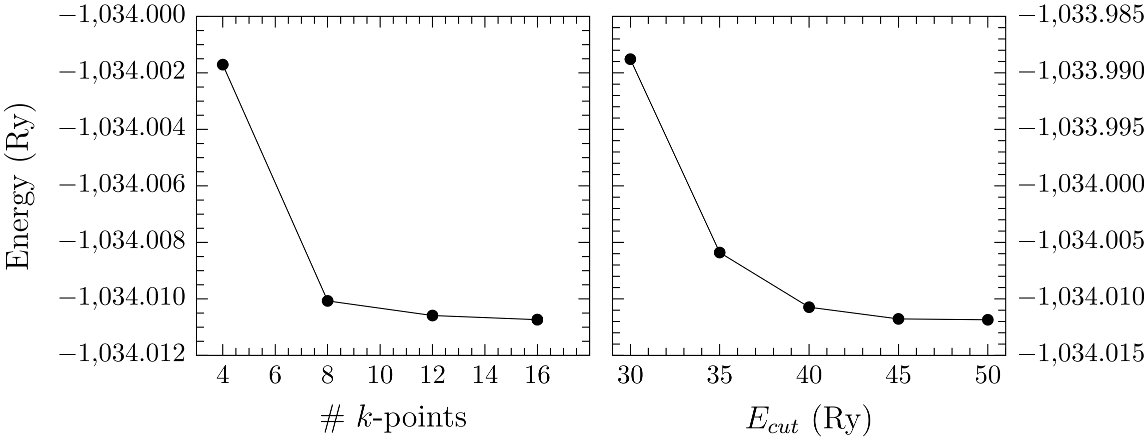

Figure 6-1: Total energies for Nb_3Sn calculated as a function of the k-point grid (left) and of the cut-off energy (right).

the BZ in order to obtain well convergent computation. However, when the crystal symmetries are taken into account the integrals in reciprocal space do not need to be evaluated using the entire BZ, but they can just be evaluated in a reduced portion of the BZ, the irreducible Brillouin zone (IBZ), that can then be extended without approximation to fill the entire BZ using symmetry. In the present case using the IBZ greatly reduces the computational effort required to perform integrals in k-space: indeed, for the 8×8×8 sampling of the BZ, only 126 distinct points in k space lie within the IBZ. Within the Monkhorst-Pack method the k points are determined by means of the relation:

$$\mathbf{k}_{m_1,m_2,m_3} = \sum_{i=1}^{3} \frac{2m_i - M_i - 1}{2M_i} \mathbf{b}_i, \tag{6.19}$$

where M_i is the number of k points in each direction, $m_i = 1, ..., M_i$ and $\mathbf{b}_i$ are the primitive vectors of the reciprocal lattice.

The second convergence test done is devoted to examine the calculations convergence with respect to the kinetic energy. Nb_3Sn has a periodical structure, then the solution of the Kohn-Sham equations must satisfy the Bloch's theorem, which states that the solution can be expressed as (*plane wave* expansion basis set) [146]:

$$\phi_{\mathbf{k}}(\mathbf{r}) = e^{i\mathbf{k}\cdot\mathbf{r}} u_{\mathbf{k}}(\mathbf{r}), \tag{6.20}$$

where $u_{\mathbf{k}}(\mathbf{r})$ is periodic with the same periodicity of the lattice. This means that it can be expanded in terms of a special set of plane waves:

$$u_{\mathbf{k}}(\mathbf{r}) = \sum_{\mathbf{G}} c_{\mathbf{G}} e^{i\mathbf{G}\cdot\mathbf{r}}, \tag{6.21}$$

where the summation is over all reciprocal lattice vectors $\mathbf{G}$. According to this expression, evaluating the solution of the Kohn and Sham equations in k-space involves a summation over an infinite number of possible values of $\mathbf{G}$. Solutions of the form of Eq. (6.20) correspond to states with kinetic energy:

$$E_c = \frac{\hbar^2}{2m}|\mathbf{k} + \mathbf{G}|^2. \tag{6.22}$$

In k-space the coefficient $u_{\mathbf{k}}(\mathbf{r})$, are obtained by the Fourier tranform of (6.21): these decrease exponentially with the kinetic energy of Eq. (6.22). As a result, the infinite sum above is approximated by including only solutions with kinetic energies below a cut-off energy E_{cut}. In order to obtain the appropriate value of E_{cut} for calculations on Nb_3Sn, Self Consistent Field (SCF) calculations of the system total energy with different values of E_{cut} were carried out. The computed total energy as function of E_{cut}, is shown in fig. 6-1-right, where it is clear that an energy cut-off of 40 Ry is sufficient in order to obtain well convergent calculations.

Next, being Nb_3Sn a metallic system, the electronic occupation at the Fermi level is a step, which makes integration and the use of plane-waves very difficult. By allowing k points to be partially occupied through smearing, a smaller number of k points yields an accurate band structure. The smearing method used for this thesis work is the Marzari-Vanderbilt smearing [147]. The smearing width *degauss* has been calculated by means of SCF calculations at different values of the variable *degauss*. It resulted that convergence is achieved for $degauss = 0.065$ Ry.

6.2.2 Computation scheme

The ground state configurations of a Nb_3Sn unit cell at different values of pressure, starting from ambient pressure to 50 GPa, have been obtained via the quasi-Newton Broyden-Fletcher-Goldfarb-Shanno (BFGS) algorithm [148]. With this algorithm, the ground state configuration is obtained by searching the minimum of the potential energy surface that is closest to the starting configuration given as input. The searched configuration corresponds to that for which the forces as defined by the Hellmann-Feynman theorem (see Eq. (6.16)) are zero. The algorithm begins at an initial estimate for the optimal configuration and proceeds iteratively to get a better estimate at each stage, as described in [148].

This variable-cell calculation has been done with the variable *cell_dofree*=x, y, z, that allows only variations on the length of the lattice parameter along the three axes.

The lattice parameter obtained from the BFGS variable-cell relaxation at each value of pressure has been given as input for the SCF calculations, from which the ground state energy and Kohn-Sham eigenfunctions are computed. The band structure calculation at each pressure is then calculated using the QE executable *band.x* along the high- symmetry directions of the simple-cubic BZ of Nb_3Sn, represented in fig. 6-2. The coordinates of the symmetry points are (0, 0, 0), (1, 0, 0), (1, 1, 0), (1, 1, 1), for Γ, X, M, and R, respectively.

Then, a non-SCF calculation has been made and its results have been processed for the electronic density of states (e-DoS) calculation at each pressure by means of the *dos.x* executable.

For the determination of phonon curves and phonon-related quantities as the electron-phonon coupling introduced with the Eliashberg theory, the PHonon package, part of the QE distribution, has been used. In particular the dynamical matrices in reciprocal space have been calculated by means of the *ph.x* executable where a 2×2×2 q-point uniform grid, previously tested to be sufficient for convergence, has been employed. After the interatomic force constants (IFC) in real space have been calculated with the *q2r.x* executable that takes as input the dynamical matrices produced by

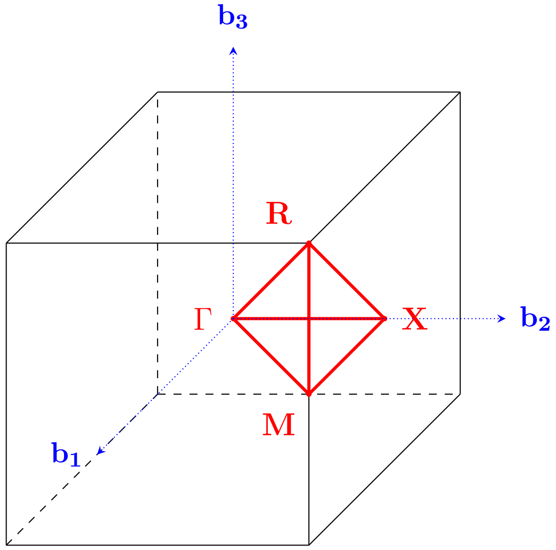

Figure 6-2: The first Brillouin zone for A15 structures.

ph.x. The next step, perfomed with the *matdyn.x* executable, was the calculation of the phonon frequencies, the phonon DoS and the electron-phonon coupling, using the IFC files calculated by *q2r.x*. A denser k-mesh of 24×24×24 was used in order to obtain accurate estimations of the electron-phonon (el-ph) coupling constant λ at each given pressure. Finally, the critical temperature T_c at each pressure value has been determined by means of the *lambda.x* executable that uses the Allen-Dynes modification of the McMillan formula (see chap. 1). Here, the Coulomb coefficient μ^* has been calculated at each pressure with the formula (1.12) and given as input for the calculations.

6.3 Results of the calculations

6.3.1 Ambient pressure

The BFGS structural optimization of the Nb_3Sn cell provides a value for the lattice parameter $a = 5.309$ Å at ambient pressure, in agreement with the previous result of 5.31 Å obtained by calculation based on the same method [110]. Also this value is in fair agreement with the experimental value of 5.291 Å [91].

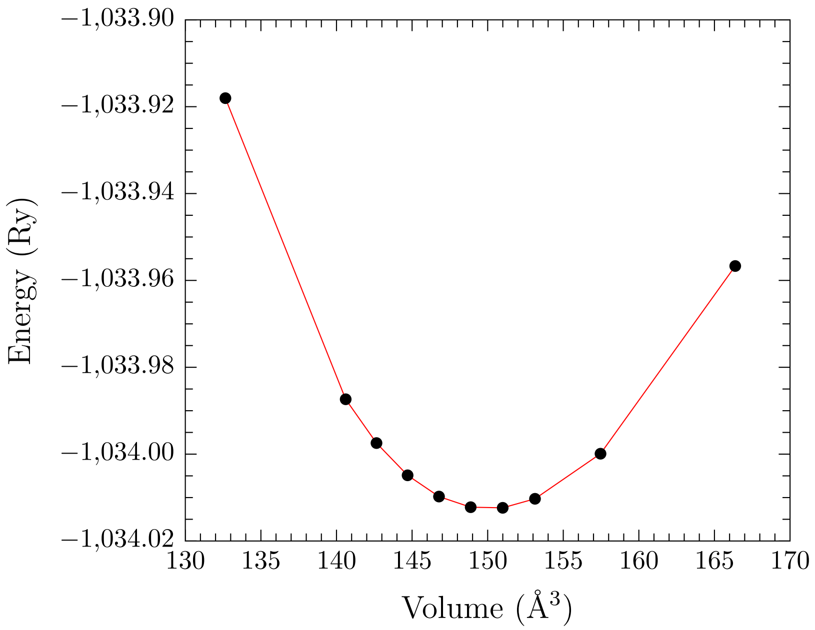

Figure 6-3: Total energy of Nb_3Sn in the simple cubic crystal structure as a function of the volume, V. The curve shows the fit of the DFT data.

Also, in order to obtain the bulk modulus and its derivative at ambient pressure, SCF calculations at many values of the lattice parameter have been done. The total energy as function of the volume is shown in fig. 6-3. The obtained points were fitted to a the Murnaghan equation of state:

$$E(V) = E_0 + V\left(\frac{K_0}{K_0'}\right)\left[\left(\frac{V_0}{V}^{\frac{K_0'}{K_0'-1}}\right) + 1\right] - \frac{K_0 V_0}{K_0' - 1}, \tag{6.23}$$

where E_0 is the minimum energy, V_0 is the volume at the atmospheric pressure and K_0 and K_0' are the bulk modulus and its pressure derivative respectively. The obtained values of the ground state lattice parameter (corresponding to the minimum of the parabola in fig. 6-3), the bulk modulus and its pressure derivative are reported in table 6.1 together with literature results.

The calculated electronic band structure and density of states of Nb_3Sn at atmospheric pressure are shown in fig. 6-4. In figure 6-4, the Fermi level is marked by a dashed horizontal line and is set to 0 eV. E_F falls close to a sharp peak in the electronic DoS, with a value for the density of states of about 20 states eV^{-1} . This

Table 6.1: The lattice parameter, bulk modulus and its derivative and the critical temperature T_c calculated at ambient pressure. Also literature values are reported, from ref. [110, 149, 150]

		a (Å)	K_0 (GPa)	K_0'	T_c (K)
this work	BFGS vc-relax	5.308			
	Murnaghan fit	5.316	161.6 GPa	4.11	
	Allen-Dynes T_c				17.992
literature	experimental	5.29	154; 160		18.3
	DFT-DFPT	5.31	161	4.15	20.7

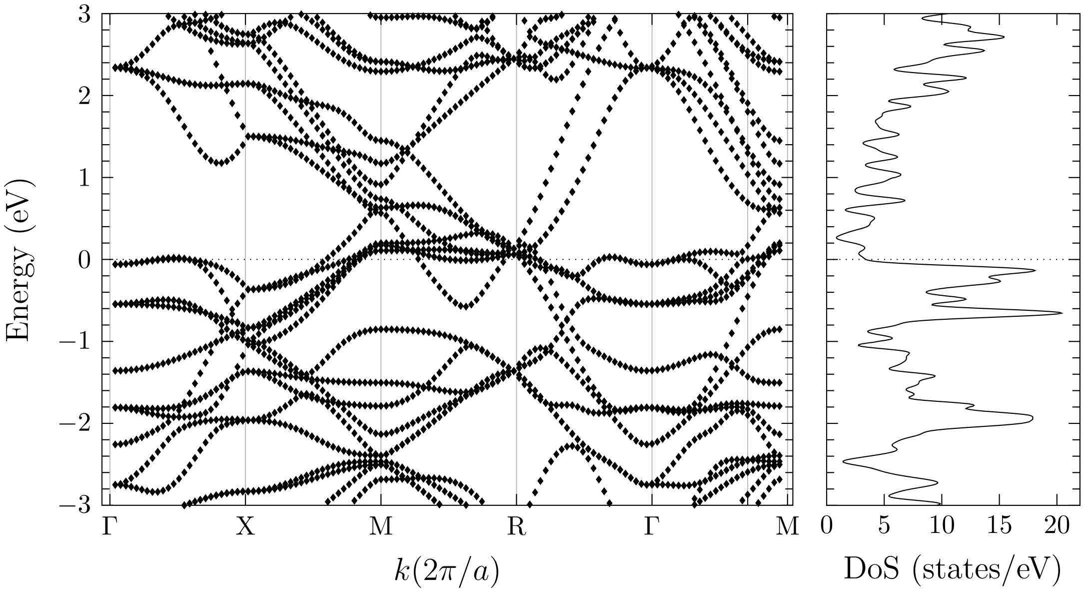

Figure 6-4: The electronic band structure and density of states of Nb_3Sn calculated at atmospheric pressure. The Fermi level is set to 0 eV (dashed orizontal line).

peak is generated by several nearly dispersionless bands crossing the Fermi level in the Γ-M, Γ-R and M-R directions and deriving from the 4d states of Nb atoms. The computed band structure and density of state is in agreement with those previously reported [110].

The calculated phonon dispersion curves at ambient pressure are presented in fig. 6-5. The calculated transverse acoustic (TA) branches show good agreement with literature experimental measurements [59].

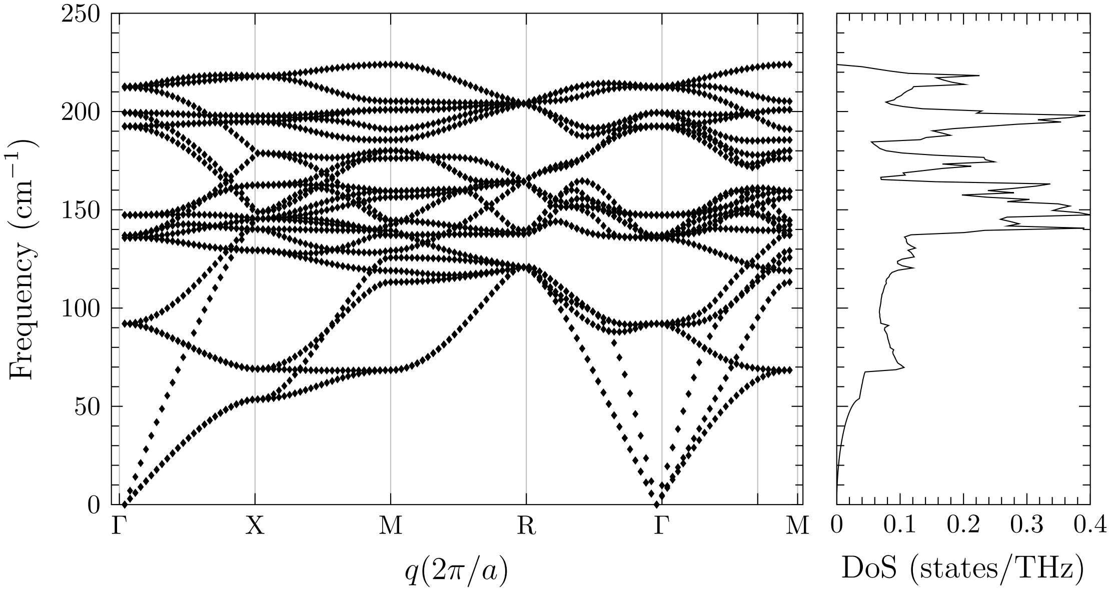

Figure 6-5: Phonon dispersion and density of states for Nb_3Sn at ambient pressure.

The critical temperature, calculated with the Allen-Dynes modification to the McMillan formula is reported also in table 6.1, where it is possible to observe the good agreement with experimental literature values. Instead greater values of T_c were reported from previous DFT-DFPT calculations, with a value of 20.3 K for a *degauss* smearing width of 0.1 Ry. The result of this work is closer to the experimental value for the reported T_c=18.3 K of the stoichiometric Nb_3Sn, and is calculated using a very small Fermi level smearing (*degauss*=0.005).

6.3.2 High pressure

Fig. 6-6 shows the calculated volumes up to 50 GPa together with the XRD results (run 1). The calculated P-V curve has been fitted to the Rydberg-Vinet Equation of State (EoS) [109] for isotropic compression:

$$P(V) = 3K_0 x^{\left(-\frac{2}{3}\right)} \left(1 - x^{\frac{1}{3}}\right) \times \exp\left[\frac{3}{2}\left(K_0' - 1\right)\left(1 - x^{\frac{1}{3}}\right)\right] \tag{6.24}$$

where $x = V/V_0$, V_0 is the volume at the atmospheric pressure and K_0 and K_0' are the bulk modulus and its pressure derivative respectively. The values obtained from

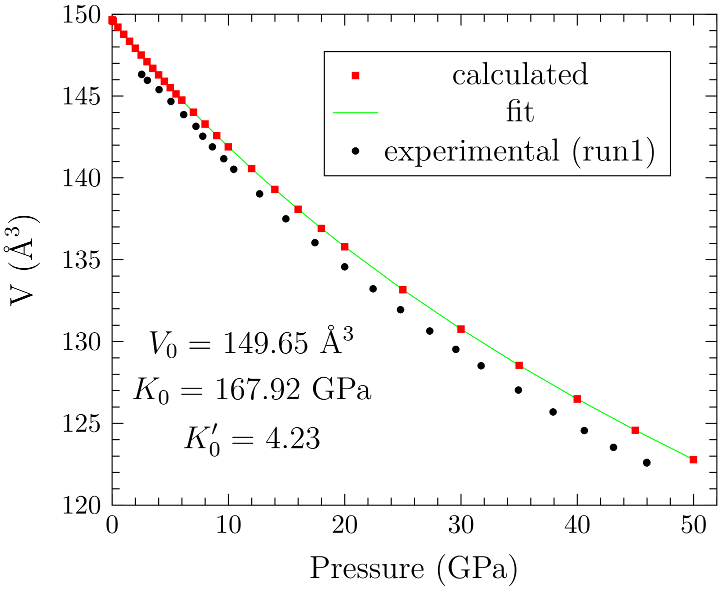

Figure 6-6: Calculated volume of Nb_3Sn as a function of pressure, compared with XRD data.

Table 6.2: The values of the volume, bulk modulus and its first derivative at ambient pressure obtained from the Rydberg-Vinet fit of volumes computed by BFGS variable-cell relaxation at different pressure.

	V_0 (Å^3)	K_0 (GPa)	K'_0
ab-initio	149.65	167.92	4.23
run 1 XRD	147.80 ± 0.03	171 ± 4	4 ± 1
run 2 XRD	148.7 ± 0.1	169 ± 4	3.4 ± 2

the fit are reported in table 6.2, along with the values determined with the XRD experiments of this thesis. The calculations slightly overestimate the volume values ($\Delta V \sim 1.5$ Å^3). These discrepancies might originate from the pseudopotential used for the calculations: several authors observed that GGA may overestimate the volume for 4d and 5d metals [151]. However, the difference between calculated and experimental V_0 falls into the uncertainty of measurement: indeed, by comparing the two runs results it is clear that V_0 varies about 1 Å^3. Moreover, the other parameters, K_0 and K'_0 are consistent within the reported measurement errors.

The obtained lattice parameters have been used as inputs for the calculations of both the phonon dispersion curves and electronic band structures along several high-

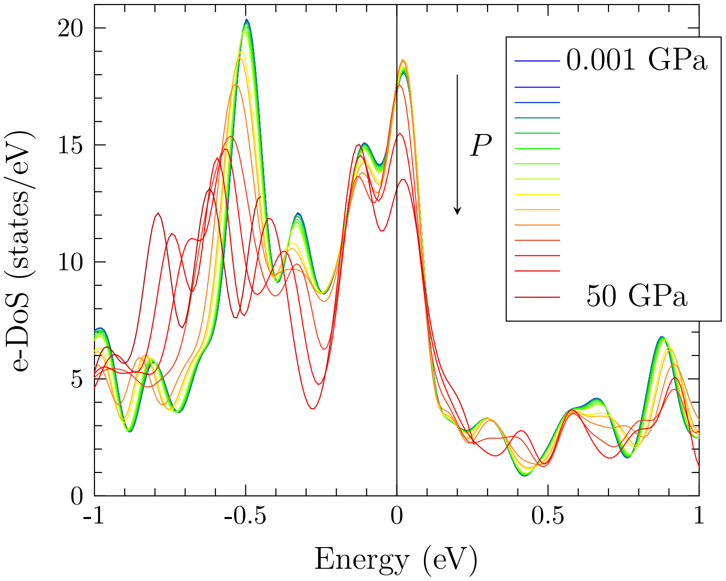

Figure 6-7: Electronic density of states of Nb_3Sn near the Fermi level at different values of pressure.

symmetry directions in the Brillouin zone. Also the Electron Density of States (e-DoS) for different values of pressure has been computed: this is plotted in fig. 6-7. It is clear that the e-DoS at the Fermi level N_{E_F} decreases as pressure increases. Thus, squeezing the cell negatively affects N_{E_F}. This quantity has particular relevance to evaluate T_c: indeed it is proportional to the electron-phonon coupling parameter λ which appears in the Allen-Dynes modification of the McMillan formula for T_c (see formulas (1.15) (1.16)).

In fig. 6-8, the ω_{ln} quantity that appers in the definition of the e-p coupling parameter of Eq. (1.16) is reported as a function of pressure: The plot shows the commonly expected lattice hardening with increasing pressure. However, some instabilities are present at low pressures. Here it is worth to stress that the structure of the system at all the pressure values has been determined by keeping the system cubic and the atoms fixed in their positions in the cell. This means that the relaxation of the structure has only affected the length of the lattice parameter, without change in the relative position of the atoms. As EXAFS experiments pointed out, at low pressure a dimerization of the Nb chains is present, and this has been also detected with XRD experiments as a compressibility anomaly. So the calculated instabilities can origi-

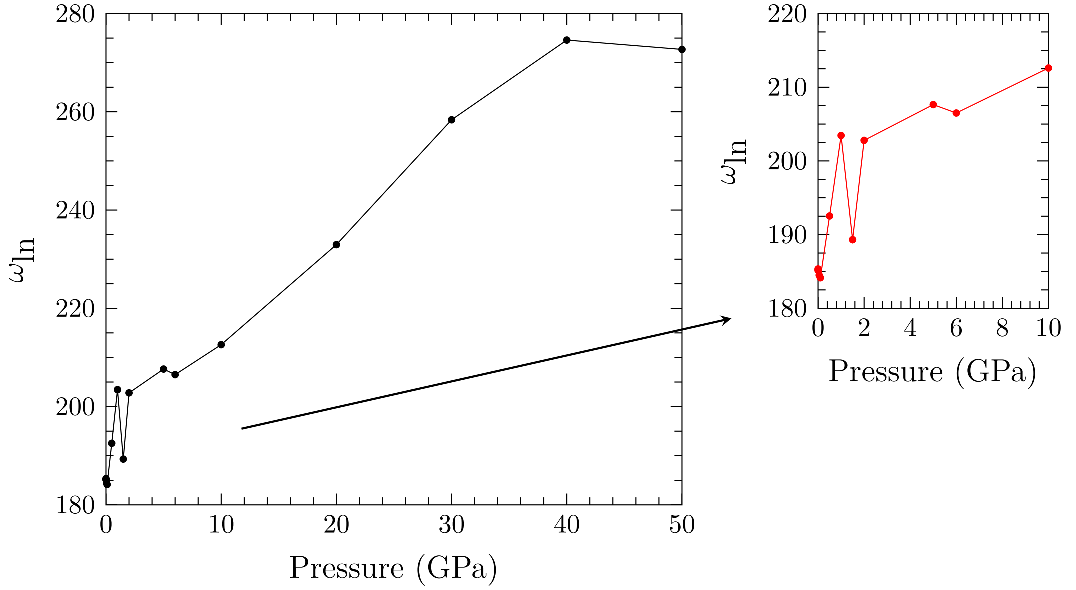

Figure 6-8: ω_{ln} as a function of hydrostatic pressure. In the inset a zoom at low pressure is shown.

nate from neglecting the possibility of atomic displacements in the model. However, they are a clear sign that at low pressures these computations are able to capture the presence of an anomalous structural behavior.

In fig. 6-9, a plot of T_c as a function of pressure is reported. Above 10 GPa, calculations show that T_c decreases linearly with pressure at a rate of -1.5 K GPa^{-1}, in agreement with the value of -1.4 K GPa^{-1} reported in literature for a single crystal of Nb_3Sn in the tetragonal phase [86].

Several oscillations are present in T_c at low pressure, in the range 0-6 GPa. The plot contains also T_c calculated by fixing ω_{ln} and $< I^2 >$ or N_{E_F} at their atmospheric pressure values. When the ω_{ln} is fixed, it is evident that the overall behavior of T_c is mainly dictated by electronic contribution, whereas the low pressure instabilities are related to the above described phonon anomalies, therefore must be closely related to lattice stresses and squeezing.

Finally, since HP-XRD experiments have pointed out anomalies in the compressibility of the system, the pressure effects on the elastic constants have been studied. Indeed, from the phonon dispersion curves, one can infer information about the elastic

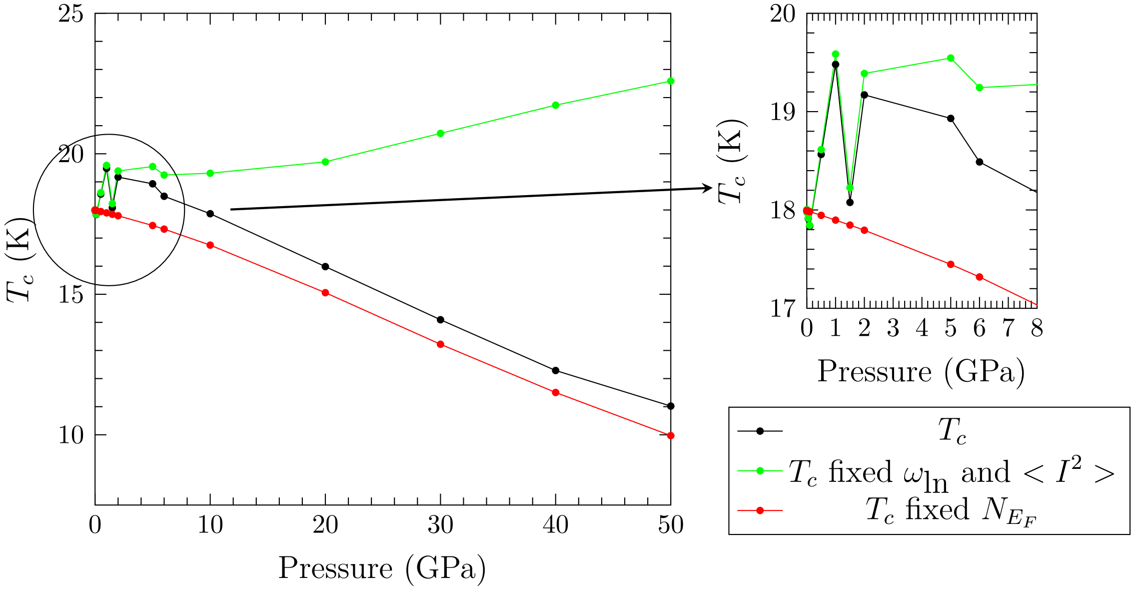

Figure 6-9: The critical temperature T_c calculated as a function of hydrostatic pressure (black line). The electronic and vibrational contributions have been separated by fixing ω_{ln} and $< I^2 >$ (red line) or N_{E_F} (green line) at their atmospheric pressure values.

constants. In fact, in a perfect crystal the elastic constants can be directly obtained from the slopes of the acoustic branches in the long wavelength limit ($|\mathbf{q}| \to 0$). The relation between the sound velocity ν_s along a given direction and the corresponding elastic constant C_{ij} is $C_{ij} = \rho\nu_s^2$, where ρ is the density of the crystal. In particular, for a cubic system, C_{11} and the shear moduli C_{44} and $\frac{1}{2}(C_{11} - C_{12})$ (see appendix B), the following relations hold:

$$C_{11} = \rho \left(\lim_{\xi \to 0} \frac{\partial \nu_{|\xi 00|L}(q)}{\partial |\xi|} a_0 \right)^2 = \rho \nu^2_{s,|\xi 00|L}, \tag{6.25}$$

$$C_{44} = \rho \left(\lim_{\xi \to 0} \frac{\partial \nu_{|\xi 00|T}(q)}{\partial |\xi|} a_0 \right)^2 = \rho \nu^2_{s,|\xi 00|T}, \tag{6.26}$$

$$\frac{1}{2}\left(C_{11} - C_{12}\right) = \rho \left(\lim_{\xi \to 0} \frac{\partial \nu_{|\xi\xi 0|T}(q)}{\partial |\xi|} a_0 \right)^2 = \rho \nu^2_{s,|\xi\xi 0|T}, \tag{6.27}$$

where $\nu_{s,|\xi 00|L}$, $\nu_{s,|\xi 00|T}$ and $\nu_{s,|\xi\xi 0|T}$ are the longitudinal and the transverse velocity of sound in the $[\xi 00]$ direction and the transverse velocity of sound in the $[\xi\xi 0]$ direction, ξ is the phonon wave vector coordinate renormalized by a factor $\frac{a_0}{2\pi}$, a_0 is the lattice

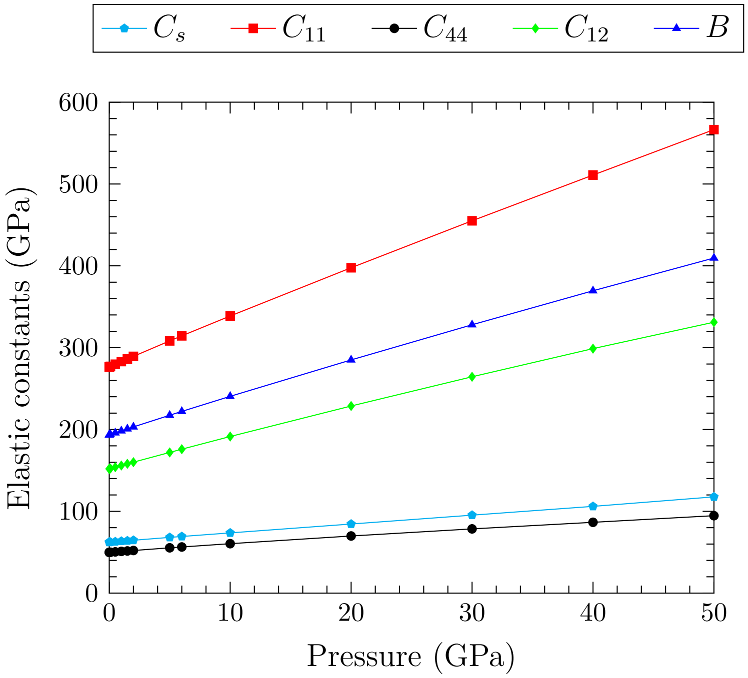

Figure 6-10: The behaviour of the elastic constants in cubic Nb_3Sn as a function of hydrostatic pressure.

parameter of the cubic cell, and ρ is the mass density of the material. The calculated elastic moduli at different pressures are shown in fig. 6-10.

The traditional mechanical stability conditions in cubic crystals on the elastic constants are known as: $C_{11} > 0$, $C_{12} > 0$, $C_{11} - C_{12} > 0$, and $C_{11} + 2C_{12} > 0$ [152]. It is obvious from the plot that all the elastic constants of Nb_3Sn in the pressure range (0-50 GPa) satisfy these traditional stability conditions, meaning that the cubic phase of Nb_3Sn is mechanically stable under pressure up to 50 GPa.

From the plot it is evident that all elastic constants of Nb_3Sn increase almost monotonically with an increase of pressure. The effect of pressure is more pronounced in C_{11} than in C_{44}, as recently pointed out by Reddy *et al.* [10]. Generally, elastic constants C_{11} reflect the stiffness to uniaxial strains along the three spatial directions. So, it can be concluded that Nb_3Sn becomes more and more incompressible with increasing pressure. However, the effect of pressure on shear modulus C_{44} is lighter, which indicates that the resistance to shear deformation of Nb_3Sn increases slower than that to an axial compression with the increase of pressure.

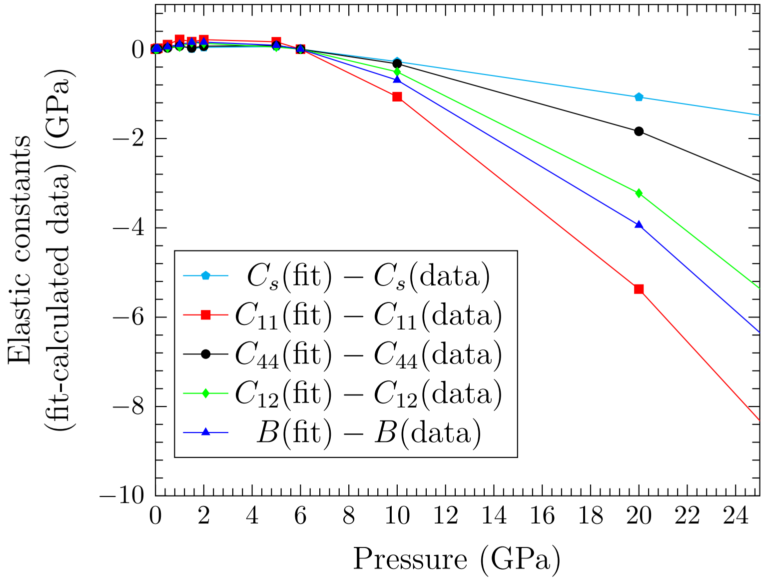

Figure 6-11: The difference between a linear fit at pressure below 6 GPa and the calculated elastic constants.

Moreover, it is possible to observe that all the computed elastic constant at low pressure show a non linear behaviour. To evidence this very small effect linear fits of the different elastic constant curves in the low pressure region (0-6 GPa) have been done. The difference between the fit and the calculated data are reported in fig. 6-11. In particular a change of slope of all the elastic constant is found above 6 GPa.

The behaviour of the elastic constants as function of the pressure obtained in this work is in agreement with that reported by [10], in the fact that both works show an anomalous behaviour of the elastic constants below 10 GPa, also if the change of slope is opposite (see fig. 6-12).

The anomalous behaviour of elastic constants at low pressure is experimentally supported by the HP-XRD experiments of this thesis, where a change in the compressibility of the material has been observed in the same pressure range (see chap. 4).

In this computational work a model for the calculation of the electronic and phonon structure as a function of an applied pressure has been proposed. To our knowledge, this calculation represents the first attempt to compute phonon dispersion curves of Nb_3Sn as a function of pressure. From phonon dispersion curves it

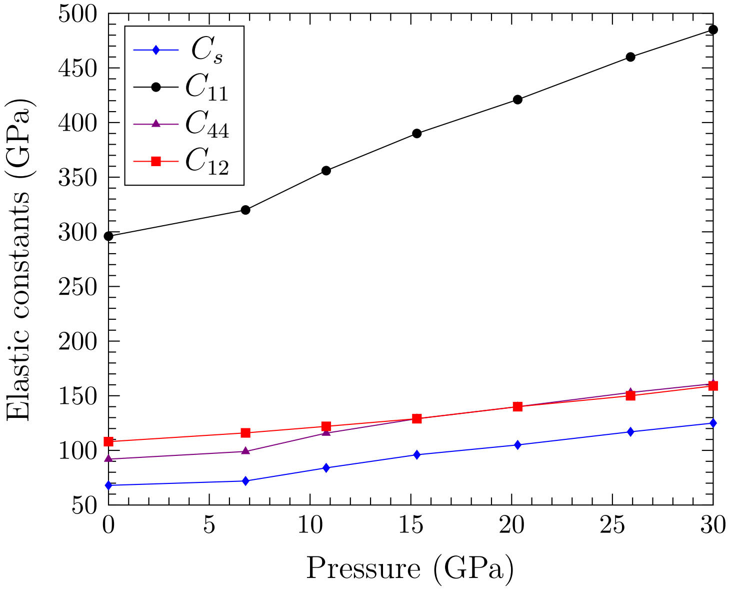

Figure 6-12: The elastic constants calculated by Reddy *et al.* [10]

has been possible to obtain the evolution of the elastic constants with pressure. The behaviour of the elastic constants is in agreement with previous computations by Reddy [10]. Also the evolution of calculated volume versus pressure is consistent with the experimental trend, obtained by HP-XRD measurements in chapter 4.2.2. Finally the T_c versus pressure evolution has the same trend as that obtained experimentally and reported in literature. Except for some oscillations at very low pressures, very likely resulting from computational problems not yet fully understood, a small jump towards lower T_c has been obtained between 5 and 6 GPa, originating from a slight softening of phonon modes at these pressures. The jump on T_c and the elastic constants non linearities occur in the same pressure range here and also in the same region where an anomaly in the compressibility has been observed with HP-XRD experiments.

From the above discussion, with the support of the experimental results of this thesis and so far available in the literature, the results of these computations give confidence on the model proposed as a starting point for further deeper studies.

Chapter 7

Conclusions

Nb_3Sn is the most widely used superconductor for high magnetic field applications. Although it has been known since long time, the effect of an applied stress on its superconducting and structural properties are still not fully understood. The main results obtained in the past have been discussed in chap. 2 and here can be recalled with the following few points: (i) Nb_3Sn is a LTS superconductor with a maximum $T_c = 18.3$ K and high upper critical magnetic field, above 20 T at 4.2 K; (ii) the high critical temperature with respect to the other LTS has been explained to originate from the peculiar arrangement of the Nb atoms that, forming non intersecting and orthogonal chains along the faces of the cubic cell of the material, produces a peak in the electronic density of states at the Fermi level, (iii) this material exhibits a structural phase transformation when cooled below $\sim$40 K that affects negatively the superconducting properties, (iv) the cubic-tetragonal and superconducting transitions are correlated and, when the latter comes before the former, the material does not change its structure; (v) the structural transition has been observed only on quasi-stoichiometric samples without additional impurities, (vi) above the structural transition precursor effects have been observed in all samples independently of its composition and purity, that can lead to the transition or not depending on the material; (vii) an hydrostatic pressure (up to 20 kbar) negatively affects T_c.

Many efforts have been addressed to study the effect of applied axial or transverse stresses on technological wires, but the effects of an hydrostatic load on the material properties have been poorly studied and the few results date back to the seventies [86,87].

Now available diamond anvil cells which allow to reach pressures of hundreds GPa, the nowadays high resolution synchrotron powder diffraction and the XAFS capabilities as a local probe technique, that at the time of most part of investigations reported in literature was only at its first applications and was not applied to this material, have been exploited in this thesis work to study the structural properties of Nb_3Sn as a function of an applied pressure (up to ~ 50 GPa) and as a function of temperature (down to ~ 80 K).
In particular, the PV curve up to ~ 50 GPa has been for the first time determined from diffraction measurements of technological samples. XRD results show a compressibility anomaly at 5-6 GPa, while the crystal structure remains cubic in the entire range of pressures investigated. The anomaly has been evidenced by means of a peak position analysis on only three diffraction peaks as a plateau in the pressure evolution of the position difference between pairs of peaks (fig. 4-8). The more sophisticated analysis based on the Rietveld method allowed also to compare the compressibility of Nb_3Sn to those of Cu and Ta (present in the samples because they have been extracted from technological wires), that are known to not show any structural particular behavior as a function of pressure in the investigated pressure range except for the obviously isotropic compression. The compressibility of Nb_3Sn is seen, from this comparison, to have an anomaly at low pressures (fig. 4-11).
More investigation on the structural properties has been done by means of XAFS spectroscopy, that allowed us to observe the local structure around a Nb atom as a function of pressure. This study has evidenced a pressure induced deviation from a gaussian distribution of the Nb-Nb distances of first shell. The analysis carried out by assuming the commonly used gaussian distribution of distances showed us that Nb-Nb bonds (I and III shells) are characterized by a higher disorder when compared to that of Nb-Sn bond (II shell). Moreover, the pressure evolution of the MSRD of

the I and the III shells showed a discontinuity at about ~ 9 GPa. The more sophisticated analysis based on the Evolutionary-Algorithm Reverse Monte Carlo method showed a bimodal distribution of the first shell distances (fig. 5-16). It has been demonstrated [129] that this effect results from a dimerization of the Nb-Nb chain (fig. 5-17).

Therefore the nature of the anomaly in the compressibility observed with the XRD technique, which allows to study only the average structure of the material, is explained as an anticorrelated displacement of Nb atoms along the chains.

The aim of this thesis has been also to obtain the pressure dependence of the properties of the material by means of first principle calculations. The results at ambient pressure match with the previously obtained results for the electronic band structure and phonon dispersion relations [110]. Instead, the obtained results at high pressure cannot be fully compared with existing works, in particular for the phonon structure that has never been calculated as a function of pressure, as far as we know. However, the results obtained are consistent with the few ones reported in literature [86, 87] and with the experimental data obtained in this thesis work. The P-V plot obtained and the overall trend of T_c are in agreement with the experimental results (fig. 6-6). Instabilities in the phonon dispersion curves result in instabilities of the critical temperature T_c. They could be the signature of some structural effect, and in particular the dimerization of Nb chains that within the proposed model cannot be taken into account. Releasing the constraint of fixed Nb positions could lead to a more accurate model, and eventually to a deeper understanding of the origin of the instabilities and of the observed chain dimerization. This work motivates future calculations that start from the proposed model and allow Nb atomic displacements from their nominal position in the cell.

The presented results at high pressure have been obtained at a time in which the interest towards the high pressure properties of A15 superconductors has turned on, given the recent results on Nb_3Al and Nb_3Ga [7, 8]. These two materials showed a plateau in the $P - V$ curves and this behaviour has been interpreted by means of *ab-initio* calculations to be the effect of an electronic topological transition. At this stage of the study it cannot be affirmed if there is such a transition on Nb_3Sn from our calculations, because they were carried out with the Nb atoms fixed in the cell. In particular with our model we do not obtain such a transition. However, the proposed model is a starting point. The initial choices of keeping the atoms fixed in the cell and leaving only the lattice parameter to vary have been suggested by the computational cost: more parameters to be evaluated correspond to more time consuming computations. The model proposed, however, is successful in the fact that it gives the overall trend of the properties of Nb_3Sn and hints phonon related instabilities in the same pressure range of the detected dimerization chains and compressibility anomaly. The XAFS experiment results, the last work of this thesis, suggested that to address the presence of the phonon instabilities at low pressures could be a matter of allowing the dimerization of Nb chains by adding some free parameters and justifies the need for more time consuming computations.

Part of the results reported in this thesis about the high pressure XRD experiments and first-principles calculations have been published [153] and two posters have been presented at the Applied Superconductivity Conference 2016 (Denver, US) and at the European Conference on Applied Superconductivity 2017 (Geneva, CH).

Finally, low temperature XRD investigations have pointed out new features, not previously observed. In particular, a compressibility variation at ~ 180 K (fig. 4-15), likely to be related to the non-linear behaviour of the elastic modulus C_{44} [12], and a change of slope of the c/a ratio at around 120 K as precursor effect of the tetragonal transition (fig. 4-19), have been detected.

In conclusion, a great effort has been done to understand the structural phase diagram of Nb_3Sn as function of temperature and pressure separately. Going forward, in addition to better understand what has already been seen, to complete the picture it will be appropriate to study what happens when varying simultaneously the temperature and pressure so as to complete the phase-diagram of Nb_3Sn on the T-P plane.

Appendix A

The Peierls distortion in 1D chain

A Peierls instability has been predicted by Rudolf Peierls in 1930 [154, 155] with a theorem that states that a one-dimensional equally spaced chain with one electron per ion is unstable as a regular array and can distort under certain conditions, such as low temperatures. This distortion is manifested as alternating bond distances, an effect called *dimerization*. Peierls predicted that this rearrangement of the ion cores would produce a change of the periodicity of the chain, the opening of a band gap at the Fermi surface of the new unit cell and a redistribution of the charge density, that results having a periodical spatial variation. This periodic fluctuations in the electron density is commonly called charge density wave (CDW).

The mechanism of the Peierls instability can be understood with the following simple model.

Consider an electron system in a potential $V(q)$. The effect of such a potential is to introduce a density modulation $\rho(q) = -\chi(q)V(q)$ [156], where $\chi(q)$ is the polarization function:

$$\chi(q) = \frac{1}{N}\sum_k \frac{f(E_{k+q}) - f(E_k)}{E_k - E_{k+q}}. \tag{A.1}$$

Here E_k and $f(E_k)$ are the band energy and the Fermi distribution function of an electron with wave number k. At temperature $k_BT \ll E_F$ it can be demonstred that,

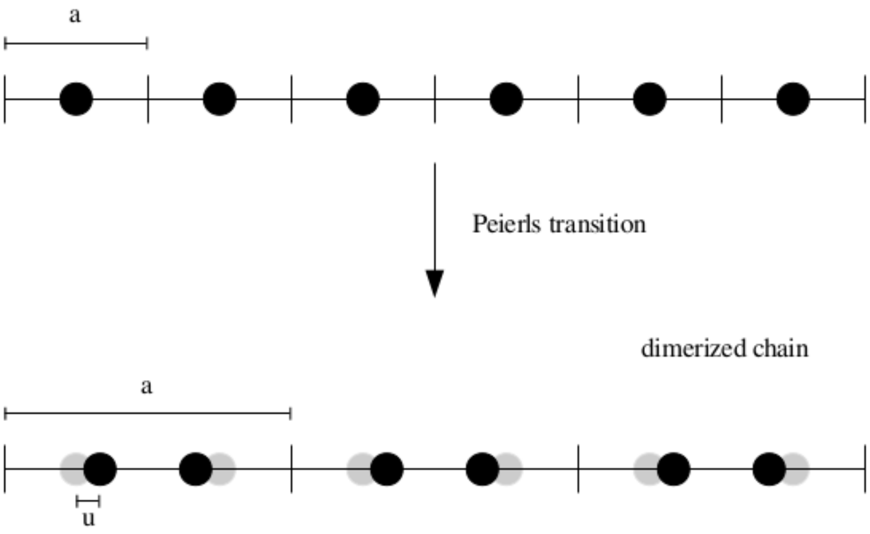

Figure A-1: Up: a linear chain of identical atoms equally spaced; Down: the chain of atoms after the Peierls distortion.

if $q \simeq \pm 2k_F$, $\chi(2k_F)$ has a logaritmic divergence [154]:

$$\chi(2k_F) = \ln\left(\frac{E_F}{k_B T}\right), \tag{A.2}$$

while it has been expected to descrease with increasing the temperature. Thus a 1D electron system becomes unstable at low temperatures in presence of a potential $V(2k_F)$. Then, if the electronic system considered is that of a crystal lattice, also a lattice distortion with period $2k_F$ provides the electron system with the potential $V(2k_F)$.

For simplicity from now on a linear chain of atoms with a regular spacing a (fig. A-1-up) is considered. In the case of one orbital per cell, i.e. if there exist an electronic band partly filled, the band energy obtained by the tight-binding method is expressed by the dispersion relation:

$$E(k) = E_0 + 2\gamma\cos(ka), \tag{A.3}$$

where E_0 and γ are the energy of the isolated atom and the overlap integral that accounts for the interaction between nearest neighbors. The energy curve of Eq. (A.3) is plotted in fig. A-2-left, where also the Fermi wavevector $\mathbf{k_F} = \pi/2a$ of the sytem is shown.

Peierls supposed that in this ideal 1D chain of atoms a lattice distortion can occur, such that every ion moves closer to one neighbor and further away from the other of the some amount **u**, as in fig. A-1-down. This means that the symmetry of the chain is reduced to that of a chain with spacing $2a$. This distortion provides the electron system the potential $V(2k_F)$ which make the system unstable at low temperatures. This rearrangement of the atoms in the chain produce a density modulation with wave number $2k_F$, the so-called CDW.

The doubling of the lattice constant causes a halving of the vectors in reciprocal space, **k**, resulting in a decrease of the size of the Brillouin zone, and hence to a backfolding of bands at the new Brillouin zone boundaries, as depicted in fig. A-2-centre.

At the point where the backfolded bands intersect a band gap opens up. Indeed, by applying the tight-binding method to the dimerized chain the following dispersion curves for the bands are obtained:

$$E(k) = \alpha \pm \sqrt{\gamma_1^2 + \gamma_2^2 + 2\gamma_1\gamma_2 \cos(k2a)}, \tag{A.4}$$

where γ_1 and γ_2 are the new overlap integrals dependent upon the magnitude of **u**.

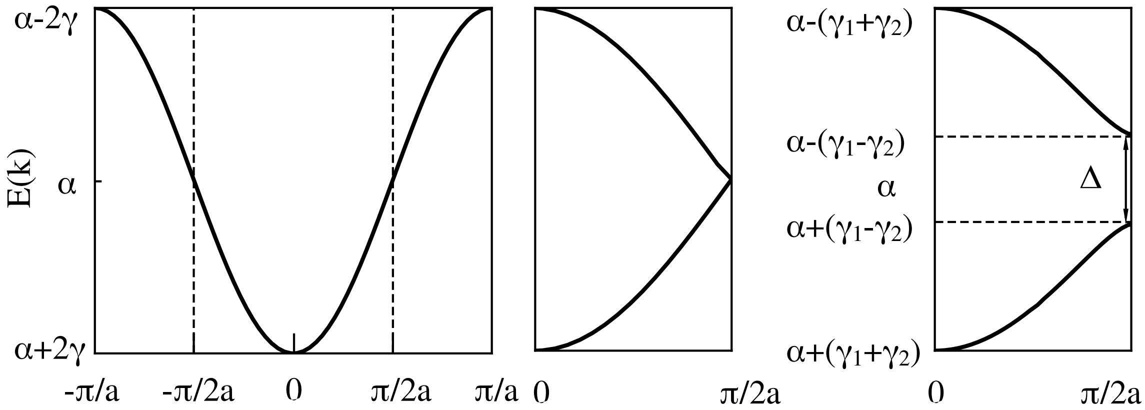

Figure A-2: Electron energy in linear chain. Left: uniform spacing a. Center: uniform spacing $2a$ with two atoms per cell. Right: Dimerized chain.

From (A.4) it results that:

$$E = \alpha \pm (\gamma_1 + \gamma_2) \qquad \text{at} \qquad \mathbf{k} = 0 \qquad \text{and} \tag{A.5}$$

$$E = \alpha \pm (\gamma_1 - \gamma_2) \qquad \text{at} \qquad \mathbf{k} = \frac{\pi}{2\mathbf{a}}. \tag{A.6}$$

At the Fermi level of the original lattice a gap $\Delta = 2(\gamma_2 - \gamma_1)$ opens up as can be seen in fig A-2-right. In this case all states raised by the dimerization are empty, and all states lowered are occupied, so there is evidently a net reduction in electron energy with respect to the original system.

A necessary condition for a Peierls transition to be observed is that the gain in energy produced by the dimerization is greater than the elastic energy of the lattice that opposes to the distortion. In particular the kinetic energy K of the electrons filling the lower band can be expressed as [154]:

$$K \sim -\Delta\chi(2k_F) \tag{A.7}$$

This is proportional to the displacement u, that enters in the overlap integrals γ_1 and γ_2. On the other hand, the lattice energy U should increase due to the distortion u by the amount:

$$U \sim Cu^2, \tag{A.8}$$

where C is the elastic constant of the lattice. When the total energy of the system becomes negative the Peierls transition takes place: this happens at a certain critical temperature T_P corresponding to the logaritmic divergence of $\chi(2k_F)$.

The Peierls distortion due to the opening of a gap on the Fermi surface can cause various phenomena, among which the most common is the metal-insulator transition.When other mechanisms are produced at the Fermi surface there is a competition between the different mechanisms that can give different effects. In the case of the Nb_3Sn, the opening of the Peierls gap subtracts electrons from the Cooper coupling, thus lowering the critical temperature.

Appendix B

Elastic constants

The property of solid materials to deform under the application of an external force and to regain their original shape after the force is removed is referred to as its "elasticity". The external force applied on a specified area is known as *stress*, while the amount of elastic deformation produced is called the *strain*. In this appendix, the mathematics of elastic constants, the quantities that relates stress and strain, is briefly discussed.

Stress, σ, is defined as a force per unit area of a material and then it is measured in Pa. In general there may be unequally applied stresses in all directions, and therefore the stress is a second order tensor with components σ_{ij}, where $i, j = 1, 2, 3$. σ_{ij} is stress acting in the i direction on the plane perpendicular to the j direction. An example is illustrated in fig. B-1. Components of the stress tensor with repeating indices, for example σ_{11}, are denoted as "normal" or "axial" stress while a stress component with different indices is called a "shear" stress.

Strain, ε, is defined as the ratio between the amount of the deformation in one direction and the original length in that direction and then it is a dimensionless quantity. Also ε is a second order tensor with components ε_{ij}.

The stress tensor σ is expressed by the generalized Hooke's law (also called "constitutive relation"):

$$\sigma_{ij} = c_{ijkl}\varepsilon_{kl} \qquad \text{with} \qquad i, j, k, l = 1, 2, 3. \tag{B.1}$$

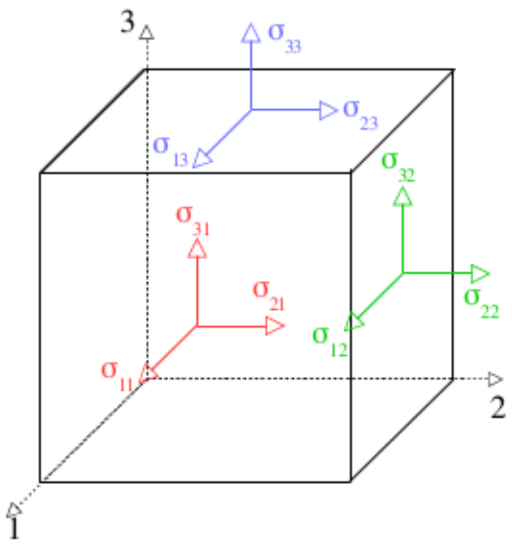

Figure B-1: Stress components acting on the 1,2,3-planes.

The c_{ijkl} are the 81 components of the stiffness tensor C (a fourth order tensor) and are called *elastic constants*. An elastic constant measures the resistance of an object to being elastically strained when a stress is applied to it. As a consequence of the definition of stress and strain an elastic modulus is measured in Pa.

The tensor C has three symmetry properties:

1. from the symmetry of the strain tensor $\varepsilon_{kl} = \varepsilon_{lk}$, it is symmetrical with respect to the last two indices:
$$c_{ijkl} = c_{ijlk} \tag{B.2}$$
2. from the symmetry of the stress tensor $\sigma_{ij} = \sigma_{ji}$, it is symmetrical with respect to the first two indices:
$$c_{ijkl} = c_{jikl} \tag{B.3}$$
3. if the thermodynamic internal energy of the system U is identified with the strain energy, then the elementary strain energy per volume $\sigma_{ij} d\varepsilon_{ij}$ has to be an exact derivative:
$$\frac{\partial \sigma_{ij}}{\partial \varepsilon_{kl}} = \frac{\partial \sigma_{kl}}{\partial \varepsilon_{ij}}. \tag{B.4}$$

By substituting in (B.4) the definition (B.1) one obtain the third symmetry property:

$$c_{ijkl} = c_{klij}. \tag{B.5}$$

Given the two first symmetry properties one has that:

$$c_{ijkl} = c_{jikl} = c_{ijlk}. \tag{B.6}$$

This means that the order of the first two indices (i, j) and the next two indices (k, l) does not affect the elastic constants values. As there are six distinct values for the group (i, j) and six distinct values for the group (k, l), there remain 36 independent elastic constants.
Finally, by applying the third symmetry properties one has also that:

$$c_{ijkl} = c_{klij}. \tag{B.7}$$

This means that the permutation of the (i, j) and (k, l) groups of indices does not modify the elastic constants values. This reduces the number of the independent elastic constants values to 21. Then, a general anisotropic elastic material has 21 elastic constants. This number can be further reduced of an amount that depends on the symmetry of the considered crystal.

In the tensorial equations above written the four indices components of the stiffness tensor appear. To simplify the notation is introduced the so-called Voigt notation which replaces the four indices i, j, k, l with the two indices I, J, according to the rules:

$$I = i \quad \text{for} \quad i = j, \qquad I = 9 - (i + j) \quad \text{for} \quad i \neq j \quad \text{and} \tag{B.8}$$

$$J = k \quad \text{for} \quad k = l, \qquad J = 9 - (k + l) \quad \text{for} \quad k \neq l \tag{B.9}$$

Elastic moduli of a cubic system

In a cubic system the number of the independent elastic constants is reduced to 3 due the symmetry of the system since in this case the three spatial directions are equivalent. They are:

- $c_{11}(=c_{22}=c_{33})$: constant for axial compression, that is when one pushes on one face and the displacement is in the same direction as the force. For a cubic crystal this mudulus is clearly the same in all the three spatial directions. In these cases, for example, a stress σ_{11} results in a strain ε_{11} along the same axis, as depicted in fig. B-2-left;

- $c_{12}(=c_{13}=c_{23})$: constant for dilatation on compression, that is when one push/pull the cube in the i direction and the cube bulges/contacts in the j and k direction. Clearly, the amount of bulging will be the same in both j and k direction (because it is a cube), and when an identical force is applied along the j or k direction, the other two dimensions will bulge or contract in the same way. One example, depicted in fig. B-2-centre, is when a axial stress σ_{11} results in a strain ε_{22} along the pependicular axis;

- $c_{44}(=c_{55}=c_{66})$: shear constant. They are the same because sheering one plane in a cube is equivalent to sheering an orthogonal plane. In these cases, for example, a stress σ_{23} results in a strain ε_{23} across a face, as depicted in fig. B-2-right.

For single crystals the elastic constants can be related to the three commonly known elastic moduli: the bulk modulus B and the shear moduli μ_1 and μ_2.
The bulk modulus B represents the resistance of an object to be compressed or dilatated of the same amount in the three spatial directions and is given by:

$$B = \frac{c_{11} + 2c_{12}}{3}. \tag{B.10}$$

In this case the deformation that results is a change in volume with the same compression or dilatation as in fig. B-2-left in the three spatial directions.

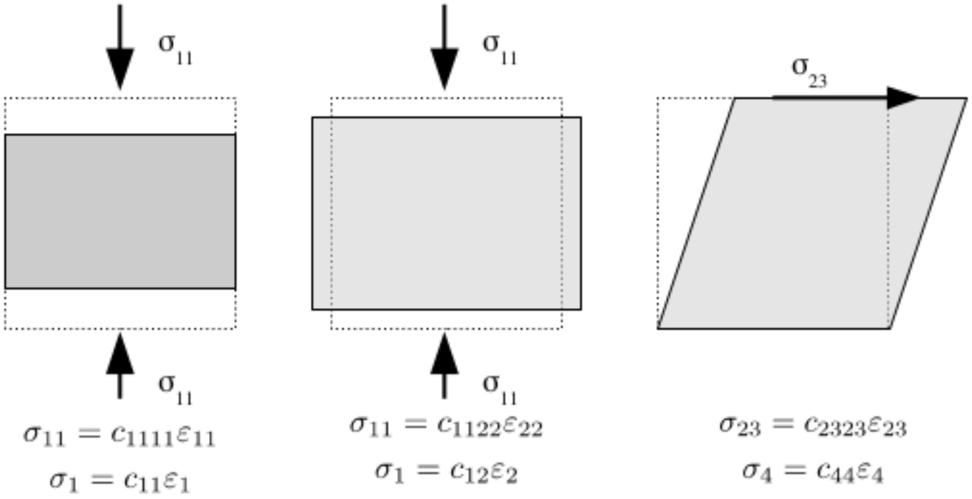

Figure B-2: The scheme of the types of deformation of a cube seen from a face: (left) compression, (center) dilatation on compression, (right)shear deformation. Below each scheme: the constitutive relation written with the four indices notation and with the Voigt notation.

The shear moduli μ_1 and μ_2 are given by:

$$\mu_1 = \frac{c_{11} - c_{12}}{2} \tag{B.11}$$

$$\mu_2 = c_{44}. \tag{B.12}$$

They account for the shear deformations, which does not change the volumes. They refer to the deformations as in fig. B-2-center and right, respectively.

Appendix C

Diamond anvil cell

This appendix surveys the apparatus and methods that have been used to carry out the investigations at high pressure of this thesis work.
High pressure conditions have been generated using the "diamond anvil cell" (DAC).

The DAC was invented in 1959 in the USA [157,158] and it is at present the device that allows to generate the highest static pressure reachable.
The basic principle of a Diamond Anvil Cell (DAC) is very simple. A sample, placed between the flat parallel faces of two opposed gem-quality single crystal diamond anvils, is subjected to a pressure when a force pushes the anvils together (fig. C-1). Since pressure is roughly defined by $P = F/A$, the smaller the area A of the anvil faces, the higher is the pressure P reached by the sample in the DAC for an equivalent value of applied force F. One of the diamond anvils is mounted on the end of a sliding piston, while the other is stationary on a cylinder (see fig. C-2). The pressure in the sample chamber is made hydrostatic, or close to it, by surrounding it with a pressure transmitting medium confined by a gasket. A small pressure gauge is also embedded in the pressure trasmitting medium to allow the measurement of the pressure inside the chamber. As pressure is exerted the gasket deforms plastically and the volume of the cavity becomes smaller increasing in this way the pressure in the experimental chamber. The pressure limit is controlled by the ability of the diamonds, gasket and diamond-backing plates to withstand the applied stresses.

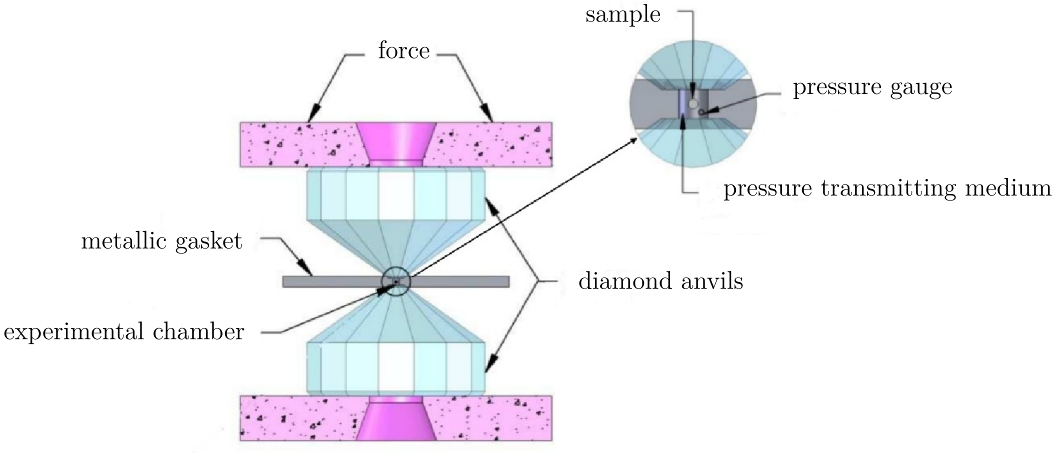

Figure C-1: Opposed diamond anvil configuration, with a metallic gasket for sample confinement in a pressure medium; the basic part of the DAC.

From the above description it is clear that the elements that play the principal roles in experiment performed in a DAC are the diamonds, the gasket and the pressure transmitting media.

Diamond

Diamond anvils are particularly indicated for experiments at high pressures because diamond is the hardest substance known, and transparent to electromagnetic radiation over a wide energy range (infrared, visible, near-ultraviolet (energy $\leqslant 5$ eV and hard X-rays with energy $\geqslant 10$ keV).

Great care must be taken in centering and aligning the two anvils to avoid premature failure of the diamonds at high pressure. The adjustment procedure is made under a microscope: the concentricity is achieved moving the support of the piston diamond slightly to superimpose the two polygons corresponding to the face of the anvils; the parallelism is checked by observing the interference fringes that appear when the two anvils are not parallel. The probe radiation passes through a conical hole drilled in the backing plate. During the pressure increase, the diamond undergoes a very strong elastic deformation (cupping) near the sample region. Due to this deformation, the force transmitted to the sample through the diamond is attenuated and continuing to increase the pressure can lead to the breaking of the diamonds.

Gasket

The use of a gasket for the containment of the pressure transmitting medium was first demonstrated by Van Valkenburg [159]. The gasket, apart from providing containment for the pressure medium, extrudes around the diamonds and acts as a supporting ring, preventing failure of the anvils due to the concentration of stresses at the edge of the anvils faces.

The preparation of the gasket is a key factor for the success of an high pressure experiment.

The gasket is a metallic foil. First of all the selection of the material gasket has to be done. The better choice is a material with a high bulk modulus.

Then, the gasket is pre-indented to a thickness slightly greater than the final thickness, which depends on the maximum pressure that is planned to be applied. The pre-indentation is important to avoid large deformation and instability of the hole, by the matching the gasket to the shape of the anvils culets.

A cavity, the experimental chamber, is then drilled in the center of the gasket and filled with the sample, the pressure gauge and the pressure-transmitting medium. The diameter of the gasket's hole depends on the chosen pressure medium. In case of a solid pressure medium (e.g. NaCl, KCl, KBr), the ideal size is a little bit smaller than half of the diamond culet size. In the case of a very compressible pressure medium (e.g. He, Ne, N_2 , H_2), the hole's diameter should be 3/4 of the total culet's size because the size of the hole dramatically decreases with the pressure rise. In this work, the gasket's holes have been drilled by spark erosion.

Pressure transmitting media

Pressure transmitting media can be liquids (alcohol, alcohol mixture (Methanol - Ethanol 4:1), silicone oil), soft solids (alkali halides), hard solids (MgO, Al_2O_3 , etc) and condensed gases (He, Ne, N_2 , Ar, etc). The adopted transmitting medium must not chemically react with the sample and must not interfere with the measurement of the sample. A fluid pressure transmitting medium supports no shear and transmits an hydrostatic pressure to the sample. With the increasing pressure the transmitting medium solidifies. Beyond this point, shear stresses appear and the pressure across the experimental volume becomes inhomogeneous. Gases, are the best pressure media for room and low temperature experiments. In particular He is considered to be the best pressure-transmitting medium. He is the element with the highest freezing pressure (11.6 GPa at 300 K [160]) and even in its solid phase, it releases stress through recrystallization [161]. In 2001 Takemura [162] reported that good hydrostatic conditions are maintained in solid helium to at least 50 GPa.

There are different ways in which the force-generating and the anvil-alignment mechanisms can be designed. Accordingly, there are different type of DAC. For this thesis work the DAC used are membrane Diamond Anvil Cells.

C.1 Membrane Diamond Anvil Cell

In a membrane DAC the force is transmitted to the piston through a pressure exerted by a gas (see fig. C-2). The idea of transmitting the force by hydraulic way was first suggested by Besson and Pinceaux [160] starting from a piston-cylinder system subsequently replaced by a sealed and deformable membrane filled with He [163].
The thrust mechanism in a membrane DAC is a metallic toroidal membrane that will be inflated with helium supplied by an external bottle, thus exerting a finely tuned pressure on the piston. The applied uniaxial compression is then transformed into an (quasi-) isotropic pressure on the sample via the deformation of the gasket. The applied force is proportional to the pressure in the membrane (see for example fig. C-3. Problems with the cell may be detected from the plot of the pressure measured in the cell as function of the pressure in the membrane. Non-linearities in this plots are a sign of impending trouble, eventually leading to diamond breakage. For this type

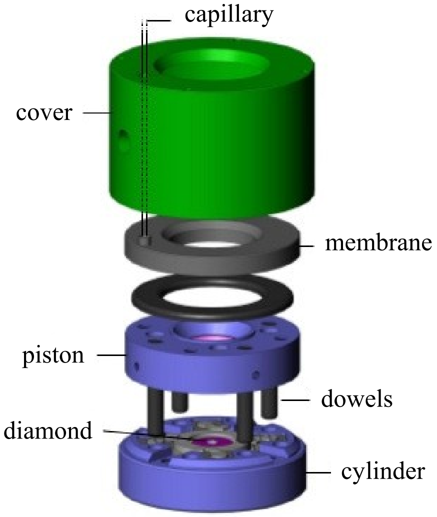

Figure C-2: Schematic representation of the components of a membrane diamond anvil cell. The membrane is filled with helium through a capillary and transmits the force to the piston.

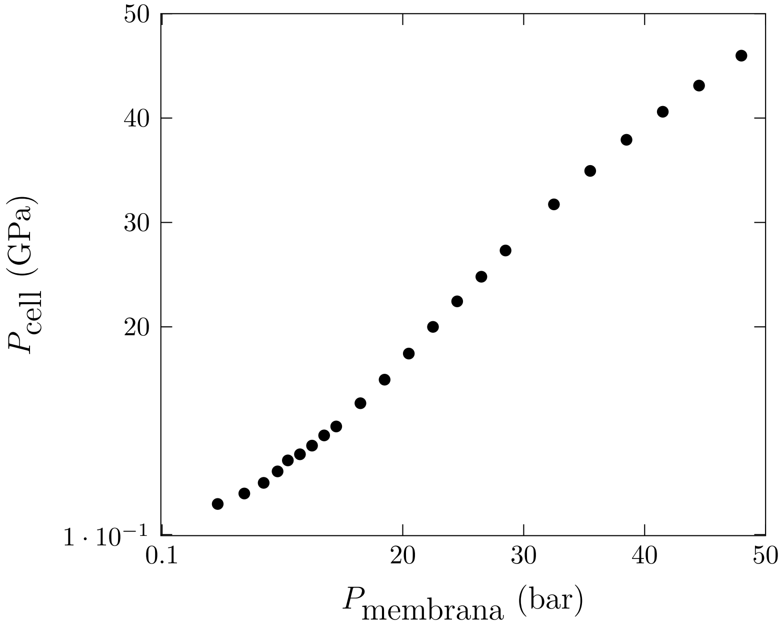

Figure C-3: Plot of the pressure measured in the cell as a function of the pressure in the membrane, in the case of the HP-XRD experiment described in sec. 4.2.2, run2.

of cells, the pressure rise (drop) can be easily tuned by increasing (decreasing) the pressure of the membrane. Moreover, with this type of cell there is the possibility to remotely control the pressure by the means of an automatic pressure driver. In this way, experiments that require the placement of the cell in poorly accessible locations (e.g. experiment in an experimental hutch of a synchrotron) can be easily performed.

C.2 Pressure calibration

To measure the pressure inside the experimental chamber a pressure gauge is also embedded in the pressure trasmitting medium together with the sample. A standard used method is that of the ruby fluorescence method, and it is employed also for this thesis work.

The ruby fluorescence method has been introduced by Forman *et al.* [164] in 1972. In this method a tiny chip of ruby, 5-10 μm in dimension, is placed in the pressure medium along with the sample, and the fluorescence is excited by a He-Cd laser line. The fluorescence signal obtained consists of two lines, R_1 and R_2, with wavelengths 694.14 and 692.7 nm, respectively, at atmospheric pressure. Under pressure these shift to higher wavelengths and the shift is nearly linear with pressure. For the calibration of pressure different model have been constructed. In this thesis the model proposed by Dorogokupets and Oganov [102] is followed. Pressure is obtained from the R_1 line shift of ruby luminescence, in according to the following formula:

$$P = 1884 \left(\frac{\lambda - \lambda_0}{\lambda_0} \right) \left(1 + 5.5 \frac{\lambda - \lambda_0}{\lambda_0} \right), \tag{C.1}$$

where λ_0 is the wavelength of the R_1 fluorescence line of the ruby at room temperature and ambient pressure (694.14 nm). This model represent correctly the $P(\lambda)$ curve in the large pressure range (0-300 GPa) by a single equation and it is consistent with room-temperature isotherms of Al, Au, Cu, Pt, Ta and W, treated often as reference substances.

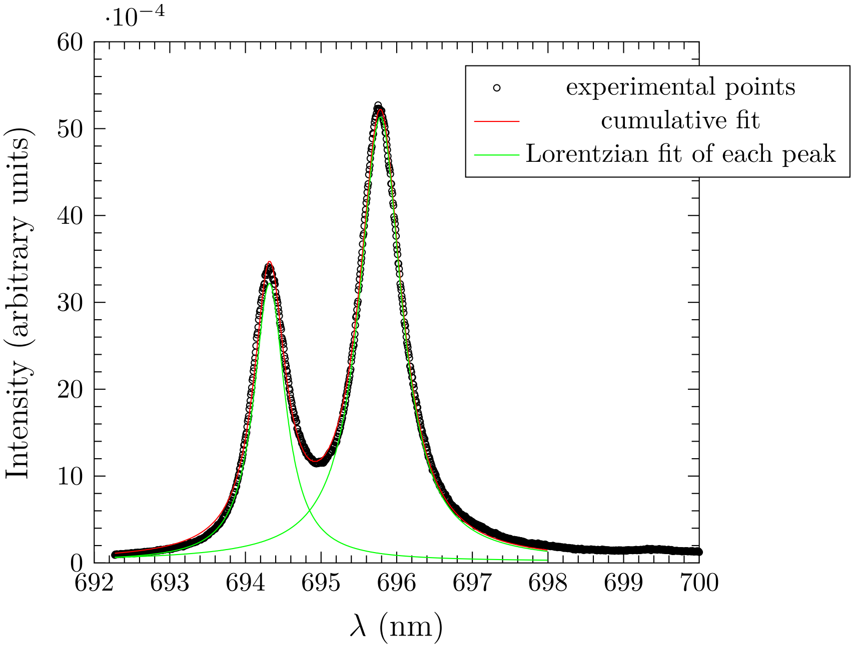

Figure C-4: Plot of the fluorescence signal obtained at pressure 4.77 GPa.

In the experiments of this thesis, the ruby fluorescence signal has been collected every time the pressure was changed and then was fitted with two Lorentzian curves (one for each peak) to obtain the peak position for the two ruby line, R_1 and R_2. An example is in fig. C-4. From fit, the R_1 peak is at 695.87 nm, then applying the Eq. (C.1), the pressure of 4.77 GPa is obtained. This is an example of how all the values of pressure have been evaluated in this thesis.

The determination of the pressure relative to each measurement has been done as follows. The ruby fluorescence signal has been collected before and after each measurement. The pressure values reported in all the analysis refer to the measurements made before each measurement. The relative error has been evaluated as the ratio between half of the difference of the pressure values before and after and is approximately between 1% and 4%.

Bibliography

[1] E. Todesco, M. Annarella, G. Ambrosio, G. Apollinari, A. Ballarino, H. Bajas, M. Bajko, B. Bordini, R. Bossert, L. Bottura, E. Cavanna, D. Cheng, G. Chlachidze, G. De Rijk, J. DiMarco, P. Ferracin, J. Fleiter, M. Guinchard, A. Hafalia, E. Holik, S. Izquierdo Bermudez, F. Lackner, M. Marchevsky, C. Loeffler, A. Nobrega, J. C. Perez, S. Prestemon, E. Ravaioli, L. Rossi, G. Sabbi, T. Salmi, F. Savary, J. Schmalzle, S. Stoynev, T. Strauss, M. Tartaglia, G. Vallone, G. Velev, P. Wanderer, X. Wang, G. Willering, and M. Yu. *IEEE Trans. Appl. Supercond.*, 28(4):4008809, 2018.

[2] Y. Takahashi, Y. Nabara, H. Ozeki, T. Hemmi, Y. Nunoya, T. Isono, K. Matsui, K. Kawano, M. Oshikiri, Y. Uno, F. Tsutsumi, K. Shibutani, T. Kawasaki, K. Okuno, Y. Murakami, M. Tani, G. Sato, Y. Nakata, and M. Sugimoto. *IEEE Trans. Appl. Supercond.*, 24(3):4802404, 2014.

[3] A. Vostner, M. Jewell, I. Pong, N. Sullivan, A. Devred, D. Bessette, G. Bevillard, N. Mitchell, G. Romano, and C. Zhou. *Supercond. Sci. Technol.*, 30(4):045004, 2017.

[4] Miyazaki T., N. Matsukura, T. Miyataka, M. Shimada, K. Takabataka, K. Itoh, T. Kiyoshi, A. Sato, K. Inoue, and H. Wada. Development of Bronze-Processed Nb_3Sn Superconductors for 1GHz NMR Magnets. In U. B. Balachandran, D. G. Gubser, K. T. Hartwig, R. P. Reed, W. H. Warnes, and V. A. Bardos, editors, *Advances in Cryogenic Engineering Materials*, volume 44, page 935. Springer, Boston, MA, 1998.

[5] P. Pugnat and H. J. Schneider-Muntau. *IEEE Trans. Appl. Supercond.*, 24(3):4300106, 2014.

[6] L. Bottura and A. Godeke. *Rev. Accl. Sci. Tech.*, 05:25, 2012.

[7] Z. H. Yu, C. Y. Li, and H. Z. Liu. *Phys. B*, 407(17):3635, 2012.

[8] V. Mkrtcheyan, R. Kumar, J. Baker, A. Connolly, D. Antonio, A. Cornelius, and Y. Zhao. *Phys. B*, 459:21, 2015.

[9] M. Rajagopalan. *Phys. B*, 413(Supplement C):1, 2013.

[10] P. Sreenivasa Reddy, K. Venkatakrishnan, G. Vaitheeswaran, P. Modak, and A. Verma. *J. Appl. Phys.*, 119:075901, 2016.

[11] Z. Ren, L. Gamperle, A. Fete, C. Senatore, and D. Jaccard. *Phys. Rev. B*, 95:184503, 2017.

[12] W. Rehwald, M. Rayl, R. W. Cohen, and G. D. Cody. *Phys. Rev. B*, 6:363, 1972.

[13] H. Kamerlingh Onnes. *Comm. Phys. Lab. Univ.*, 120b, 122b, 124c, 1911.

[14] W. Meissner and R. Ochsenfeld. *Naturwissenschaften*, 21(44):787, 1933.

[15] J. R. Gavaler, M. A. Janocko, and C. K. Jones. *J. Appl. Phys.*, 45(7):3009, 1974.

[16] J. G. Bednorz and K. A. Müller. *Z. Phys. B*, 64(2):189, 1986.

[17] M. K. Wu, J. R. Ashburn, C. J. Torng, P. H. Hor, R. L. Meng, L. Gao, Z. J. Huang, Y. Q. Wang, and C. W. Chu. *Phys. Rev. Lett.*, 58:908, 1987.

[18] J. Nagamatsu, N. Nakagawa, T. Muranaka, Y. Zenitani, and J. Akimitsu. *Nature*, 410:63, 2001.

[19] C. H. Pennington and V. A. Stenger. *Rev. Mod. Phys.*, 68:855, 1996.

[20] F. Steglich, J. Aarts, C. D. Bredl, W. Lieke, D. Meschede, W. Franz, and H. Schäfer. *Phys. Rev. Lett.*, 43:1892, 1979.

[21] Y. Kamihara, H. Hiramatsu, M. Hirano, R. Kawamura, H. Yanagi, T. Kamiya, and H. Hosono. *J. Am. Chem. Soc.*, 128(31):10012, 2006.

[22] A. P. Drozdov, M. I. Eremets, I. A. Troyan, V. Ksenofontov, and S. I. Shylin. *Nature*, 525:73, 2015.

[23] X. F. Pan, Y. Feng, G. Yan, L. J. Cui, C. Chen, Y. Zhang, Z. X. Wu, X. H. Liu, P. X. Zhang, Z. M. Bai, Y. Zhao, and L. F. Li. *Supercond. Sci. Technol.*, 29(1):015008, 2016.

[24] A. A. Abrikosov. *Zh. Eksp. Teor. Fiz.*, 32:1442, 1957.

[25] B. T. Matthias, T. H. Geballe, S. Geller, and E. Corenzwit. *Phys. Rev.*, 95:1435, 1954.

[26] S. Posen and D. L. Hall. *Supercond. Sci. Technol.*, 30(3):033004, 2017.

[27] G. Ambrosio. *IEEE Trans. Appl. Supercond.*, 25(3):4002107, 2015.

[28] L. Bottura, G. de Rijk, L. Rossi, and E. Todesco. *IEEE Trans. Appl. Supercond.*, 22:4002008, 2012.

[29] X. Xu. *Supercond. Sci. Technol.*, 30(9):093001, 2017.

[30] M. Marz, G. Goll, W. Goldacker, and R. Lortz. *Phys. Rev. B*, 82:024507, 2010.

[31] A. Godeke. *Supercond. Sci. Technol.*, 19:R68, 2006.

[32] H. Fröhlich. *Phys. Rev.*, 79:845, 1950.

[33] J. Bardeen. *Phys. Rev.*, 79:167, 1950.

[34] E. Maxwell. *Phys. Rev.*, 78:477, 1950.

[35] C. A. Reynolds, B. Serin, W. H. Wright, and L. B. Nesbitt. *Phys. Rev.*, 78:487, 1950.

[36] L. N. Cooper. *Phys. Rev.*, 104:1189, 1956.

[37] M. Tinkham. *Introduction to Superconductivity*. Dover Books on Physics Series. Dover Publications, 1996.

[38] D. J. Scalapino. The Electron-Phonon Interaction and Strong-Coupling Superconductors. In R. D. Parks, editor, *Superconductivity*, page 449. Marcel Dekker, Inc., New York, 1969.

[39] W. L. McMillan. *Phys. Rev.*, 167:331, 1968.

[40] P. B. Allen and R. C. Dynes. *Phys. Rev. B*, 12:905, 1975.

[41] R. Bauer, A. Schmid, P. Pavone, and D. Strauch. *Phys. Rev. B*, 57:11276, 1998.

[42] W. L. McMillan and J. M. Rowell. *Phys. Rev. Lett.*, 14:108, 1965.

[43] S. Y. Savrasov and D. Y. Savrasov. *Phys. Rev. B*, 54:16487, 1996.

[44] E. L. Wolf, John Zasadzinski, G. B. Arnold, D. F. Moore, J. M. Rowell, and M. R. Beasley. *Phys. Rev. B*, 22:1214, 1980.

[45] C. Paduani. *Braz. J. Phys.*, 37:1073, 2007.

[46] J. Kwo and T. H. Geballe. *Phys. Rev. B*, 23:3230, 1981.

[47] K. E. Kihlstrom, R. W. Simon, and S. A. Wolf. *Phys. B+C*, 135(1):198, 1985.

[48] B. M. Klein, L. L. Boyer, and D. A. Papaconstantopoulos. *Phys. Rev. Lett.*, 42:530, 1979.

[49] L. D. Landau. On the Theory of Superconductivity. In D. T. Haar, editor, *Collected Papers of L. D. Landau*, page 546. Pergamon, 1965.

[50] Y. Li and Y. Gao. *Sci. Rep.*, 7:1, 2017.

[51] G. F. Hardy and J. K. Hulm. *Phys. Rev.*, 89:884, 1953.

[52] George F. Hardy and J. K. Hulm. *Phys. Rev.*, 93:1004, 1954.

[53] L. R. Testardi, J. H. Wernick, and W. A. Royer. *Solid State Commun.*, 15(1):1, 1974.

[54] J. P. Charlesworth, I. Macphail, and P. E. Madsen. *J. Mater. Sci.*, 5:580, 1970.

[55] B. W. Batterman and C. S. Barrett. *Phys. Rev.*, 145:296, 1966.

[56] R. Viswanathan, C. T. Wu, H.L. Luo, and G.W. Webb. *Solid State Commun.*, 14(11):1051, 1974.

[57] K. R. Keller and J. J. Hanak. *Phys. Lett.*, 21(3):263, 1966.

[58] R. Mailfert, B. W. Batterman, and J. J. Hanak. *Phys. Lett. A*, 24(6):315, 1967.

[59] G. Shirane and J. D. Axe. *Phys. Rev. B*, 4:2957, 1971.

[60] R. N. Bhatt and W. L. McMillan. *Phys. Rev. B*, 14:1007, 1976.

[61] G. Bilbro and W. L. McMillan. *Phys. Rev. B*, 14:1887, 1976.

[62] L. P. Gor'kov and O. N. Dorokhov. *Solid State Commun.*, 19(11):1107, 1976.

[63] L. P. Gor'kov. *J. Exp. Theor. Phys.*, 38(4):830, 1973.

[64] J. Labbé and J. Friedel. *J. Phys. France*, 27(5-6):303, 1966.

[65] E. Pytte. *Phys. Rev. B*, 4:1094, 1971.

[66] Welch D.O. The Relationship Between the Martensitic Phase Transition and the Superconducting Properties of A15 Compounds. In Reed R. P. Clark A. F., editor, *Adv. Cryog. Eng.*, page 671. Springer, Boston, MA, 1983.

[67] S. Foner and E. J. McNiff. *Solid State Commun.*, 39(9):959, 1981.

[68] L. R. Testardi, T. B. Bateman, W. A. Reed, and V. G. Chirba. *Phys. Rev. Lett.*, 15:250, 1965.

[69] K. R. Keller and J. J. Hanak. *Phys. Rev.*, 154:628, 1967.

[70] S. Schicktanz, R. Kaiser, E. Schneider, and W. Gläser. *Phys. Rev. B*, 22:2386, 1980.

[71] K. Shimizu, H. Ishikawa, D. Takao, T. Yagi, and K. Amaya. *Nature*, 419:597, 2002.

[72] V. V. Struzhkin, M. I. Eremets, W. Gan, H.-k. Mao, and R. J. Hemley. *Science*, 298(5596):1213, 2002.

[73] S. Deemyad and J. S. Schilling. *Phys. Rev. Lett.*, 91:167001, 2003.

[74] N. W. Ashcroft. *Phys. Rev. Lett.*, 21:1748, 1968.

[75] A. P. Drozdov, M. I. Eremets, I. A. Troyan, V. Ksenofontov, and S. I. Shylin. *Nature*, 525:73, 2015.

[76] G. J. Sizoo and H. K. Onnes. *Commun. Phys. Lab. Univ. Leiden.*, 180b:13, 1925.

[77] L. D. Jennings and C. A. Swenson. *Phys. Rev.*, 112:31, 1958.

[78] J. Hatton. *Phys. Rev.*, 103:1167, 1956.

[79] C. W. Chu, T. F. Smith, and W. E. Gardner. *Phys. Rev. Lett.*, 20:198, 1968.

[80] V. I. Makarov and V. G. Bar'yachtar. *J. Exp. Theor. Phys.*, 21:1151, 1965.

[81] J. J. Hamlin. *Phys. C*, 514:59, 2015.

[82] C. W. Chu, P. H. Hor, R. L. Meng, L. Gao, Z. J. Huang, and Y. Q. Wang. *Phys. Rev. Lett.*, 58:405, 1987.

[83] J. V. Ekin. *Cryogenics*, 20:611, 1980.

[84] G. De Marzi, L. Morici, L. Muzzi, A. della Corte, and M. Buongiorno Nardelli. *J. Phys. Condens. Matter*, 25:135702, 2013.

[85] T. F. Smith. *J. Low. Temp. Phys.*, 6:171, 1972.

[86] C. W. Chu and L. J. Vieland. *J. Low. Temp. Phys.*, 17(1-2):25, 1974.

[87] C. W. Chu. *Phys. Rev. Lett.*, 33:1283, 1974.

[88] I. M. Lifshitz. *Sov. Phys. JETP*, 11:1130, 1960.

[89] M. J. Rice. *Phys. Rev. Lett.*, 20:1439, 1968.

[90] L. Muzzi, S. Chiarelli, A. D. Corte, A. Di Zenobio, M. Moroni, A. Rufoloni, A. Vannozzi, E. Salpietro, and A. Vostner. *IEEE Trans. Appl. Supercond.*, 16(2):1253, 2006.

[91] T. Spina. *Proton Irradiation Effects on Nb_3Sn Wires and Thin Platelets in View of High Luminosity LHC Ugrade.* PhD dissertation, University of Geneva, Department of Science, 2015.

[92] R. E. Collin. *Foundation for Microwave Engineering.* McGraw-HillInternational Editions, 2002.

[93] B. W. Hakki and P. D. Coleman. *IEEE Trans. Microw. Theory Tech.*, 8(4):402, 1960.

[94] P. Debye and P. Scherrer. *Nachrichten von der Gesellschaft der Wissenschaften zu Göttingen, Mathematisch-Physikalische Klasse*, 1916:1, 1916.

[95] R. E. Dinnebier and S. J. L. Billinge, editors. *Powder Diffraction.* The Royal Society of Chemistry, 2008.

[96] M. Mezouar, R. Giampaoli, G. Garbarino, I. Kantor, A. Dewaele, G. Weck, S. Boccato, V. Svitlyk, A. D. Rosa, R. Torchio, O. Mathon, O. Hignette, and S. Bauchau. *High Pressure Research*, 37(2):170, 2017.

[97] S. Wang, A. E. Kovalev, A. V. Suslov, and T. Siegrist. *Rev. Sci. Instrum.*, 86(12):123902, 2015.

[98] H. M. Rietveld. *Acta Crystallogr. A*, 22(1):151, 1967.

[99] R. A. Young, P. E. Mackie, and R. B. von Dreele. *J. Appl. Crystallogr.*, 10(4):262, 1977.

[100] M. Basham, J. Filik, M. T. Wharmby, P. C. Y. Chang, B. El Kassaby, M. Gerring, J. Aishima, K. Levik, B. C. A. Pulford, I. Sikharulidze, D. Sneddon, M. Webber, S. S. Dhesi, F. Maccherozzi, O. Svensson, S. Brockhauser, G. Náray, and A. W. Ashton. *J. Synchrotron Radiat.*, 22(3):853, 2015.

[101] `http://www.diamond.ac.uk/Beamlines/Engineering-and-Environment/I15-Extreme/`.

[102] Peter I. Dorogokupets and Artem R. Oganov. *Phys. Rev. B*, 75:024115, 2007.

[103] D. Rasberry, Y. Zhang, C. R. Hubbard, and R. L. McKenzie. *National Institute of Standards and Technology SRM Certificates*, 1989.

[104] S. W. Freiman, N. M. Trahey, R. D. Deslattes, J-L. Staudenmann, L. D. Hudson, A. Henins, J. J. Fillinben, and R.J. Gettins. *National Institute of Standards and Technology SRM Certificates*, 2000.

[105] A.C. Larson and R.B. Von Dreele. *Report LAUR*, 86-789, 2000.

[106] S. Gražulis, A. Daškevič, A. Merkys, D. Chateigner, L. Lutterotti, M. Quirós, N. R. Serebryanaya, P. Moeck, R. T. Downs, and A. Le Bail. *Nucleic Acids Res.*, 40(D1):D420, 2012.

[107] A.C. Larson and R.B. Von Dreele. *GSAS general structure analysis system operation manual*, volume 86. 2000.

[108] P. Thompson, D. E. Cox, and J. B. Hastings. *J. Appl. Crystallogr.*, 20(2):79, 1987.

[109] P. Vinet, J. Ferrante, J. H. Rose, and J. R. Smith. *J. Geophys. Res. Solid Earth*, 92(B9):9319, 1987.

[110] H. M. Tütüncü, G. P. Srivastava, S. Bagci, and S. Duman. *Phys. Rev. B*, 74:212506, 2006.

[111] Y. Wang, J. Zhang, H. Xu, Z. Lin, L. L. Daemen, Y. Zhao, and L. Wang. *Appl. Phys. Lett.*, 94(7):071904, 2009.

[112] Tang Ling-Yun, Liu Lei, Liu Jing, Xiao Wan-Sheng, Li Yan-Chun, Li Xiao-Dong, and Bi Yan. *Chin. Phys. Lett.*, 27(1):016402, 2010.

[113] H. Holleck, F. Benesovsky, and H. Nowotny. *Monatsh. Chem.*, 93:996, 1962.

[114] Grant Bunker. *Introduction to XAFS: A Practical Guide to X-ray Absorption Fine Structure Spectroscopy.* Cambridge University Press, 2010.

[115] S. Mobilio, F. Boscherini, and C. Meneghini. *Synchrotron Radiation: Basics, Methods and Applications.* Springer-Verlag Berlin Heidelberg, 2015.

[116] H. Fricke. *Phys. Rev.*, 16:202, 1920.

[117] D. E. Sayers, E. A. Stern, and F. W. Lytle. *Phys. Rev. Lett.*, 27:1204, 1971.

[118] Edward A. Stern. *Phys. Rev. B*, 10:3027, 1974.

[119] F. W. Lytle, D. E. Sayers, and E. A. Stern. *Phys. Rev. B*, 11:4825, 1975.

[120] E. A. Stern, D. E. Sayers, and F. W. Lytle. *Phys. Rev. B*, 11:4836, 1975.

[121] D. C. Koningsberger and R. Prins. *X-Ray Absorption: Principles, Applications, Techniques of EXAFS, SEXAFS and XANES.* Wiley, 1988.

[122] A. Filipponi, A. Di Cicco, and C. R. Natoli. *Phys. Rev. B*, 52:15122, 1995.

[123] J. J. Rehr and R. C. Albers. *Rev. Mod. Phys.*, 72:621, 2000.

[124] G. Dalba and P. Fornasini. *J. Synchrotron Radiat.*, 4(4):243, 1997.

[125] O. Mathon, A. Beteva, J. Borrel, D. Bugnazet, S. Gatla, R. Hino, I. Kantor, T. Mairs, M. Munoz, S. Pasternak, F. Perrin, and S. Pascarelli. *J. Synchrotron Radiat.*, 22(6):1548, 2015.

[126] B. Ravel and M. Newville. *J. Synchrotron Radiat.*, 12(4):537, 2005.

[127] Y. Iwasawa, K. Asakura, and M. Tada. *XAFS Techniques for Catalysts, Nanomaterials, and Surfaces.* Springer International Publishing, 2017.

[128] J. Timoshenko, A. Kuzmin, and J. Purans. *J. Phys. Condens. Matter*, 26(5):055401, 2014.

[129] I. Schiesaro. Analisi EXAFS di superconduttori Nb_3Sn. Master's thesis, Roma Tre University, 2018.

[130] W. Kohn. *Rev. Mod. Phys.*, 71:1253, 1999.

[131] P. Hohenberg and W. Kohn. *Phys. Rev.*, 136:B864, 1964.

[132] Richard M. Martin. *Electronic Structure: Basic Theory and Practical Methods.* Cambridge University Press, 2004.

[133] W. Kohn and L. J. Sham. *Phys. Rev.*, 140:A1133, 1965.

[134] P. Ziesche, H. Eschrig, Technische Universität Dresden. Institut für Theoretische Physik, and European Physical Society. *Electronic structure of solids '91.* Physical research. Akademie Verlag, 1991.

[135] Kieron Burke. *J. Chem. Phys*, 136(15):150901, 2012.

[136] Stefano Baroni, Paolo Giannozzi, and Andrea Testa. *Phys. Rev. Lett.*, 58:1861, 1987.

[137] P. Giannozzi, S. Baroni, N. Bonini, M. Calandra, R. Car, C. Cavazzoni, D. Ceresoli, G. L. Chiarotti, M. Cococcioni, I. Dabo, A. Dal Corso, S. de Gironcoli, S. Fabris, G. Fratesi, R. Gebauer, U. Gerstmann, C. Gougoussis, A. Kokalj, M. Lazzeri, L. Martin-Samos, N. Marzari, F. Mauri, R. Mazzarello, S. Paolini, A. Pasquarello, L. Paulatto, C. Sbraccia, S. Scandolo, G. Sclauzero, A. P. Seitsonen, A. Smogunov, P. Umari, and R. M. Wentzcovitch. *J. Phys. Condens. Matter*, 21(39):395502, 2009.

[138] X. Gonze, F. Jollet, F. Abreu Araujo, D. Adams, B. Amadon, T. Applencourt, C. Audouze, J. M. Beuken, J. Bieder, A. Bokhanchuk, E. Bousquet, F. Bruneval, D. Caliste, M. Côté, F. Dahm, F. Da Pieve, M. Delaveau, M. Di Gennaro, B. Dorado, C. Espejo, G. Geneste, L. Genovese, A. Gerossier, M. Giantomassi, Y. Gillet, D.R. Hamann, L. He, G. Jomard, J. Laflamme Janssen, S. Le Roux, A. Levitt, A. Lherbier, F. Liu, I. Lukačević, A. Martin, C. Martins, M.J.T. Oliveira, S. Poncé, Y. Pouillon, T. Rangel, G. M. Rignanese, A.H. Romero, B. Rousseau, O. Rubel, A.A. Shukri, M. Stankovski, M. Torrent, M.J. Van Setten, B. Van Troeye, M.J. Verstraete, D. Waroquiers, J. Wiktor, B. Xu, A. Zhou, and J.W. Zwanziger. *Comput. Phys. Commun.*, 205:106, 2016.

[139] J. Hafner and G. Kresse. The Vienna AB-Initio Simulation Program VASP: An Efficient and Versatile Tool for Studying the Structural, Dynamic, and Electronic Properties of Materials. In Turchi P. E. A., editor, *Properties of Complex Inorganic Solids*, page 69. Springer, Boston, MA, 1997.

[140] X. Andrade, D. Strubbe, U. De Giovannini, A. H. Larsen, M. J. T. Oliveira, J. Alberdi-Rodriguez, A. Varas, I. Theophilou, N. Helbig, M. J. Verstraete, L. Stella, F. Nogueira, A. Aspuru-Guzik, A. Castro, M. A. L. Marques, and A. Rubio. *Phys. Chem. Chem. Phys.*, 17:31371, 2015.

[141] S. J. Clark, M. D. Segall, C. J. Pickard, P. J. Hasnip, M. I. J. Probert, K. Refson, and M. C. Payne. *Cryst. Mater.*, 220(5-6):567, 2009.

[142] Stefano Baroni, Stefano de Gironcoli, Andrea Dal Corso, and Paolo Giannozzi. *Rev. Mod. Phys.*, 73(2):515, 2001.

[143] H. Hellmann. *Einführung in die Quantenchemie.* Franz Deuticke, 1937.

[144] R. P. Feynman. *Phys. Rev.*, 56:340, 1939.

[145] Hendrik J. Monkhorst and James D. Pack. *Phys. Rev. B*, 13:5188, 1976.

[146] N. W. Ashcroft and N. D. Mermin. *Solid State Physics.* Saunders College, Philadelphia, 1976.

[147] N. Marzari, D. Vanderbilt, A. De Vita, and M. C. Payne. *Phys. Rev. Lett.*, 82:3296, 1999.

[148] Salomon R Billeter, Alessandro Curioni, and Wanda Andreoni. *Comput. Mater. Sci.*, 27(4):437, 2003.

[149] V. Guritanu, W. Goldacker, F. Bouquet, Y. Wang, R. Lortz, G. Goll, and A. Junod. *Phys. Rev. B*, 70:184526, 2004.

[150] J. H. Westbrook and R. L. Fleischer. *Crystal Structures of Intermetallic Compounds*, volume 1 of *Intermetallic Compounds.* Wiley, 2000.

[151] Agnès Dewaele, Marc Torrent, Paul Loubeyre, and Mohamed Mezouar. *Phys. Rev. B*, 78:104102, 2008.

[152] J. Long, L. Yang, and X. Wei. *J. Alloys Compd.*, 549:336, 2013.

[153] R. Loria, G. De Marzi, S. Anzellini, L. Muzzi, N. Pompeo, F. Gala, E. Silva, and C. Meneghini. *IEEE Trans. Appl. Supercond.*, 27(4):8400305, 2017.

[154] Seiichi Kagoshima. *Jpn. J. Appl. Phys.*, 20(9):1617, 1981.

[155] R. Peierls. *More Surprises in Theoretical Physics.* Priceton University Press, 1991.

[156] J. M. Ziman. *Principles of the Theory of Solids.* Cambridge University Press, 1964.

[157] J. C. Jamieson, A. W. Lawson, and N. D. Nachtrieb. *J. Res. Natl. Bur. Stand. Sec. A*, 63A(1):55, 1959.

[158] C. E. Weir, E. R. Lippincott, A. Van Valkenburg, and E. N. Bunting. *Rev. Sci. Instrum.*, 30(11):1016, 1959.

[159] A. Van Valkenburg. *Conférence Internationale Sur-les Hautes Pressions.* Le Creusot, Saone-et-Loire, France, 1965.

[160] J. M. Besson and J. P. Pinceaux. *Science*, 206(4422):1073, 1979.

[161] H. K. Mao, R. J. Hemley, Y. Wu, A. P. Jephcoat, L. W. Finger, C. S. Zha, and W. A. Bassett. *Phys. Rev. Lett.*, 60:2649, 1988.

[162] Takemura K. *J. Appl. Phys.*, 89(1):662, 2001.

[163] R. Letoullec, J. P. Pinceaux, and P. Loubeyre. *High. Press. Res.*, 1(1):77, 1988.

[164] R. A. Forman, G. J. Piermarini, J. D. Barnett, and S. Block. *Science*, 176:284, 1972.